FACULTY
OF MATHEMATICS
AND PHYSICS
Charles University

DOCTORAL THESIS

Michael Pešek

Pion-induced polarized Drell-Yan process at COMPASS

Department of Low Temperature Physics

Supervisor of the doctoral thesis:	M.Sc. Michael Finger, CSc.
Study programme:	Physics
Study branch:	Subnuclear Physics

Prague 2020

I declare that I carried out this doctoral thesis independently, and only with the cited sources, literature and other professional sources.

I understand that my work relates to the rights and obligations under the Act No. 121/2000 Sb., the Copyright Act, as amended, in particular the fact that the Charles University has the right to conclude a license agreement on the use of this work as a school work pursuant to Section 60 subsection 1 of the Copyright Act.

In .... date .... signature of the author

I would like to thank both to Miroslav and Michael Finger for giving me the opportunity to work on the COMPASS experiment and for the support through all these years.

A big thank you belongs to the full COMPASS collaboration. Special thanks, not in the order of the importance, goes to: Vincent Andrieux with whom I had the pleasure to coordinate the 2018 data-taking, to Annika Vauth and Vladimir Anosov for the pleasure to join the work on the hardware side of the experiment, to the polarised target group (Nori, Genki, Jaakko, Kaori, and Yuri) for all the fun around the work on the polarised target, to ”The Czech Mafia”, without them I would never be able to survive all those years at CERN, to Bakur Parsamyan who despite being overly busy had always an advice at hand, not only for the analysis, and finally to my wife for all the support without which I would have gone crazy a long time ago.

Title: Pion-induced polarized Drell-Yan process at COMPASS

Author: Michael Pešek

Department: Department of Low Temperature Physics

Supervisor: M.Sc. Michael Finger, CSc., Department of Low Temperature Physics

Abstract:

In this work we present the basic theoretical concepts of the description of the nucleon spin structure. The theoretical background of two processes of interest - Semi-inclusive DIS and Drell-Yan - in the terms of Transverse Momentum Dependent Parton distribution Functions is presented. The COMPASS experiment and particularly its unique polarised target are described in detail. Several target related measurements are presented. The express analysis and detector efficiencies analysis are presented as examples of important hardware related analysis. Finally two measurements of Transverse Spin Asymmetries are presented. The first measurement is the measurement of the Transverse Spin Asymmetries in J/ψ production in the Semi-inclusive DIS on polarised protons. The second measurement is the measurement of Transverse Spin Asymmetries in J/ψ in the $\pi^{-}p$ polarised Drell-Yan data.

Keywords: parton distribution functions, Drell-Yan process, J/ψ meson, COMPASS experiment, polarised target

Contents

Introduction **4**

1 Theory overview **5**
1.1 Deep Inelastic Scattering . . . 5
1.2 Parton model and Parton distribution functions . . . 6
1.2.1 Transversity . . . 7
1.3 Transverse momentum dependent PDFs . . . 8
1.3.1 QCD, TMDs and Sign change . . . 10
1.4 Semi-Inclusive DIS . . . 10
1.4.1 Description within the TMD framework . . . 11
1.5 J/ψ production and gluon Sivers function in SIDIS . . . 13
1.6 Drell-Yan process at the leading twist . . . 14
1.7 J/ψ production in pion-proton interactions . . . 17
1.8 Current knowledge . . . 17

2 COMPASS experimental setup **21**
2.1 Beamline . . . 21
2.2 Beam particle identification . . . 22
2.3 Beam telescope . . . 23
2.4 Target region . . . 23
2.5 Spectrometer . . . 26
2.5.1 Micromegas detectors . . . 26
2.5.2 Drift chambers . . . 26
2.5.3 Straw trackers . . . 27
2.5.4 Ring imaging Cherenkov detector . . . 27
2.5.5 Multi-wire proportional chambers . . . 28
2.5.6 GEM detectors . . . 28
2.5.7 Scintillating fibres . . . 28
2.5.8 Muon identification . . . 28
2.5.9 Calorimeters . . . 29
2.5.10 Magnets . . . 29
2.6 Trigger system and Data Acquisition . . . 29
2.6.1 Trigger system . . . 29
2.6.2 Data Acquisition . . . 30
2.7 Data processing and reconstruction . . . 31
2.8 Data taking, performance and resolutions . . . 32
2.8.1 Data taking . . . 32
2.8.2 Performance and resolutions . . . 32

3 COMPASS polarised target **33**
3.1 The need for the polarised target . . . 33
3.2 Dynamic nuclear polarisation . . . 33
3.2.1 Solid state effect . . . 34
3.2.2 Spin temperature . . . 34
3.3 Polarisation measurement and TE calibration . . . 36

3.3.1 TE calibration 36
3.4 Dilution refrigerator 37
3.4.1 Target holder 39
3.5 Magnet system 40
3.6 Microwave system 42
3.7 NMR system 43
3.8 Target material and radiation hardness 43
3.9 Target material weight measurement 45
3.10 Relaxation time measurements in 2018 46
3.10.1 Relaxation time in zero magnetic field 46
3.10.2 Polarisation loss during the magnetic field rotation 47

4 Express Analysis during 2015 DY run **49**
4.1 Introduction 49
4.1.1 Data processing 49
4.2 Examples 49
4.2.1 Good run 50
4.2.2 Pixel MicroMegas issue 51
4.2.3 Dead time setting test 51
4.3 Conclusions and lessons learned 51

5 Detector efficiency studies in 2015 data **55**
5.1 General principles 55
5.2 Beam telescope 55
5.3 Vertex detector 56
5.4 GEM detectors 58
5.5 Conclusion 59

6 General analysis principles **60**
6.1 Data stability 60
6.1.1 Bad spill analysis 60
6.1.2 Bad run analysis 61
6.2 Event selection 62
6.3 Raw asymmetry extraction 63
6.4 Determination of the physics asymmetries 64
6.5 False asymmetries, pulls and systematics 64
6.5.1 Pulls 64
6.5.2 Time false asymmetries 64
6.5.3 Target false asymmetries 64

7 Transverse spin asymmetries in J/ψ production in 2010 SIDIS data **65**
7.1 Data selection 65
7.2 Kinematic distribution 67
7.3 Results 68
7.4 Systematics and Conclusion 69

8 Transverse spin asymmetries in J/ψ production in 2015 Drell-Yan data **74**
8.1 Data selection 74
8.2 Kinematic distribution 75
8.3 Results 75
8.4 Systematics 76
8.4.1 False asymmetries 77
8.4.2 Polarisation and dilution factor 77
8.4.3 Feed-down contribution and unpolarised asymmetry 78
8.5 Conclusion 78

Conclusion **84**

Bibliography **85**

List of Figures **90**

List of Tables **92**

List of Abbreviations **93**

List of publications **94**

Introduction

The large A_N asymmetry in hadron-hadron collisions [1; 2], the spin crisis [3], possible violation of Lam-Tung relation in Drell-Yan production [4; 5; 6] - these are only few of the puzzling experimental evidence which stimulated immense development of theoretical description of the hadron structure. One of the examples could be the role of axial anomaly in possible large gluon polarisation explaining the spin puzzle [7]. Other examples are the new developments beyond the collinear approximation. Namely the Generalised Parton Distributions (GPDs) [8] which provide unique possibility to measure quark orbital angular momentum via the Ji sum rule [9] and the Transverse Momentum Dependent Parton Distributions (TMD PDFs) with its contra-intuitive T-odd Sivers [10] and Boer-Mulders [11] distributions. These naturally stimulated more experimental research and lead, among others, to the rich physics programme of the COMPASS experiment at CERN [12].

In this work we focus on one of the key features of COMPASS experiment - the polarised target and the related TMD physics with a new results from the two parts of the COMPASS experimental programme - the transversely polarised Semi-inclusive DIS and Drell-Yan processes, which might, hopefully, bring more light in to the intriguing physics of the proton (spin) structure.

The first chapter of this thesis describes in compact form the relevant processes and the emergence of the TMD PDFs.

The second chapter describes the COMPASS spectrometer and the difference between the SIDIS measurements setup and the Drell-Yan measurement setup.

The third chapter describes in more details the COMPASS polarised target and its performance together with an interesting measurement concerning the relaxation behaviour of the ammonia material.

The fourth and fifth chapter present two kind of technical analyses using the 2015 data. First part is dedicated to the express analysis which was done quasi-online and directly impacted the ongoing data taking. The second part is related to detector performance.

The sixth chapter describes the common parts of analysis of the 2010 and 2015 data.

Finally the seventh and eighth chapters describe the analysis of transverse spin dependent asymmetries in the SIDIS and Drell-Yan measurement.

1. Theory overview

In this chapter we present the main ideas concerning the description of the nucleon structure and the relevant scattering processes - (semi-inclusive) deep inelastic scattering and Drell-Yan process. This text does not aspire to cover all theoretical intricacies of the subject. For that we will give reference to a more extended theoretical coverage whenever possible. In addition, we refer to the "bible of the modern QCD" [13].

1.1 Deep Inelastic Scattering

We start with deep inelastic scattering (DIS) process of high energy leptons[1] off nucleons described by the following formula:

$$L(l) + N(P) \longrightarrow L(l') + X, \tag{1.1}$$

where the l and l' denote the four-momenta of the scattered lepton, P denotes the four-momentum of the nucleon, and X denotes remnants of the nucleon produced during the collision. The process can be described by the following kinematic variables [14]:

$$Q^2 = -q^2 = -(l-l')^2 = 2EE'(1-\cos\theta), \tag{1.2}$$

$$x = \frac{Q^2}{2P\cdot q}, \tag{1.3}$$

$$y = \frac{P\cdot q}{P\cdot l} = \frac{E_{lab} - E'_{lab}}{E_{lab}}, \tag{1.4}$$

$$W^2 = (P+q)^2, \tag{1.5}$$

where E and E' denote the initial and final lepton energy, θ is the scattering angle, and q is the momentum transfer between the lepton and the hadronic system. The Feynman diagram of the process is shown in Fig. 1.1.

The x, also called Bjorken variable, varies between 0 and 1, which is true also for the inelasticity variable y. The precise meaning of the Bjorken x related to the parton distribution functions will be discussed later. The W represent the invariant mass of the hadronic system X. Note that only two out of the four variables are independent. The combination of (x,Q^2) is usually used. In case of the elastic scattering the $x = 1$ and $W = M$ and only one variable remains independent.

We can now proceed to the cross-section calculation. The cross-section is given [14] by the contraction of the leptonic tensor $L_{\mu\nu}$ and hadronic tensor $W_{\mu\nu}$:

$$d\sigma \propto L_{\mu\nu}W^{\mu\nu}. \tag{1.6}$$

The leptonic tensor $L_{\mu\nu}$ is easily calculable in the QED [14]. It should be noted that for the transversely polarised lepton the corresponding part of the lepton

[1] We consider only charged leptons here

tensor is suppressed by a factor of m/E [16]. Therefore only the unpolarised or longitudinally polarised case is considered.

The hadronic tensor $W_{\mu\nu}$ is non-perturbative object and can be parametrised. Taking into account the parity conservation, calibration invariance and Lorenz invariance, the tensor can be parametrised by 4 independent structure functions F_1, F_2 (unpolarised case), G_1 and G_2 (longitudinally polarised case) [2]. The spin-independent cross-section is then expressed [14]:

$$\frac{d\sigma}{dxdQ^2} = \frac{4\pi\alpha^2}{Q^4}\left[y^2 F_1(x,Q^2) + (1 - y - \frac{xyM^2}{s})\frac{F_2(x,Q^2)}{x}\right]. \tag{1.7}$$

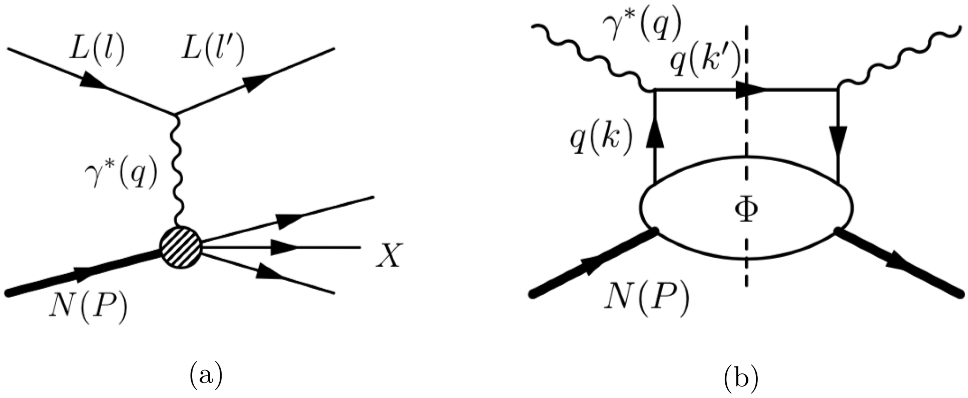

Figure 1.1: The DIS Feynman diagram (a) and the corresponding handbag diagram (b), taken from Ref. [15]

The independence of the F_1 and F_2 functions on Q^2[3] measured by at SLAC [17] lead to the formulation the parton model [18].

1.2 Parton model and Parton distribution functions

In the parton model the scattering is described as scattering off the free point-like nucleon constituents [18]. The cross-section is then given as an incoherent sum of the individual cross-sections. At the leading order only quarks contribute and the hadronic tensor can be written as [16]:

$$\begin{aligned} W^{\mu\nu} = \frac{1}{2\pi}\sum_q e_q^2 \sum_X \int \frac{d^3 P_X}{(2\pi)^3 2E_X} \int d^4k \int d^4k' \delta(k'^2)\delta^{(4)}(P - k - P_X) \\ \times\delta^{(4)}(k + q - k')[\bar{u}(k')\gamma^\mu \phi(k;P,S)]^*[\bar{u}(k')\gamma^\nu \phi(k;P,S)], \end{aligned} \tag{1.8}$$

where e_q are the parton charges, $\bar{u}$ is the quark bi-spinor and ϕ are the matrix elements of the quark fields between the nucleon and its remnants. We can now

[2]Usually the G_1 and G_2 structure functions are labeled as g_1 and g_2. This could lead to confusion with helicity function discussed latter, so we adopt this convention of labeling.

[3]There is actually mild dependence on Q^2, which is explained in the QCD framework [14].

define the quark-quark correlation matrix, shown in Fig. 1.1:

$$\Phi_{ij} = \sum_X \int \frac{d^3P_X}{(2\pi)^3 2E_X}(2\pi)^4 \delta^{(4)}(P-k-P_X) \langle PS| \psi_j(0) |X\rangle \langle X| \psi_i(0) |PS\rangle , \quad (1.9)$$

where the $\langle X| \psi_i(0) |PS\rangle = \phi_i$. After substituting the correlation matrix to the hadronic tensor $W_{\mu\nu}$ we obtain [16]:

$$W^{\mu\nu} = \sum_q e_q^2 \int \frac{d^4k}{(2\pi)^4} \delta[(k+q)^2] \, \mathrm{Tr}[\Phi \gamma^\mu (\not{k} + \not{q}) \gamma^\nu]. \quad (1.10)$$

In the infinite-momentum frame (also called brick-wall reference frame) usually used in the DIS description [14] the on-shell condition $\delta[(k+q)^2]$ from Eq. 1.10 leads to the struck quark momentum [16] $k^\mu \approx xP^\mu + k_T^\mu$, where k_T^μ quark initial transverse momentum. The Bjorken x can be then interpreted as the fraction of the nucleon momentum carried by the struck quark.

The hadron tensor can be now decomposed into the vector and axial-vector parts. Using the following parametrisations [16]:

$$f_1(x)P^\mu = \frac{1}{2}\int \frac{d^4k}{(2\pi)^4} \delta(x - \frac{k^+}{P^+}) \, \mathrm{Tr}(\gamma^\mu \Phi), \quad (1.11)$$

$$g_1(x)P^\mu = \frac{1}{2}\int \frac{d^4k}{(2\pi)^4} \delta(x - \frac{k^+}{P^+}) \, \mathrm{Tr}(\gamma^\mu \gamma_5 \Phi), \quad (1.12)$$

then leads to the structure functions [16]:

$$\begin{aligned} F_2(x) = 2xF_1(x) &= \sum_{e_q} x[f_1^q(x) + f_1^{\bar{q}}(x)], \\ G_1(x) &= \frac{1}{2}\sum_{e_q} x[g_1^q(x) + g_1^{\bar{q}}(x)], \end{aligned} \quad (1.13)$$

where the $f_1^q(x)$ is the number density or ordinary (unpolarised) parton distribution function (PDF) and the $g_1^q(x)$ is the helicity PDF of longitudinally polarised quarks in the longitudinally polarised nucleon.

Note that the above construction is valid at the leading twist $\mathcal{O}(P^+)$[4]. The vector part of the hadronic tensor couples with four-momentum P^μ of the leptonic tensor $L_{\mu\nu}$, while the axial-vector part couples with the longitudinal component of the spin four-vector part of the $L_{\mu\nu}$ tensor.

1.2.1 Transversity

We have seen in the previous section that description of the scattering process by the correlation matrix leads to the natural definition of parton distribution functions. We will show now that there is an additional distribution function at the leading twist, the transversity function, which is analogous to the helicity function but for a transversely polarised nucleon. We will also see why it cannot be measured in the inclusive DIS.

[4]The $\pm$ components label the light-cone coordinates defined for any vector v as $v^\pm = (v^0 \pm v^3)$.

Ignoring the transverse momentum of the partons and having the spin four-vector $S^\mu \approx (\frac{\lambda_N}{M})P^\mu + S_T^\mu$ we can write down the most general form of the correlation matrix [16]:

$$\Phi(k,P,S) = \frac{1}{2}\left[A_1 \not{P} + A_2 \lambda_N \gamma_5 \not{P} + A_3 \not{P} \gamma_5 \not{S}_T\right], \tag{1.14}$$

where $A_n(k^2, k \cdot P)$ are real functions. After integration over k and using the definition of the correlation matrix we get [16]:

$$f_1(x) = \frac{1}{2}\int \frac{d^4k}{(2\pi)^4}\,\mathrm{Tr}(\gamma^+\Phi)\delta(k^+ - xP^+), \tag{1.15}$$

$$g_1(x) = \frac{1}{2}\int \frac{d^4k}{(2\pi)^4}\,\mathrm{Tr}(\gamma^+\gamma_5\Phi)\delta(k^+ - xP^+), \tag{1.16}$$

$$h_1(x) = \frac{1}{2}\int \frac{d^4k}{(2\pi)^4}\,\mathrm{Tr}(\gamma^+\gamma^1\gamma_5\Phi)\delta(k^+ - xP^+), \tag{1.17}$$

where the $h_1(x)$ is the transversity function.

It is well known that these functions have rather simple probabilistic interpretation [14]. The $f_1(x)$ is the probability to find the given quark with momentum xP inside a nucleon with momentum P. The helicity $g_1(x)$ is difference of probabilities to find the given quark with helicity $+$ and $-$ in nucleon with helicity $+$. The transversity $h_1(x)$ is analogous to the helicity but concerns transversely polarised quark in transversely polarised nucleon. Note that the the helicity interpretation works only in the longitudinal polarisation basis and analogously the transversity interpretation works in the transverse polarisation basis.

We can now use the optical theorem [19] to explain why the transversity does not appear in the inclusive DIS. According to the optical theorem the hadronic tensor is related to the forward virtual Compton scattering amplitude. The leading twist distributions can be then written using the quark-nucleon forward amplitudes $A_{\Lambda\lambda,\Lambda'\lambda'}$ shown in Fig. 1.2 (a). The subscripts denote the helicities of the nucleon and quark. There are only three independent amplitudes due to parity invariance and helicity conservation. They are: $A_{++,++}$, $A_{+-,+-}$ and $A_{+-,-+}$. Finally the quarks distributions can be written down:

$$\begin{aligned} f_1(x) &\propto \Im(A_{++,++} + A_{+-,+-}), \\ g_1(x) &\propto \Im(A_{++,++} - A_{+-,+-}), \\ h_1(x) &\propto \Im A_{+-,-+}. \end{aligned} \tag{1.18}$$

We can now see why the transversity cannot be measured in the inclusive DIS. The transversity is given by the Compton amplitude which requires chirality flip. That is not allowed in the QED as shown in Fig. 1.2 (b). However, the transversity can be studied in other processes as will be shown in further sections.

1.3 Transverse momentum dependent PDFs

We now consider the case when we take into account the full quark momentum $k^\mu \approx xP^\mu + k_T^\mu$ without neglecting the transverse part k_T. This is relevant e.g. in

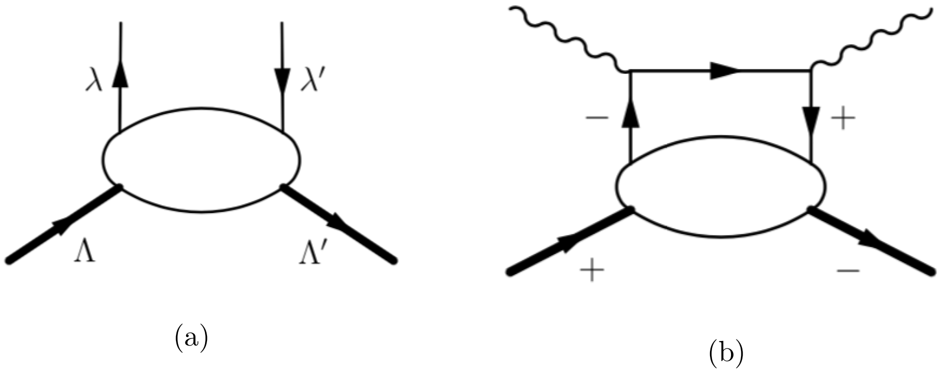

Figure 1.2: (a) The quark-nucleon forward amplitude, (b) the chirality forbidden amplitude, taken from Ref. [15].

Parton \ Nucleon	Unpolarised	Longitudinal	Transverse
U	f_1 (number density)		$f_{1T}^{\perp}$ (Sivers)
L		g_1 (helicity)	g_{1T} (worm-gear)
T	$h_1^{\perp}$ (Boer-Mulders)	$h_{1L}^{\perp}$ (worm-gear)	h_1 (transversity) $h_{1T}^{\perp}$ (pretzelosity)

Table 1.1: Leading twist TMD PDFs

the case of the semi-inclusive DIS (SIDIS) or the Drell-Yan processes, where the final state particle carry the information on the initial transverse momentum of the quark, and where the final state transverse momentum is measured.

The full correlation matrix at leading twist then reads [16]:

$$
\begin{aligned}
\Phi(k,P,S) = \frac{1}{2}[&\not{P}A_1 + \epsilon_{\mu\nu\rho\sigma}\gamma^{\mu}\frac{P^{\nu}k_T^{\rho}S_T^{\sigma}}{M}\tilde{A}_1 + \lambda_N\gamma_5\not{P}A_2 \\
&+ \frac{\boldsymbol{k}_T\cdot\boldsymbol{S}_T}{M}\gamma_5\not{P}\tilde{A}_2 + \not{P}\gamma_5\not{S}_T A_3 + \frac{\boldsymbol{k}_T\cdot\boldsymbol{S}_T}{M^2}\not{P}\gamma_5\not{k}_T\tilde{A}_3 \\
&+ \frac{\lambda_N}{M}\not{P}\gamma_5\not{k}_T\tilde{A}_4 + \epsilon_{\mu\nu\rho\sigma}\gamma^{\mu}\gamma^{\nu}\gamma_5\frac{P^{\rho}k_T^{\sigma}}{M}\tilde{A}_5].
\end{aligned}
\tag{1.19}
$$

We now have 8 real functions A_N compared to the previous case of 3 functions in Eq. 1.14. It should be noted that after projecting the vector, axial-vector and tensor component of Eq. 1.19 and integrating over the k_T the result yields the distribution functions as written in Eqs. 1.15, 1.16 and 1.17.

Integration of the matrix in Eq. 1.19 over the momentum longitudinal components k^+ and k^- leads to a new set of parton distribution dependent on k_T, which are called Transverse Momentum Dependent Parton Distribution Functions (TMD PDFs or just TMDs). Three of them are generalisation of the ordinary PDFs, the other are completely new objects. The TMDs are summarised in Tab. 1.1.

All of the leading-twist TMDs have probabilistic interpretation. They are believed to be universal, meaning the various processes can be factorised [13] in the perturbative hard part and non-perturbative TMDs, which are independent on the used process. In addition there exist more TMDs beyond the leading twist which arise from either more complex correlations (quark-quark-gluon) or kinematic effects. They have no probabilistic interpretation [13; 16].

1.3.1 QCD, TMDs and Sign change

It is known [14] that ordinary PDFs have logarithmic dependence on the scale at which they are measured. This dependence is described by the DGLAP equations [20]. This evolution arises from the QCD description of the quarks and gluons, where the quarks can emit gluons and the gluons can split into $q\bar{q}$ pairs. Unlike the collinear evolution, the TMD evolution is still highly debated subject [22]. We will briefly mention this debate in the section on current knowledge.

Additionally, the above definitions of the TMDs are not gauge-invariant in QCD [13]. This implies the need for so-called Wilson lines (also called gauge links)[5] to be added into the definitions. This has important consequences concerning the Sivers $f_{1T}^{\perp}$ and Boer-Mulders $h_1^{\perp}$ function. It leads to the following prediction:

$$\begin{aligned} \left[h_1^{\perp}(x)\right]_{SIDIS} &= -\left[h_1^{\perp}(x)\right]_{DY}, \\ \left[f_{1T}^{\perp}(x)\right]_{SIDIS} &= -\left[f_{1T}^{\perp}(x)\right]_{DY}. \end{aligned} \tag{1.20}$$

The Sivers $f_{1T}^{\perp}$ and Boer-Mulders $h_1^{\perp}$ function should be process dependent. Specifically, they should change sign when measured in SIDIS and in Drell-Yan.

Let us mention as a side remark that the history of the Sivers function is rather interesting. It was first predicted in the beginning of 1990s [10] to explain the sizeable asymmetries measured in the proton-proton collisions. It was then assumed to be zero[6]. Finally the prediction was revised for the Sivers to undergo the sign-change [13].

1.4 Semi-Inclusive DIS

We now proceed with the description of the semi-inclusive DIS process. It is a DIS process where at least one of the final state hadron is also detected:

$$L(l,\lambda) + N(P,S) \longrightarrow L(l') + h(P_h) + X. \tag{1.21}$$

The λ denotes the lepton helicity and S is the spin four-vector of the nucleon. In addition to the inclusive DIS variables defined in Eq. 1.2-Eq. 1.5 two additional variables are used. It is the final state hadron transverse momentum $\boldsymbol{P}_h T$ and the relative energy of the hadron [23]:

$$z = \frac{P \cdot P_h}{P \cdot q}. \tag{1.22}$$

[5] They are basically path ordered exponentials of the gluon field along a line, see e.g. [13] or [21].

[6] This was based on the fact that the correlation $(\boldsymbol{k_T} \times \boldsymbol{S_T}) \cdot \boldsymbol{P}$ is time reversal-odd, in reality this not full time reversal as that would require also to change the initial and final states [13].

Note that analogously to the x variable the z is the fraction of the fragmenting quark momentum transferred to the hadron [16]. The corresponding Feynman diagram is shown in Fig. 1.3. The usual reference frame used for the SIDIS description is shown in Fig. 1.4. The z-axis is chosen along the virtual photon momentum q, the lepton scattering plane is then xz-plane.

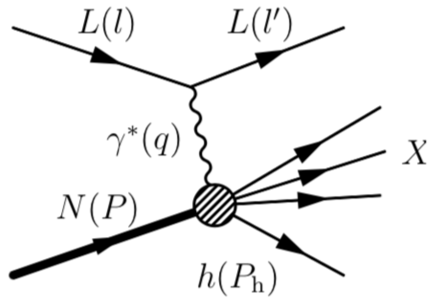

Figure 1.3: The Feynman diagram of the SIDIS process.

In the case of transversely polarised nucleon the SIDIS cross section can be written in model independent way [23]:

$$
\begin{aligned}
\frac{d^6\sigma_{SIDIS}}{dxdydzd\phi_S d\phi_h d\boldsymbol{P}_{hT}^2} = \frac{\alpha^2}{xyQ^2}\left(1+\frac{\gamma^2}{2x}\right) \times \Bigg\{ & \frac{2-2y+y^2}{2}F_{UU,T} + (1-y)F_{UU,L} \\
& +(2-y)\sqrt{1-y}\cos\phi_h F_{UU}^{\cos\phi_h} + (1-y)\cos(2\phi_h)F_{UU}^{\cos\phi_h} \\
& +\lambda y\sqrt{1-y}\sin(\phi_h)F_{LU}^{\sin(\phi_h)} \\
+|\boldsymbol{S}_T|\Bigg[\sin(\phi_h-\phi_S)\Bigg(& \frac{2-2y+y^2}{2}F_{UT,T}^{\sin(\phi_h-\phi_S)} + (1-y)F_{UT,L}^{\sin(\phi_h-\phi_S)}\Bigg) \\
+(1-y)\Bigg(& \sin(\phi_h+\phi_S)F_{UT}^{\sin(\phi_h+\phi_S)} + \sin(3\phi_h-\phi_S)F_{UT}^{\sin(3\phi_h-\phi_S)}\Bigg) \\
+(2-y)\sqrt{1-y}\Bigg(& \sin\phi_S F_{UT}^{\sin\phi_S} + \sin(2\phi_h-\phi_S)F_{UT}^{\sin(2\phi_h-\phi_S)}\Bigg)\Bigg] \\
+\lambda|\boldsymbol{S}_T|\Bigg[& \frac{2y-y^2}{2}\cos(\phi_h-\phi_S)F_{LT}^{\cos(\phi_h-\phi_S)} + y\sqrt{1-y}\cos(\phi_S)F_{LT}^{\cos(\phi_S)} \\
& +y\sqrt{1-y}\cos(2\phi_h-\phi_S)F_{LT}^{\cos(2\phi_h-\phi_S)}\Bigg]\Bigg\},
\end{aligned}
\tag{1.23}
$$

where α is the fine structure constant. The dependence of the structure functions F on variables x, Q^2, z and P_{hT}^2 is assumed. The subscripts in $F_{ab,c}$ denote the polarisations of a) beam, b) nucleon and c) the virtual photon.

1.4.1 Description within the TMD framework

We can now proceed to writing down the hadronic tensor for the SIDIS process. In addition to the inclusive DIS we need also to consider the fragmentation

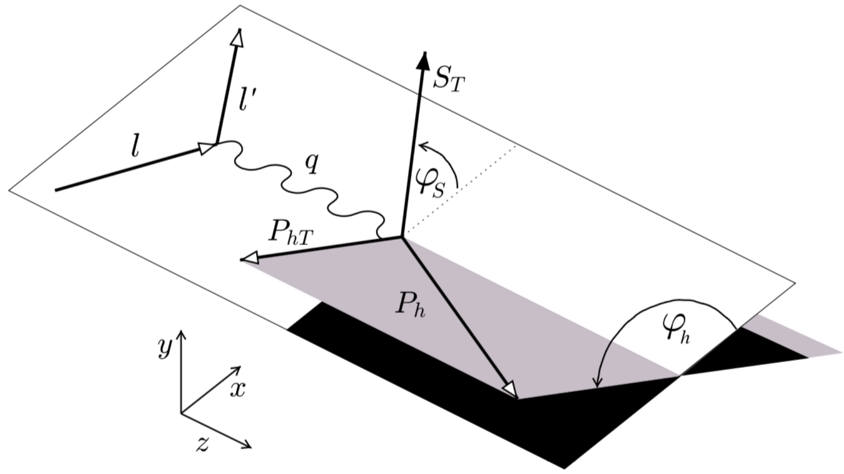

Figure 1.4: The reference frame used for SIDIS description [23].

since we observe the final state hadron. The hadronic tensor reads [16]:

$$W^{\mu\nu} = \sum_q e_q^2 \int \frac{d^4k}{(2\pi)^4} \int \frac{d^4k'}{(2\pi)^4} \delta[(k+q-k')^2]\, \mathrm{Tr}[\Phi\gamma^\mu\Delta\gamma^\nu], \tag{1.24}$$

where k' is the fragmenting quark momentum and Δ is so-called decay matrix which describes the fragmentation of the quark into a hadron, analogously to the correlation matrix Φ [16].

The decay matrix Δ can be parametrised in a similar way as the correlation matrix Φ. There are three parameters left after integrating the matrix over k'. They are the Fragmentation Functions (FFs) $D_1(z)$, $G_1(z)$ and $H_1(z)$ [16]. The $D_1(z)$ gives the probability to having the quark with the longitudinal momentum fraction z fragmenting into the hadron. It is analogous to the f_1 distribution function. The $G_1(z)$ and $H_1(z)$ are then analogous to the spin-dependent distributions g_1 and h_1.

Integrating the decay matrix over the longitudinal momentum components yield eight transverse momentum dependent FFs [16]. As with the TMD PDFs they are generalisations of the $D_1(z)$, $G_1(z)$ and $H_1(z)$ functions. Many of these depend on the spin of the hadron, which is usually not measured in experiments[7]. In addition the majority of the hadrons produced in the experiments are scalar meson with zero spin. Further discussion will be restricted to that particular case.

Note that there exists an interesting fragmentation function $H_1^\perp(x, p_T^2)$ called the Collins fragmentation function [16]. It correlates the transverse momentum of the final state hadron with the spin of the fragmenting quark. It can be used to measure the quark polarisation inside the nucleon via the angular distribution in the cross-section.

Using the above mentioned parametrisations of the correlation and decay matrices the SIDIS cross-section amplitudes F can be written down in terms of convolution of the TMDs and TMD FFs [23]. The expressions are available up to twist-3 level [23]. We will limit ourselves only to the nucleon transverse spin

[7]With the exception of the self-analysing decays like e.g. the lambda baryon.

amplitudes at twist-2 as these are goal of the measurement presented latter in this work. The relevant amplitudes[8] are then [23]:

$$
\begin{aligned}
&F_{UT,T}^{\sin(\phi_h-\phi_S)} \propto f_1 \otimes D_1,\\
&F_{UT,L} = 0,\\
&F_{UT}^{\sin(\phi_h+\phi_S)} \propto h_1 \otimes H_1^{\perp},\\
&F_{UT}^{\sin(3\phi_h-\phi_S)} \propto h_{1T}^{\perp} \otimes H_1^{\perp},\\
&F_{UT}^{\sin\phi_S} = 0,\\
&F_{UT}^{\sin(2\phi_h-\phi_S)} = 0,\\
&F_{LT}^{\cos(\phi_h-\phi_S)} \propto g_{1T} \otimes D_1,\\
&F_{LT}^{\cos(phi_S)} = 0,\\
&F_{LT}^{\cos(2\phi_h-\phi_S)} = 0.
\end{aligned}
\tag{1.25}
$$

Note that in principle it might be interesting to measure the amplitudes where only twist-3 contributes even if the interpretation might not be straightforward.

Finally it is convenient from experimental point of view to rewrite the cross-section in terms of asymmetries:

$$A^{\sin\Phi_i} = \frac{\sigma_{\sin\Phi_i}}{\sigma_0}, \tag{1.26}$$

where Φ_i denote any of the possible angular dependencies in the cross-section[9], $\sigma_{\sin\Phi_i}$ is the relevant part of the cross-section and σ_0 is the unpolarised cross-section. Possible kinematic variables can be fully or partly integrated over. The advantage of this redefinition is that many experimental uncertainties cancel out.

1.5 J/ψ production and gluon Sivers function in SIDIS

We have so far ignored the gluon distributions. It is known that the ordinary gluon PDF can me determined from the Q^2 evolution of the ordinary quark PDFs [20]. Another option is a measurement of prompt photon production, which is being considered for possible future measurement of gluon distributions in kaons at AMBER/COMPASS++ [24]. In addition to these there are at least two other experimental options which could provide access to the TMDs.

First possibility is the photon-gluon fusion subprocess process $\gamma^* g \to q\bar{q}$ in leptoproduction. Unfortunately there are several other processes with the same final state, which can create a significant background. It is experimentally rather difficult measurement, but it has been performed before at COMPASS [25].

Second option is a heavy quark production (charm or bottom), where photon-gluon fusion dominates as the corresponding PDFs in a nucleon are suppressed. This method has been also used [26]. However, its disadvantage is the low statistics available.

[8] Note that $F_{UT,L} = 0$ also at twist-3.

[9] Note that all the angular distributions are orthogonal.

The papers [27] and [28] propose to study the following process:

$$l + N^{\uparrow} \longrightarrow l' + \mathrm{J}/\psi + X \tag{1.27}$$

and to measure the amplitude of the Sivers modulation $\sin(\phi_h - \phi_S)$. The paper [27] uses the color evaporation model to predict rather significant effect up to several tens of percent.

The paper [28] uses the TMD framework to predict a significant effect up to 20 %. The main difference with respect to the usual leptoproduction of charged hadrons is that the J/ψ is assumed to be produced exclusively ($z = 1$). The predictions needs to be treated with care since the gluon Sivers function is virtually unknown. We present the relevant measurements performed with COMPASS data in the chapter 7.

1.6 Drell-Yan process at the leading twist

In this section we present the description of dilepton production in hadron-hadron collisions known as the Drell-Yan process [29]. In our case the reaction reads:

$$H_a(P_a) + H_b(P_b, S) \longrightarrow L^+(l^+) + L^-(l^-) + X, \tag{1.28}$$

where we assume spin-0 beam hadron H_a and transversely polarised hadron H_b[10]. The P_a and P_b denote the hadron momenta and l^+ and l^- denote the lepton momenta. It is convenient to define $q = l^+ + l^-$. The corresponding Feynman diagram is shown in Fig. 1.5.

Following variables are commonly used for the description of the Drell-Yan process:

$$\begin{aligned} Q^2 &= q^2 = M^2, \\ x_a &= \frac{Q^2}{2P_a \cdot q}, \\ x_b &= \frac{Q^2}{2P_b \cdot q}, \\ x_F &= x_a - x_b, \end{aligned} \tag{1.29}$$

where M^2 is the dilepton invariant mass and the x_a and x_b are the Bjorken variables of the beam and target hadron, respectively.

The single-polarised Drell-Yan process is commonly described in the target rest frame and the Collins-Sopper frame [30]. The reference frames are shown in Fig. 1.6. The target rest frame is the rest frame of target nucleon, where the z-axis is defined along the beam particle momentum. The x-axis is defined along the q_T, which is the transverse component of the virtual photon momentum q with respect to the z-axis. The Collins-Sopper frame is then obtained from the target frame by two subsequent Lorentz boosts. First boost is done along the target frame z-axis so that the longitudinal component of q vanishes. Second boost is then along the target frame x-axis, which makes the q_T to vanish.

[10]Note that the COMPASS experiment uses pion beam impinging on the polarised proton target.

In total three angles are used for the process description. The ϕ_S is defined in the target rest frame as angle between the q_T and the transverse spin S_T of the nucleon. The ϕ and θ angles are the azimuthal and polar angles of the negative muon momentum in the Collins-Sopper frame as illustrated in Fig. 1.6.

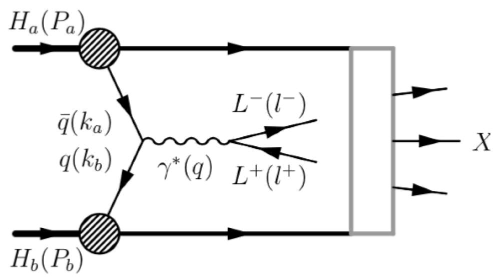

Figure 1.5: Feynman diagram of the Drell-Yan process.

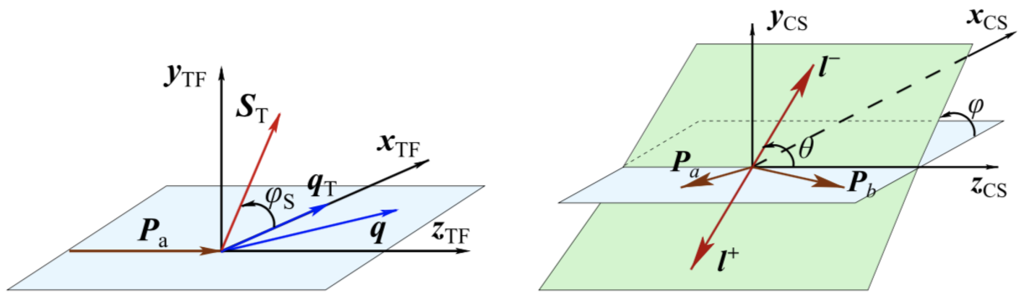

(a) (b)

Figure 1.6: The target frame (a) and the Collins-Sopper frame (b), note the definitions of ϕ_S, ϕ and θ angles.

The single-polarised Drell-Yan process can be generally written down as [30]

$$\begin{aligned}\frac{d^4\sigma}{dqd^3\Omega} = \frac{\alpha^2}{CQ^2}\Bigg\{&(1+\cos^2\theta)F_U^1 + (1-cos^2\theta)F_U^2 \\ &+ \sin 2\theta\cos\phi F_U^{\cos\phi} + \sin^2\cos 2\phi F_U^{\cos 2\phi} \\ + |\boldsymbol{S}_T|\Bigg[&\sin\phi_S\Big((1+\cos^2\theta)F_T^1 + (1-\cos^2\theta)F_T^2\Big) \\ + \sin 2\theta\Big(&\sin(\phi+\phi_S)F_T^{\sin(\phi+\phi_S)} + \sin(\phi-\phi_S)F_T^{\sin(\phi-\phi_S)}\Big) \\ + \sin^2\theta\Big(&\sin(2\phi+\phi_S)F_T^{\sin(2\phi+\phi_S)} + \sin(2\phi-\phi_S)F_T^{\sin(2\phi-\phi_S)}\Big)\Bigg]\Bigg\},\end{aligned} \tag{1.30}$$

where $C = 4\sqrt{(P_a \cdot P_b)^2 - M_a^2 M_b^2}$ is a kinematic factor.

Integrating the Eq. 1.30 over ϕ_S we get the angular distribution of the unpolarised Drell-Yan cross-section [30]:

$$\frac{d^4\sigma}{dqd^3\Omega} \propto \frac{3}{4\pi}\frac{1}{\lambda+3}\left(1+\lambda\cos^2\theta + \mu\sin 2\theta\cos\phi + \frac{\nu}{2}\sin^2\theta\cos 2\phi\right), \tag{1.31}$$

where the angular coefficients λ, μ, ν are defined in terms of the amplitudes F:

$$\lambda = \frac{F_U^1 - F_U^2}{F_U^1 + F_U^2}, \qquad \mu = \frac{F^{\cos\phi}}{F_U^1 + F_U^2}, \qquad \nu = \frac{2F_U^{\cos 2\phi}}{F_U^1 + F_U^2}. \tag{1.32}$$

The coefficients obey so-called Lam-Tung relation: [31; 32]

$$\lambda + 2\nu = 1, \tag{1.33}$$

which is valid at the leading order collinear QCD and has only small next-to-leading order corrections [30]. The Lam-Tung relation has been measured at variety of experiments. The pion induced Drell-Yan experiments [4; 5; 6] show a violation of the Lam-Tung relation and a significant $\cos 2\phi$ modulation. The explanation has been proposed based on the non-zero Boer-Mulders function [11]. Other experiments on p+p and p+d collisions show no such violation [33; 34]. This is not a discrepancy, as the p+p and p+d collisions are sensitive to the sea quarks, where the Boer-Mulders function is expected to be small.

Perturbative QCD calculation [35] performed recently has shown a good description of a majority of the experimental data. This puts constraints on the size of the Boer-Mulders effects. New data from COMPASS and SeaQuest [36] will help to resolve this issue.

In the TMD factorisation at the leading twist the cross-section amplitudes F can be written down [30]:

$$\begin{aligned} F_U^1 &\propto f_{1,a} \otimes f_{1,b}, \\ F_U^2 = F_U^{\cos\phi} = F_T^2 = F^{\cos(\phi\pm\phi_S)} &= 0, \\ F^{\cos 2\phi} &\propto h_{1,a}^{\perp} \otimes h_{1,b}^{\perp}, \\ F_T^1 = F_T^{\sin\phi_S} &\propto f_{1,a} \otimes f_{1T,b}^{\perp}, \\ F^{\sin(2\phi+\phi)} &\propto h_{1,a}^{\perp} \otimes h_{1T,b}^{\perp}, \\ F^{\sin(2\phi-\phi_S)} &\propto h_{1,a}^{\perp} \otimes h_{1,b}. \end{aligned} \tag{1.34}$$

The cross-section can be then rewritten in the terms of asymmetries:

$$\begin{aligned} \frac{d^6\sigma}{dx_a dx_b dq_T^2 d\phi_S d\cos\theta d\phi} \propto \Bigg\{ & 1 + D_{\cos 2\phi}(\theta) \cos 2\phi A_U^{\cos 2\phi} \\ & + |S_T| \Bigg[D_{\sin\phi_S}(\theta) \sin\phi_S A_T^{\sin\phi_S} \\ & + D_{\sin(2\phi+\phi_S)}(\theta) \sin(2\phi+\phi_S) A_T^{\sin(2\phi+\phi_S)} \\ & + D_{\sin(2\phi-\phi_S)}(\theta) \sin(2\phi-\phi_S) A_T^{\sin(2\phi-\phi_S)} \Bigg] \Bigg\} \end{aligned}, \tag{1.35}$$

where we introduced so-called depolarisation factors:

$$D_{\sin\phi_S} = \frac{1+\cos^2\theta}{1+\lambda\cos^2\theta}, \qquad D_{\sin(2\phi\pm\phi_S)} = \frac{\sin^2\theta}{1+\lambda\cos^2\theta}. \tag{1.36}$$

Note that at the leading twist $\lambda = 1$ for Drell-Yan. However, this needs to be verified experimentally and any difference from 1 can lead to somewhat different results for the asymmetries. We will discuss this issue in the relevant section of analysis in Chapter 8.

1.7 J/ψ production in pion-proton interactions

Since the Drell-Yan cross-section is rather small and the statistics obtained at COMPASS in 2015 and 2018 is less than 100 000 events it has been recently suggested by Anselmino et al. [37] to measure the Sivers asymmetry in J/ψ production where abundant statistics is available[11].

The reaction of interest at COMPASS is then:

$$\pi^- \mathrm{p}^\uparrow \longrightarrow \mathrm{J}/\psi + X \longrightarrow L^+ + L^- + X. \tag{1.37}$$

The main assumption of the calculation is the replacement of the virtual photon in the case of ordinary Drell-Yan by the J/ψ which has the quantum number. This leads to replacement of the coupling constants and the replacement of the photon propagator by the massive J/ψ propagator [37].

The reasons for relevance of the measurement for the determination of the Sivers function sign change are the following:

- In the COMPASS kinematics $x_a x_b = M^2_{\mathrm{J}/\psi}/s \approx 0.027$ so the x_a and x_b are large enough so that the $q\bar{q}$ annihilation should then dominate over the gluon fusion.
- Valence quark annihilation should dominate the process as the sea contribution is suppressed.
- The gluon fusion should impact mostly the unpolarised part of the cross-section as the gluon Sivers function is expected to be small.

Based on the results of the Sivers function extracted from the SIDIS data, they predict a significant asymmetry up to 20% which would be easy to observe with the COMPASS data. The Fig. 1.7 shows the relevant predictions.

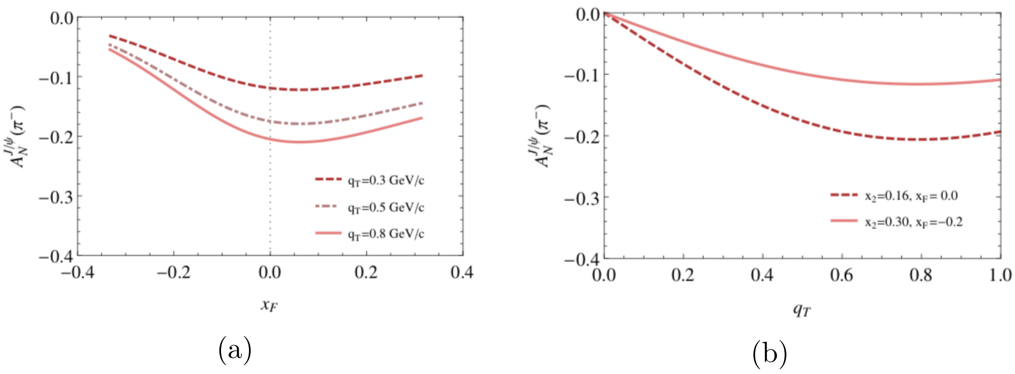

Figure 1.7: Predicted Sivers asymmetry in the J/ψ production.

1.8 Current knowledge

There exists a large amount of data collected over a wide kinematic domain, which allows for rather precise extraction of the unpolarised PDFs. The data come from fixed target experiments (DIS), HERA collider and also LHC experiments.

[11] Approximately by factor 20-30.

A significant improvement should come in the following decade from the Electron Ion Collider (EIC) [38]. One example of the global extraction by NNPDF is shown in Fig. 1.8 [39].

The helicity distributions are less constrained, in particular the gluon helicity and sea distrbutions are rather poorly known. The data are coming mostly from fixed target experiments like SMC, COMPASS and JLab experiments. A recent example of the global extraction is shown in Fig. 1.8 [39].

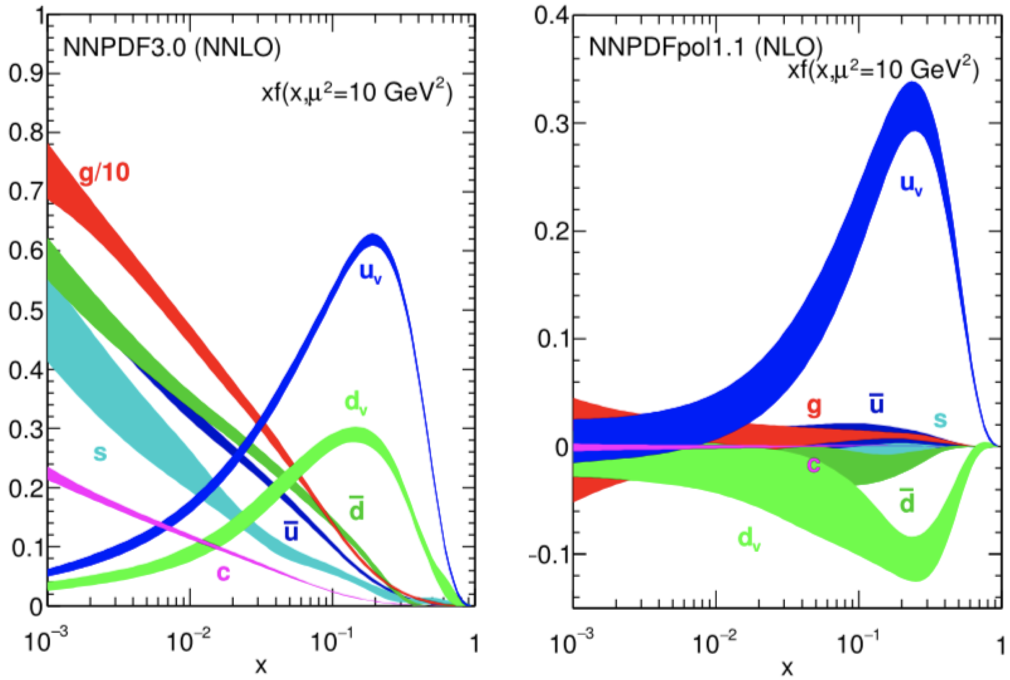

(a) number density

(b) helicity

Figure 1.8: Recent extraction of the collinear PDFs from global data by NNPDF [39].

The transversity distribution measurements pose a different problem. As we have seen it cannot be measured in the inclusive DIS due to being chirally-odd. The two channels accessible experimentally are measurement of the Collins asymmetry[12] in SIDIS (e.g. [40]) and measurement of dihadron asymmetry in SIDIS (e.g. [41])[13]. Both of the measurements need the knowledge of the relevant fragmentation functions, the Collins fragmentation function and the dihadron fragmentation function. Both have been measured in e^+e^- collisions by the Belle collaboration [42]. A recent example of the transversity extraction [43] is shown in Fig. 1.9.

The extraction of the transversity from the Collins asymmetry brings an extra complication, as such an extraction of collinear quantity relies on the TMD framework. Especially the convolution over the quarks transverse momenta posses a problem. In addition the SIDIS and e^+e^- data are taken at very different energies. The extraction might be then also affected by the TMD evolution. The

[12]The amplitude of the $\sin(\phi_h + \phi_S)$ modulation.

[13]Both of the measurements are performed both on proton and deuteron targets to allow for flavour separation. An additional year of deuteron data will be collected by COMPASS in 2021 to improve the significantly lacking statistics [44].

dihadron asymmetry does not have these problem and can be analysed in the collinear framework [43].

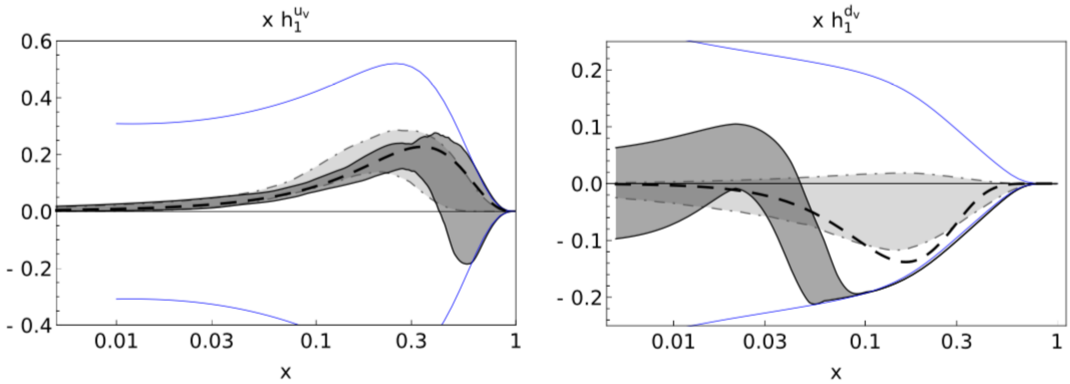

Figure 1.9: Extraction of the valence u and d quark transversity function from Collins asymmetry(2 different extractions, the dark dashed line and light grey bands) and dihadron asymmetry (the dark band) [43].

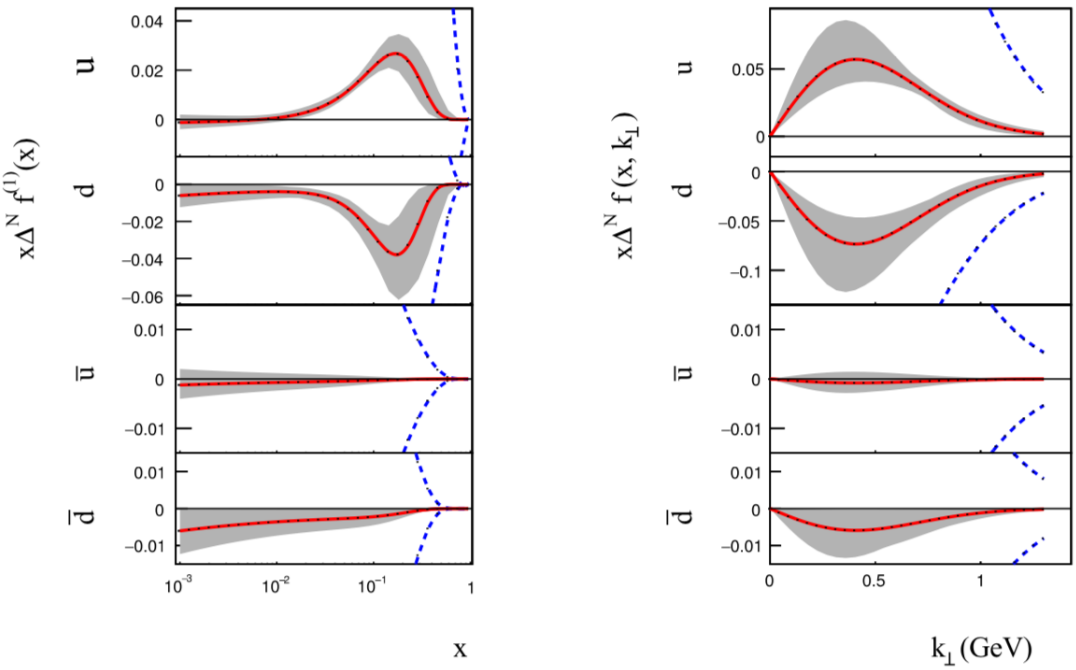

Figure 1.10: Extraction of the first moment of the Sivers function from the available SIDIS data, grey bands correspond to 90% confidence level.

Out of the TMDs only the Sivers function is firmly established so far. We show an example of recent extraction [45] of the first moment of the Sivers function from COMPASS, HERMES and JLab data.

Recently results started to appear to support the predicted sign change of the Sivers function in Drell-Yan with respect to SIDIS. We show here the result from 2015 COMPASS data Fig. 1.11 and STAR data in Fig. 1.12. Both results prefer the sign change hypothesis, although the statistics is limited. Results from combined 2015+2018 COMPASS[14] and the new STAR data should appear soon.

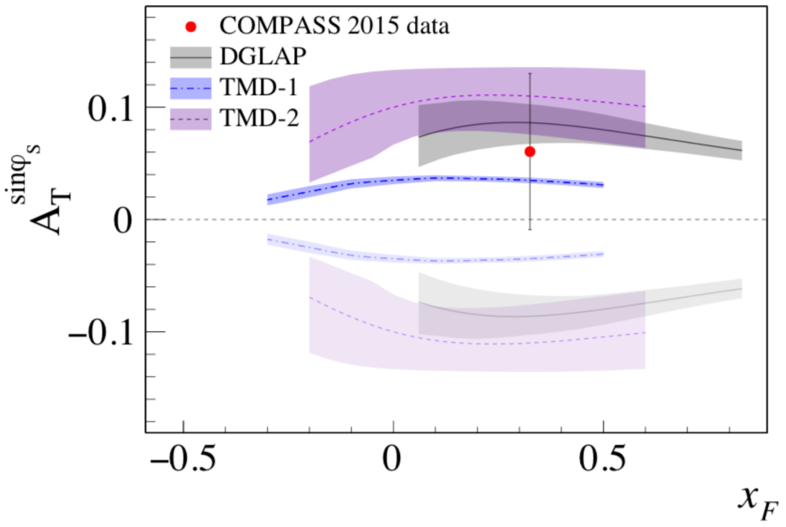

Figure 1.11: Sivers function sign change from COMPASS Drell-Yan data [46], note the three different prediction bands which come from different application of the evolution.

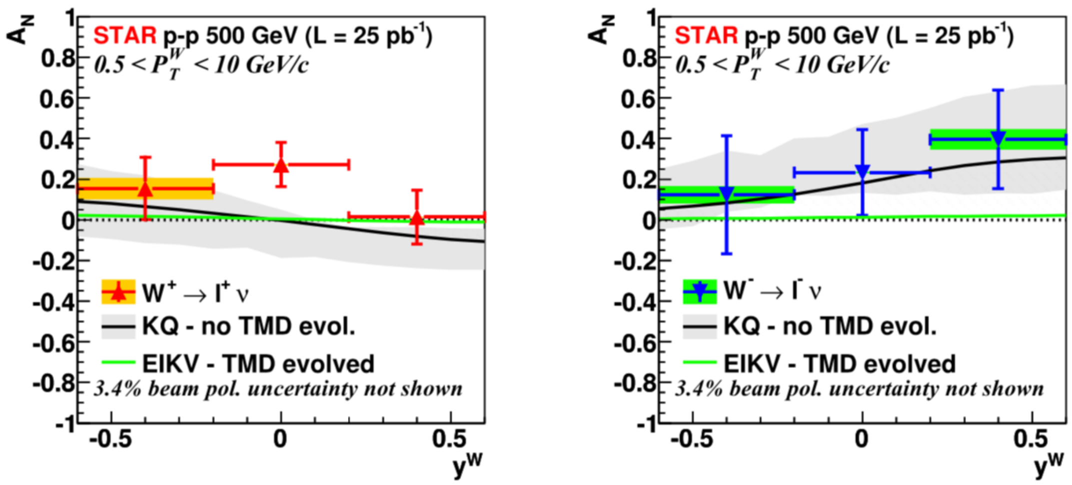

Figure 1.12: Sivers function sign change from PHENIX $W^{\pm}$ production data [47], the KQ and EIKV correspond to different evolutions, note that the $W^{\pm}$ is kinematically far from the SIDIS measurements thus leading to wide spread of the predictions.

[14]Preliminary results from part of the statistics confirm the 2015 measurement.

2. COMPASS experimental setup

2.1 Beamline

The COMPASS experiment is located in the CERN North Area at the M2 beam line. Scheme of the beamline is shown in Fig. 2.1. The primary 400 GeV/c proton beam is slowly extracted[1] from SPS accelerator onto T6 beryllium target. The target station consists of several beryllium plates with transverse dimensions 2×50 mm with variable length. The default target length is 500 mm. Shorter ones (including the Air target) are usually used for detector studies or alignment, where a lower intensity beam is needed.

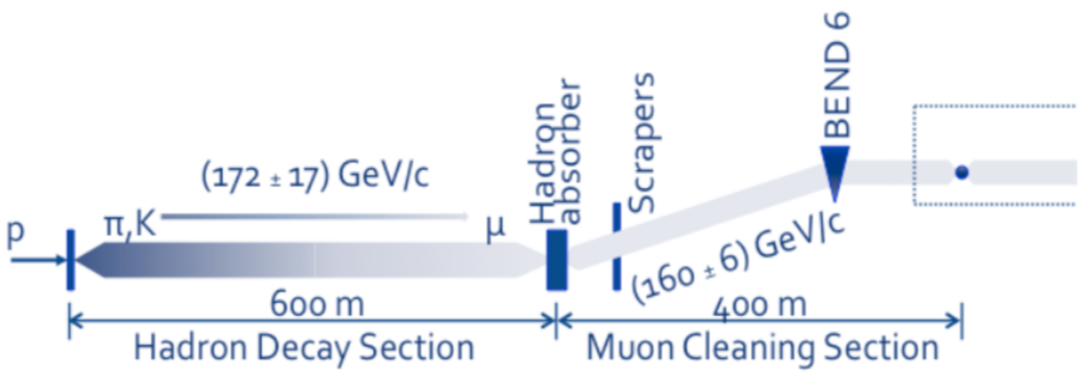

Figure 2.1: Schematic layout of the M2 beamline, setting for 160 GeV muons [48].

The target station is then followed by TAXes[2], dipole bending magnets, focusing quadrupole magnets, movable absorbers, collimators and various beam instrumentation for measurement of the beam profile, position and intensity. The bending magnets serve for steering the beam along the beam line towards the experimental area and also for beam momentum definition. The movable absorbers are moved in the beam if muon beam is used. Thus they determine two main operating modes of the beam line - secondary hadrons, and muon beam from the decaying hadron beam. Due to the parity violation in weak decays of scalar meson the muon beam is naturally polarised. The beam line provides both charges in wide momentum range of about 60-280 GeV/c for muons and about 20-350 GeV/c for hadrons [48]. Maximum intensity for hadron beam is about 1×10^8 particles/s, mainly dictated by radiation protection requirements, and 4×10^7 particle/s for muon beam [48]. For the purpose of the calibration of electromagnetic calorimeters a low intensity electron beam can be provided by inserting an additional target in the beam line.

The last section of the beam line can be equipped with so called Beam Momentum Stations[3] used for precise measurement of the muon beam momentum,

[1] Arbitrarily induced instability in the beam combined with electric field can be used to extract the beam over a period of several seconds, the time period is called spill, usually takes 4.8 s and occurs every 16-50 s.

[2] Movable beam dump/attenuators.

[3] Based on scintillating fibres.

or with CEDAR detectors (see following section) for beam particles identification in the case of hadron beam. Finally, last two quadrupole magnets and two bending magnets are installed on a movable structure called chicane, which is used to compensate the dipole field in the polarised target.

2.2 Beam particle identification

The secondary hadron beams produced in primary proton interactions have different composition depending on the selected beam momentum. Thus a good particle identification is essential for any kind of measurement performed with such a beam. This identification has to be performed rather close to the physics target, as the composition changes along the beamline due to particle decays. As an example the Fig. 2.2 [49] shows the calculated composition of the negative hadron beam used in COMPASS Drell-Yan measurements. It can be seen that for beam momentum of 190 GeV/c any admixture of particles different from pions is very small at the level of 1-2%. This implies that for measurements with kaons a high efficiency of the identification is needed.

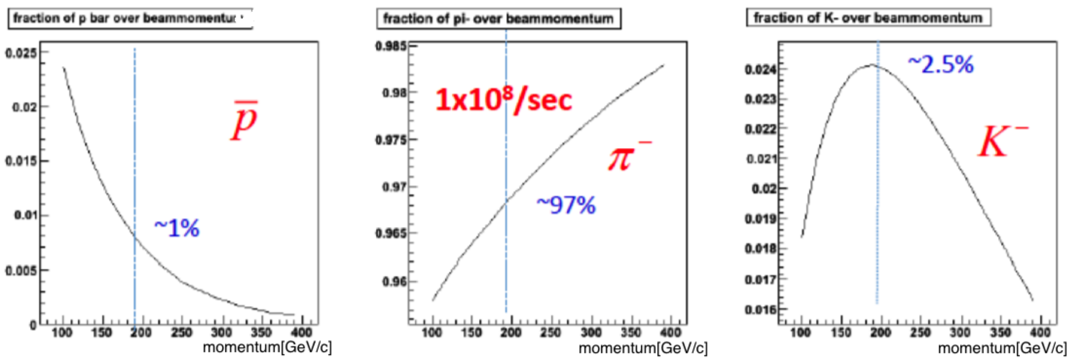

Figure 2.2: Calculated negative hadron beam composition [49].

The particle identification is performed by CEDAR (Cherenkov differential detectors with achromatic focusing [50]) detectors. The detector consists of a high pressure vessel equipped with an optical system which reflects and focuses the Cherenkov light produced by the beam toward a ring composed of 8 photomultipliers (PMTs). The basic working principle is shown in Fig. 2.3. The pressure in the detector can be varied, which is changing the refractive index of the gas if temperature stays constant. This changes the emission angle of the Cherenkov light that allows to tune the detector for identification of given particle species. The Θ angle dependence on the refractive index n is given by the famous simple formula:

$$\cos(\Theta) = \frac{1}{\beta n}. \tag{2.1}$$

The original detectors date back to 70's and they were never intended to be used in the high intensity beam used at COMPASS. This limitation was clearly seen in 2015, as it was not possible to observe any clear separation of kaons from pions. The CEDARs underwent a significant upgrade for 2018 run, with much improved thermal stability[4], and new PMTs, and read-out electronics. The pre-

[4]at the level of 0.1 K as compared to previous several K.

liminary results are showing improvement, no plots are yet available though. It was also observed that the separation efficiency is strongly dependent on the alignment of the detectors. New alignment procedure based on finding the maximum occupancy of the PMTs instead of equilibrating the occupancy was developed.

There are two CEDAR detectors in the beamline in total. Each can be tuned to different particle species. They can be used to either identify both the kaons and antiprotons or by setting them to same species to increase the overall efficiency of either kaons or antiprotons.

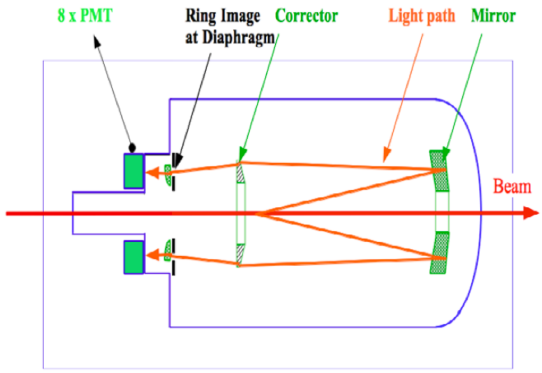

Figure 2.3: Working principle of CEDAR detector.

2.3 Beam telescope

The beam telescope configuration is also depending on the beam used for the type of measurement. In the case of muon beam or low intensity hadron beam running the telescope consists of 3 stations of silicon micro-strip detectors with 4 coordinate views each and 3 Scintillating fibres (SciFis) stations. The micro-strip detectors provide spatial resolution of about 10 μm [51] while the SciFi stations provide an excellent timing resolution of about 400 ps [51].

For the Drell-Yan running with a high intensity hadron beam the silicon stations are not usable, thus leaving only the SciFi stations for the beam reconstruction. In 2015 the beam telescope was equipped with 3 stations with total of 8 coordinate views. For 2018 there were 4 stations with total of 11 coordinate views as the redundancy of 2015 setup proved insufficient for reliable beam reconstruction. The veto hodoscopes, located in the same area, are described in the Section 2.6.

2.4 Target region

The target region provides a great versatility to the COMPASS apparatus. It can be equipped with variety of targets - various solid unpolarised targets, short and long liquid hydrogen targets equipped with recoil proton detector, and proton or deuteron polarised target. During 2010 transversely polarised SIDIS data-taking the target region was occupied by the polarised target in three-cell configuration with ammonia as a proton target. The corresponding setup is depicted in Fig. 2.5. For 2015 and 2018 polarised Drell-Yan run the target was moved 2.3 m upstream with respect to the 2010 setup. A hadron absorber containing additional 10 cm long aluminium target and 120 cm tungsten beam plug was installed behind the polarised target. The hadron absorber is necessary to prevent flooding the tracking detectors with too high rate of secondary hadrons produced in the target. However, this configuration limits the Drell-Yan measurement to muon pairs only. The absorber consists of steel structure filled with alumina in order to minimise the multiple scattering of the muons inside the absorber. The tungsten beam plug serving as beam dump is also used as additional nuclear target for the Drell-Yan. The Fig. 2.4 shows the Drell-Yan target region as well as the structure of the hadron absorber.

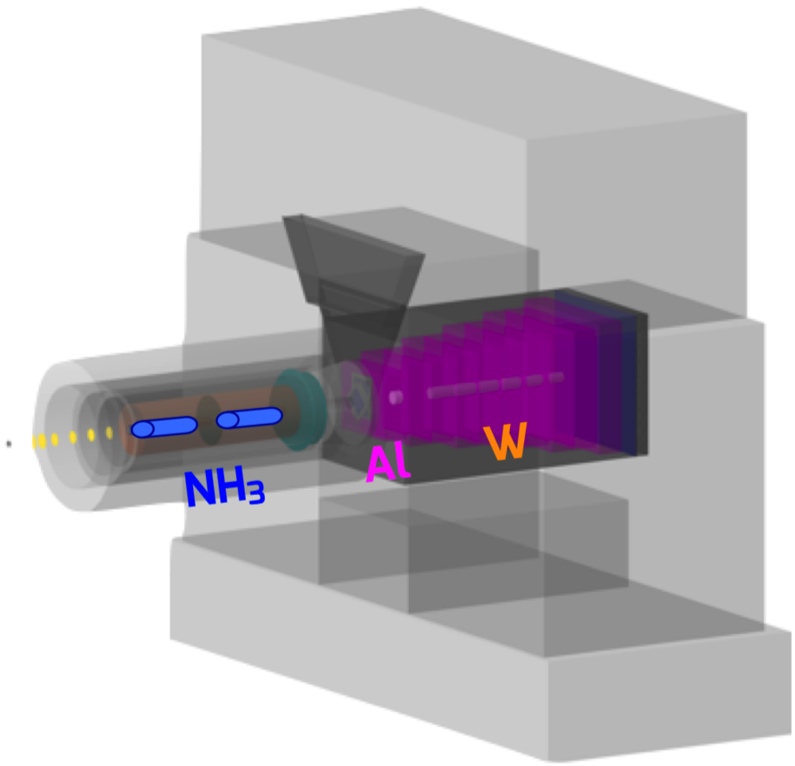

Figure 2.4: Drell-Yan setup target region. Highlighted in blue is the polarised target, the vertex detector in yellow, Aluminium target in magenta, and the hadron absorber in orange with its concrete shielding.

The Space between the absorber and the target magnet was filled with dedicated SciFi-based vertex detector in 2015. It consisted of 3 coordinate views. However, it was not reinstalled for 2018 as its usefulness for track reconstruction proved limited and the installation was not compatible with the extended concrete shielding used in 2018.

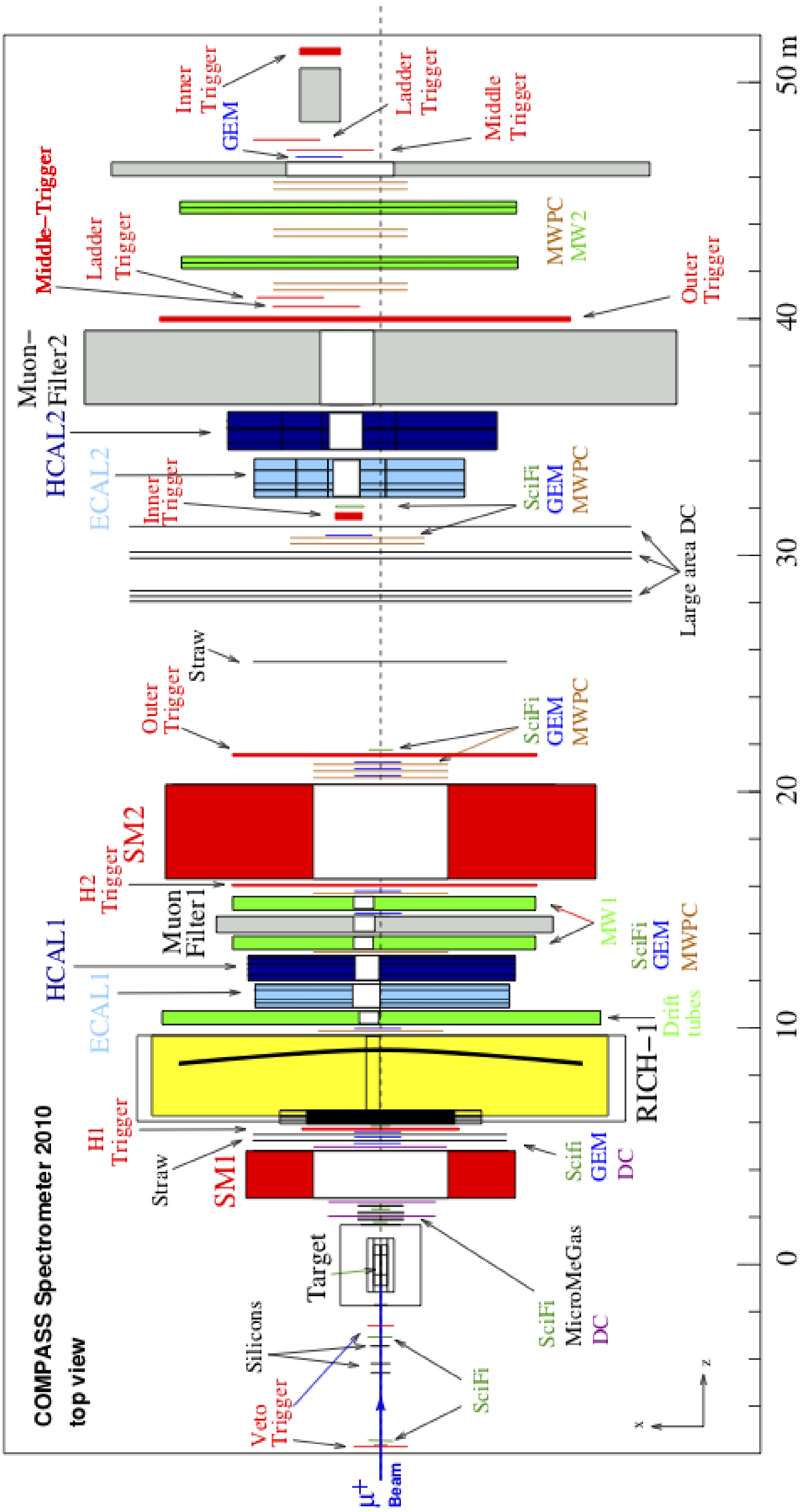

Figure 2.5: 2010 COMPASS spectrometer setup.

2.5 Spectrometer

COMPASS is a two staged magnetic spectrometer. It consists of two parts: the Large angle spectrometer (LAS), and Small angle spectrometer (SAS). Both stages are equipped with tracking and electromagnetic and hadronic calorimeters and muon identification. In addition, the LAS is equipped with Cherenkov detector for hadron identification.

In this section we provide basic information on the detectors used in the COMPASS spectrometer downstream the target. The detectors are ordered mostly as they follow the direction of the beam. We point out the differences between 2010 and 2015/2018 where relevant.

2.5.1 Micromegas detectors

The Micromegas are gaseous tracking detectors with microstrip readout. The gas volume is separated into two sections - conversion and amplification - by metallic micromesh. In the conversion gap the ionisation takes place. The amplification gap with higher electric field produces avalanches, which are then collected on the microstrips. The working principle is illustrated in Fig. 2.6.

The active area is 40×40 cm^2 with 5 cm dead zone in the centre. The obtained resolution is about 80 μm [51]. In 2015 the original detectors were replaced by a new pixelised version, where the central region of 8×8 cm^2 was planted with pixels instead of strips.

There 3 stations of the detectors in the setup each consisting of 4 coordinate views - X, Y, U and V. The U and V vies are rotated by $\pm45°$ with respect to the X view.

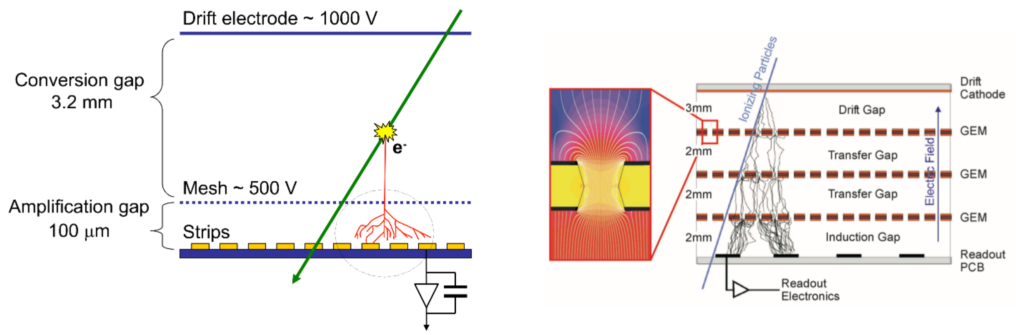

(a) Micromegas (b) GEM

Figure 2.6: Working principle of the Micromegas and GEM detectors.

2.5.2 Drift chambers

The spectrometer is equipped with 3 different types of drift chambers. There are 2 small drift chambers (DC00 and DC01) with dimensions of 180×127 cm^2, 2 large area chambers with dimensions 248×206 cm^2 (DC04 and DC05) and 6 large area chambers(W04/5 reused from the EMC experiment) with dimensions 500×250 cm^2 [51].

The DCs have all four coordinate view - X, Y, U, V, with U an V being tilted by $\pm 10°$ with respect to the X view. The W4/5 have the following view combinations - XY, XU, XV, YU, YV, with U and V views being rotated by $\pm 30°$.

The corresponding resolutions are about 190 μm for the small DCs, about 350 μm for the large DCs and about 500 μm for the W4/5 [51].

2.5.3 Straw trackers

The straw tracker works on the same principle as the drift chambers but the each anode wire has its own gas volume in the shape of straw tube. The tubes are made of two layers of Kapton with thin wire in the centre [51].

Originally there were three stations of Straws in the spectrometer, but two of them were decommissioned between 2010 and 2015 leaving only one station in the LAS.

The detector has four coordinate views - X, Y, U, V. It has dimensions of 323×280 cm^2 with 20×20 cm^2 dead zone. The resolution was estimated to be about 190 μm [51].

2.5.4 Ring imaging Cherenkov detector

The Ring Imaging Cherenkov detector (RICH) works on principle similar as the CEDARs, see Fig. 2.7. The main difference is that the detector is not tuned to one specific species but can detect all the hadrons at the same time. For that is equipped with large area photo-detectors. They were originally all multi-wire proportional chambers (MWPCs) with CsI photo cathode. Later the central part of the system was replaced with multi-anode PMTs. Recently, novel detectors based of thick GEM/Micromegas hybrid were used to replace part of the peripheral chambers [52].

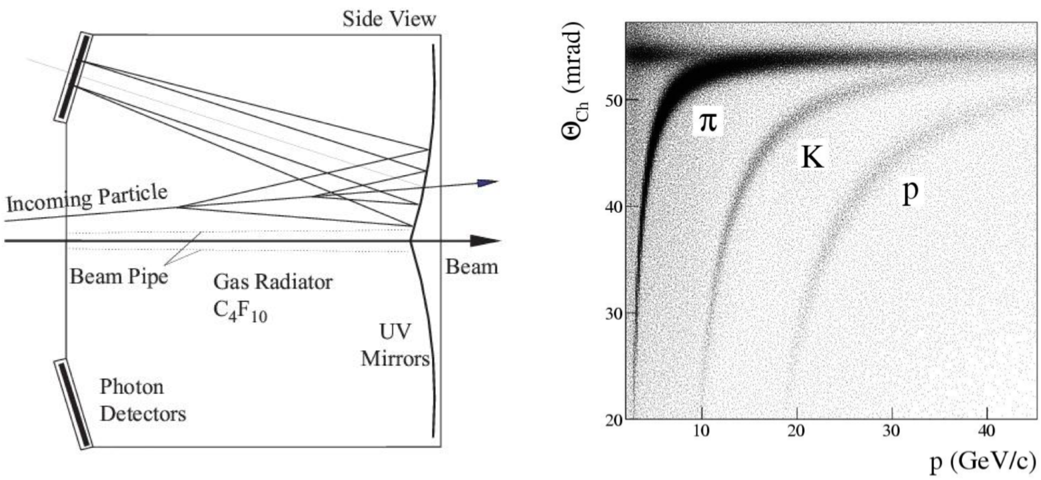

(a) RICH detector

(b) Particle separation

Figure 2.7: The side of the RICH detector and the identification performance of the detector.

The detector can separate pions, kaons and protons in wide range of momenta from about 5-50 GeV/c. The separation is illustrated in Fig. 2.7. Its use in the Drell-Yan measurements is limited to providing additional timing information for the track reconstruction.

2.5.5 Multi-wire proportional chambers

The spectrometer is equipped with 14 MWPCs of 3 different varieties. There is one chamber with coordinates X, Y, U and V. It size is 178×120 cm^2. There are 7 chambers with same dimensions but only 3 coordinates - X, U, V. Finally there 6 chambers with slightly different dimensions of 178×90 cm^2 with either XU or XV views. They all have the same resolution of about 1.6 mm [51].

2.5.6 GEM detectors

The basic principle behind the GEM detectors is a copper coated foil with large number of micro-holes as is shown in Fig. 2.6. When potential difference of about 100 V is applied across the foil it results in avalanche multiplication of the primary ionisation electrons. In case of COMPASS GEMs there 3 such GEM foils. The read out is strip based.

The dimensions of the 31×31 cm^2 with 5×5 cm^2 of area, which is made inactive during normal data taking by lowering the corresponding voltage. In total there are 22 detectors with two coordinate view combined together into 11 stations with all X, Y, U, V views. Typical resolution is about 70 μm [51].

2.5.7 Scintillating fibres

In addition to the beam telescope stations there are 5 to 6 additional stations in the spectrometer. They are mostly equipped with only 2 projections X and Y. There used in the muon program, where they contribute to the tracking near the beam axis [51]. They were not used in the Drell-Yan measurements.

2.5.8 Muon identification

The muon identification is based on measurement of the muon track after it passed significant amount of material. There two muon filters in the spectrometer with corresponding Muon wall detectors.

The first muon filter consists of 60 cm thick iron wall which is from both sides equipped with drift tube-based trackers. Both the stations have two planes of X and Y view. The detector resolution is rather moderate 3 mm [51].

The second muon filter consists of 2.5 m thick concrete wall with drift tube tracker behind it. There are in total 2 sets of X, Y, and V planes. The resolution is about 0.9 mm [51].

Finally there is a third muon filter located near the end of the spectrometer in front of the HI5 hodoscope. It covers the central part where there are holes in both the previous muon filters. This is mainly relevant for very small angle muon scattering and not for the Drell-Yan programme.

2.5.9 Calorimeters

There are two electromagnetic and two hadron calorimeters in the spectrometer. They are ECal1 and HCAl1 LAS and Ecal2 and HCal2 in SAS. The ECal1 is homogeneous calorimeters composed of lead glass modules, both HCAls are sampling calorimeters with shashlyk type modules and ECal2 is combination of lead glass and shaslyk modules [51].

The HCals tuned to MIP signals are the only ones used for the Drell-Yan measurements where they serve as secondary trigger independent of the main hodoscope based trigger. They can be used for evaluating the trigger efficiencies, when independent information is needed.

2.5.10 Magnets

In addition to the target magnet there are two normal conducting dipole spectrometer magnets - SM1 in the LAS and SM2 in the SAS.

SM1 has central hole of 229×152 cm^2 matching the ± 180 mrad acceptance of the target magnet. It has field integral of 1 Tm [51]. SM2 has central hole of 2×1 m^2 and field integral of 4.4 Tm [51].

2.6 Trigger system and Data Acquisition

2.6.1 Trigger system

The basic idea behind the trigger system is target pointing. The system is based on coincidences between several pairs of scintillating hodoscopes segmented in vertical direction. The hodoscopes vary in size and position, which results in different kinematic coverage. The logic is set between different slabs of different hodoscopes in a way that only track, which originates in the target region, could have produced the given coincidence. This coincidence logic is described by the coincidence matrices. The principle of the coincidence matrix is shown in Fig. 2.8. This configuration is used to trigger on scattered muon in DIS measurements or as a single muon trigger in Drell-Yan measurements.

There are additional hodoscopes, which are segmented in horizontal direction. They trigger according to the scattering angle. Finally, the calorimeters can be used for triggering on photons (ECals) or on either hadrons or MIP signal of muons (HCals).

Important part of the trigger system is the veto system. It is basically a trigger, which is in anti-coincidence with the physics trigger. It triggers on beam tracks or halo tracks, which are not hitting the target.

For the Drell-Yan measurements there is an additional coincidence logic, that combines two single muon triggers providing the dimuon trigger. There were three dimuon trigger used in 2015 and 2018 - the LAS×LAS trigger, Outer×LAS trigger and Middle×LAS trigger.

The main trigger elements and their position in the spectrometer are shown in Fig. 2.9.

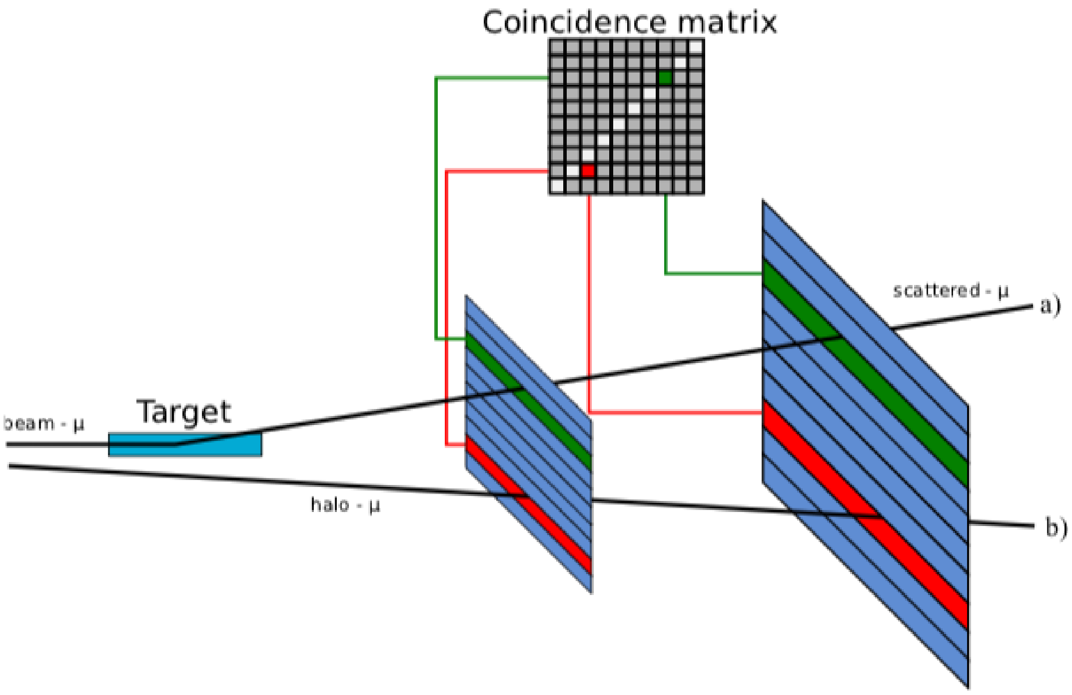

Figure 2.8: Principle of the trigger matrix for for target pointing [53].

2.6.2 Data Acquisition

All detectors are equipped with Front End Electronics cards (or simply frontends, all custom designed according to the needs of the experiments, most of them are described in Ref. [51]) grouping together multiple analog channels (e.g. 64 or 192 wires from drift chambers or multi-wire chambers, etc.). The electronics take care of amplification and digitisation of the signals. Multiple cards (typically one chamber or several detector planes) are multiplexed together in dedicated multiplexer card located nearby given detectors and finally the data are transmitted via optical fibres to the crate with Data Acquisition (DAQ) system located outside of the experimental area. All the frontends are synchronised together with the DAQ via Trigger Control system (TCS). TCS also provides basis for the dead time setting, which is given by three numbers e.g. 5-40-250. The numbers are the time intervals in μs during which 2, 3 or 10 trigger signals can occur.

The DAQ consists of 6 multiplexers with 15 input ports. The multiplexer outputs are then connected to the switch, which is responsible for the event building (i.e. putting together all the data from detectors for given event) and then send to one of 4 readout engines. The data are stored in chunks of size of 1 gigabyte and are quasi-online transferred to the tape storage CASTOR.

The current system is used since 2014 and replaced the original DAQ used until 2012. The original system used few dozens of event-building computers and the event building was done by software. The current system is generally much more reliable and in 2017 it reached excellent up-time performance better than 99% [54].

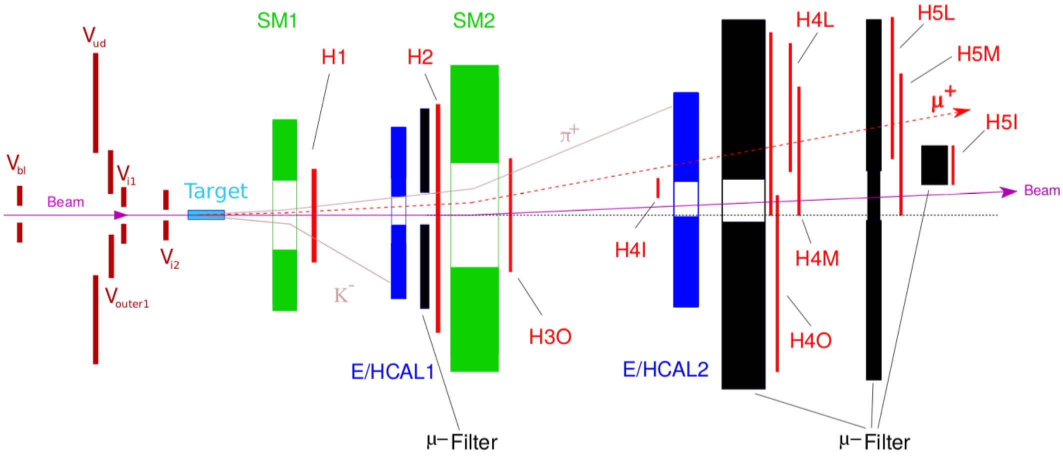

Figure 2.9: The trigger elements in the spectrometer [53].

2.7 Data processing and reconstruction

In order to be able to perform a physics analysis of the data several additional steps are needed.

First an alignment file is needed. The alignment file specifies the positions of all detectors in the area. Since the required resolutions are impossible to obtain with normal survey measurements dedicated measurement with special beam is needed. Muon beam with low intensity (of the order of 10^6/s) is used. In order to get proper illumination of the detectors active area the beam is defocused by switching off the last quadrupole magnet in the beam-line. Then dedicated data are taken in two configurations - with spectrometer magnets off, and magnets on. Then in the offline analysis with special iterative procedure the positions of detectors active area are obtained with sub-millimetre precision.

The reconstruction is done using software package called Compass Reconstruction Algorithm Library (CORAL) [51]. CORAL makes use DAQ Decoding library to access the raw detector hits and calibration data stored in MySQL database together with the alignment file to reconstruct the data and produce the mini DST (Data Summary Tree) files [51].

Reconstruction proceeds in several steps. It starts with reconstructing the straight tracks, then bridging through magnetic field and determining the momentum, track fitting and finally a vertex finding and fit. Separately the clusters in calorimeters are reconstructed and likelihoods determined for the particle identification using the RICH detector. As the full problematic of the reconstruction is far beyond the scope of this text we refer to [51] for more details.

The miniDST files, which are the output of the reconstruction, are used for the user analysis within the framework of the PHAST software [55]. They contain information on the tracks, vertices, calorimetric clusters, particle IDs, various setup information, etc.

2.8 Data taking, performance and resolutions

2.8.1 Data taking

Although the DAQ can in principle run continuously, the data are split into so called runs for practical purposes. Each run is set to be either 100 spills (2010 data) or 200 spills (2015 and 2018) long. This be even shorter in practice in case some detector problem occurs.

The polarised measurements are divided into periods, which are usually two weeks long. In the middle of each period, the polarisation reversal of target is done. This is usually coincident with the accelerator stops in order to minimise the loss of beam for physics. Alignment of calibration runs can be taken in parallel as well, since the polarisation reversal usually takes at least 24 h compared to usual accelerator stops of 12 h.

They key requirement for each period is to keep the spectrometer in as much stable running conditions as possible. In principle no changes are allowed to settings of the detectors and beam. Accesses should be minimised to reduce the risk of moving any detector accidentally. Each period is scrutinised for stability latter on during the analysis. We will briefly discuss this issue in latter chapters.

In general the data taking efficiency over the years remains constant at about 80%, meaning that during the beam time useful physics data are taken in 80% of the time.

2.8.2 Performance and resolutions

The reconstruction efficiency is above 90% for tracks with momentum above 5 GeV/c. The momentum resolution varies between 0.5-2% [51]. This depends on the quality of the alignment and calibration and can be also affected by detector problems.

The main difference between the DIS and Drell-Yan measurements is the presence of the hadron absorber. While designed to minimise the multiple scattering of the muons, it still significantly affects the experimental resolution.

In the latter chapters is shown that the dimuon invariant mass resolution varies from about 50 MeV/c^2 in case of no absorber to about 200 MeV/c^2 with the absorber present.

The vertex resolution remains below 1 mm in the transverse plane. The resolution deteriorates significantly in the z-direction from less than 1 cm to about 10 cm [56]. The angular variables are also significantly affected. In particular the azimuthal angles have resolution about 0.2 rad [56].

3. COMPASS polarised target

3.1 The need for the polarised target

It is clear from chapter 1 that the ideal target would be large and contain one nuclear species with all the nuclear spins aligned in one direction, i.e. 100% polarised[1]. However, it is impossible. Unfortunately there exists no pure element, which could be polarised. Instead, we have to resolve to using more or less complex compounds like e.g. ammonia (NH_3), deuterated lithium (^6LiD), butanol (C_4H_9OH), etc. To take into account that not all the nuclei in the given material can be polarised the so called dilution factor f is introduced, which gives the fraction of polarisable nuclei in the material. We will come back to his point later on. Moreover, the maximum polarisation never reaches 100%. This means that what we measure are actually so-called raw asymmetries and we need to correct them for the dilution factor and polarisation to get the physical quantities:

$$A = \frac{A_{raw}}{fP}. \tag{3.1}$$

As we can see from the formula, the highest possible polarisation is needed, together with the highest possible dilution factor to reach the smallest uncertainty of the asymmetry. We will describe how to reach a high polarisation in suitable materials, how to measure the polarisation, the choice of the suitable material, as well as the realisation of the polarised target in the COMPASS experiment in the following sections.

3.2 Dynamic nuclear polarisation

When a system of spins 1/2 is put into magnetic field B, the Zeeman splitting occurs. Then the polarisation P can be defined as:

$$P = \frac{n^+ - n^-}{n^+ + n^-}, \tag{3.2}$$

where n^+ is the number of spins, which are parallel to the field B, and n^- the number of the spins, which are anti-parallel to the field. In general case of any non-interacting non-zero spins the polarisation is given by the Brillouin function, which in case of spins 1/2 simplifies to:

$$P = \tanh(\frac{\mu B}{kT}), \tag{3.3}$$

where μ is the magnetic moment related to the spin, and k is the Boltzman constant. It is clear that in order to achieve high polarisation values a large magnetic field B and a very low temperature T is needed. For example if $B = 10$ T and $T = 10$ mK, a polarisation of 90% can be reached for protons. This brute force method is not usually very practical, as the conditions are quite difficult to reach, and also the relaxation time for reaching the equilibrium in the nuclear

[1]Polarisation is a number between -1 and +1 but it is usually expressed as $P \times 100\%$.

system is quite long. Fortunately another method exists, namely the Dynamic Nuclear Polarisation (DNP), where a high degree of polarisation can be reached with moderately high field values and temperatures. (In COMPASS case 2.5 T field is used and temperature of about 300 mK). The basic idea is to transfer the high electron polarisation (which is above 99% at 1 K according to the eq. 3.3) to the nuclear system.

In the following section we will describe briefly the so-called solid state effect, which is rather simple concept for describing the DNP, but unfortunately its assumptions are rarely satisfied with solid state targets. Then the basic idea of the spin temperature concept as an underlying theory of DNP will be given. We refer to Ref. [57] for comprehensive overview of the topic.

3.2.1 Solid state effect

Lets consider an ensemble of nuclear spins I and of electron spins S. The system can be described by the following Hamiltonian:

$$H = H_{ZI} + H_{ZS} + H_{II} + H_{SS} + H_{IS} = H_{RF}, \tag{3.4}$$

where the H_{ZI} and H_{ZS} are the Zeeman terms of nuclear and electron systems, the H_{II} and H_{SS} are the dipole interactions in the nuclear and electron systems respectively, the H_{IS} is the electron-nucleus dipole interaction, and H_{RF} is the possible external radio-frequency field interaction.

If we consider one electron-nucleus pair, there are four pure states without the dipole interaction H_{IS}. They are $|{+}{+}\rangle$, $|{+}{-}\rangle$, $|{-}{+}\rangle$ and $|{-}{-}\rangle$, where the sign + denotes the spin parallel to the magnetic field and - the spin anti-parallel to the magnetic field. We can now consider the electron-nucleus dipole interaction as a perturbation and calculate the perturbed states $|a\rangle$,$|b\rangle$, $|c\rangle$, $|d\rangle$ and transition probabilities. Here we only summarise the main results and refer to Ref. [57] for the full theoretical treatment.

As shown in Fig. 3.1 the dipole interaction allows for simultaneous flip of the nuclear and electron spins when the system is irradiated by radio-frequency field with frequency $\omega_e \pm \omega_N$, with ω_e and ω_N denoting the nuclear and electron Larmor frequency respectively. From that the basic idea of solid effect follows: The material in static magnetic field is irradiated with radio-frequency field with the given frequency and mutual flip-flops of the electron-nucleus pair occur. The electron relaxation is much faster than the nuclear flips-flops can occur, which leads to the polarisation build-up. In addition, the so-called spin diffusion occurs with flip-flops between nuclei thus enhancing the polarisation as well.

The above mentioned effect works only if the width of the electron spin resonance line is much smaller than the nuclear Larmor frequency. However, this is almost never fulfilled due to the broadening of the electron line caused by the chemical neighbourhood of the electrons [57].

3.2.2 Spin temperature

The main assumption of the spin temperature theory is that the system of electron spins can be considered isolated and the system evolves toward equilibrium with spin temperature T_S. To make the assumption valid the spin-spin relaxation

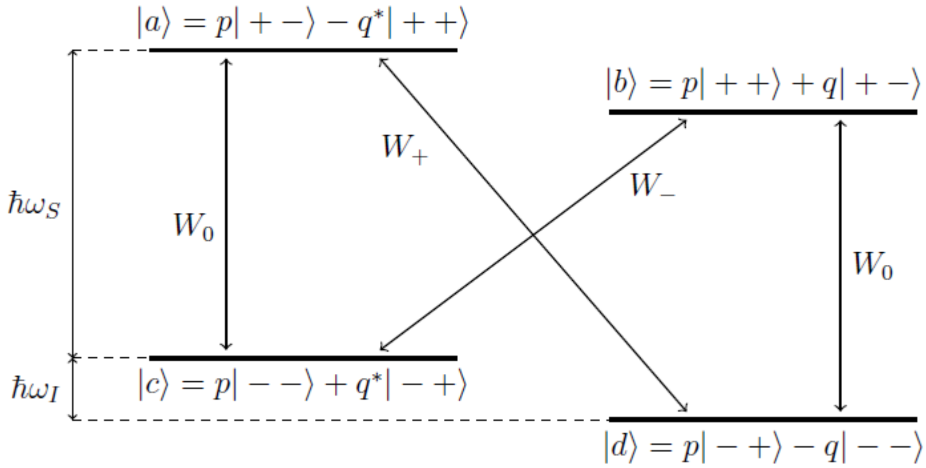

Figure 3.1: Energy levels of electron-nucleus pair coupled by dipole interaction. The W_+ and W_+ show the possible transitions for the positive and negative polarisations respectively. The p and q are the mixing coefficients given by the perturbation theory [57].

time T_2 needed by the electron system is much shorter than the spin-lattice relaxation time T_1. That means that during the time T_1 the lattice temperature T is actually different from the spin temperature T_S. The spin-lattice relaxation can be then understood as equalisation of the two temperatures [57].

Since the spectrum of the electron spins has an upper limit, the spin temperature T_S can be both negative and positive. See Fig. 3.2 as illustration. Since the spin system is thermally connected to the nuclear system, the DNP can be understood as cooling of the nuclear system via cooling of the electron system. Cooling of the electron system is then to be understood in the sense of lowering $|T_S|$. Polarising nuclear spins is then equivalent to approach the zero temperature from negative temperature for a negative polarisation and vice versa for the positive polarisation.

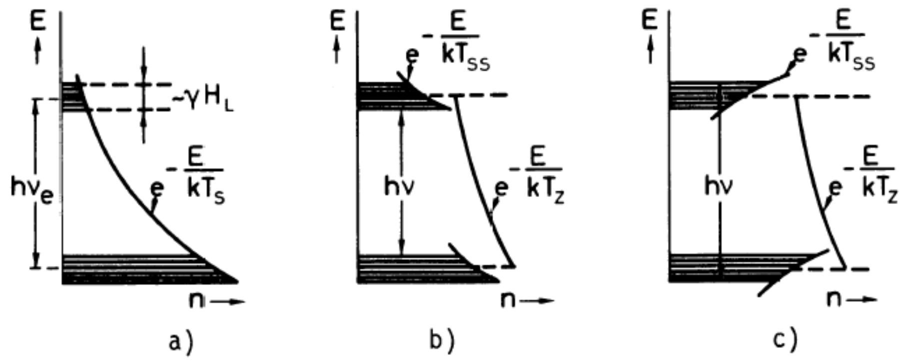

Figure 3.2: Illustration of the spin temperature: a) equilibrium, b) positive temperature of electron spins, c) negative temperature of the electron spins.

3.3 Polarisation measurement and TE calibration

There are two possibilities how to measure nuclear polarisation. The first is a scattering method, however this one is extremely impractical and close to impossible to use at COMPASS. Second method, which is widely used in this kind of experiments, is continuous nuclear magnetic resonance (NMR). The basic principle being the fact that the area of the measured NMR absorption curve is proportional to the polarisation.

It can be shown [58] that the polarisation P can be expressed by the following formula:

$$P \propto \int \chi(\omega)'' d\omega, \tag{3.5}$$

where $\chi(\omega)''$ is the frequency dependent absorption part of the nuclear susceptibility. In addition, the measured NMR voltage V obeys the following relation:

$$V(\omega) \propto \chi(\omega)''. \tag{3.6}$$

3.3.1 TE calibration

As was already mentioned the polarisation of an ensemble of particles with spin-1/2, which is at equilibrium in magnetic field B and temperature T, can be calculated by the formula 3.3. If we compare the result of this calculation with the NMR measurement, we can obtain calibration constant, which can be then used even for the situation when DNP is performed. Then the formula 3.3 is no longer valid as the system is far from thermal equilibrium.

There is unfortunately one practical issue. Since the target material is not suspended in vacuum, the NMR measurement will also see the contribution from other nuclei around, especially in the target holder. This problem can be dealt with in two ways. The first solution is that the target holder is made of material, which is not NMR active (in our case does not contain free protons), the second method is that the background is measured separately and then subtracted from the signal. For the 2010 configuration the target holder was made from polyamide mesh, which contains free protons. The overall contribution of the empty TE calibration was about 10% [59]. For 2015 and 2018 the target holder was made from PTFE, which contains no free protons. The residual contribution from cable insulation and possible water ice was found to be about 1% [60].

The TE signals are generally rather noisy due to their low amplitude. Usually 4 signals are averaged during the measurement of enhanced polarisation, 16 signals are averaged for TE signals and 64 are used for empty TE signals. The Fig. 3.3 shows example of the TE and enhanced signals. The TE measurement is performed for several temperature points. They are usually about 1.5 K, 1.3 K and 1 K. The temperature steps are given by the different pumping speed available in the system.

The analysis of the data then proceeds in following steps [59] for every NMR coil:

- Subtraction of the Q-curve from the raw signal

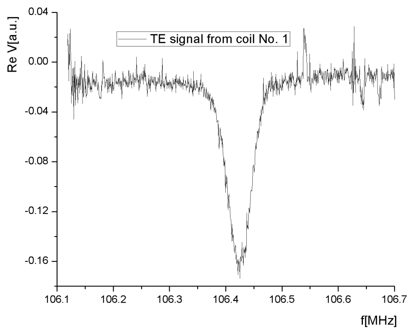

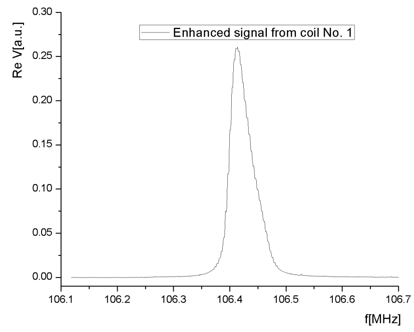

Figure 3.3: Comparison of NMR signals for enhanced polarisation of about 80 % and TE signal at 1 K.

- Removal of bad data (shift of Q-curve)
- Linear fit of the residual baseline and its subtraction
- Integration of the signal
- Averaging of all the measured areas for given temperature
- Fit the final areas with $1/T$ Curie law dependence, see Fig. 3.4 as example
- Correction for the gain and non-linearity.

The TE calibration is performed usually once before the start of the run and once after the end of the run.

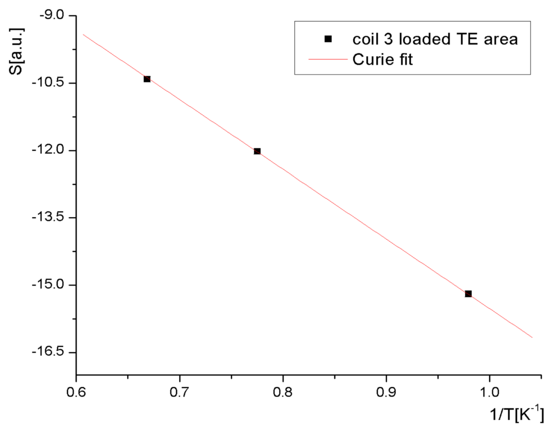

Figure 3.4: Curie fit of measured calibration points.

3.4 Dilution refrigerator

The working principle of dilution refrigerator (DR) is based on the phase diagram of ^{3}He/^{4}He mixture shown in Fig. 3.5. When mixture of ^{3}He/^{4}He is cooled down below 1 K, a phase separation occurs. The ^{3}He rich phase floats on ^{4}He rich phase, which due to finite solubility of ^{3}He in ^{4}He always contains

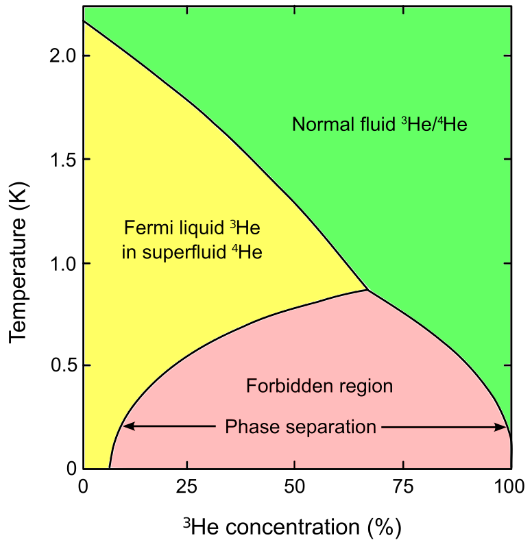

Figure 3.5: Phase diagram of ^{3}He/^{4}He.

at least 6% of ^{3}He even in the limit of zero temperature. If we start pumping the vapours of the mixture then, due to much higher pressure of ^{3}He at this temperature, mostly ^{3}He will be removed from both phases. However, to keep the ^{3}He concentration in the dilute phase the ^{3}He is forced to pass from the concentrated phase through the boundary of the phases. And since the ^{4}He represents a vacuum for ^{3}He, it will result in cooling. If we keep the pumped ^{3}He circulating back to the mixture, the refrigerator will operate in the continuous mode. If the ^{3}He is not returned, then we talk about a single shot regime, which can reach lower temperature, but the cooling stops after all ^{3}He is removed from the system. The cooling power $\dot{Q}$ of the dilution refrigerator can be deduced easily from enthalpy balance [61] and is given by the following equation:

$$\dot{Q} = \dot{n}_3[H_D(T_{ex}) - H_C(T_{mc})] - \dot{Q}_{leak} - \dot{Q}_{beam}, \tag{3.7}$$

where $\dot{n}_3$ is the ^{3}He flow, the H_D is the enthalpy of the dilute phase, H_C is the enthalpy of the concentrated phase, $\dot{Q}_{leak}$ is the heat leak given mostly by the imperfect insulation in the beam entrance, and $\dot{Q}_{beam}$ is the incoming heat from the beam. The beam induced heat varies from about 1 mW for muon beam and goes up to 5 mW for the hadron beam, thus causing a significant raise of the temperature up to 120 mK. The cooling power of the COMPASS DR as a function of temperature is shown in Fig. 3.6. More details on the principles of a DR can be found in Ref. [61].

The scheme of the COMPASS DR is shown in Fig. 3.7. It consists of the separator, the evaporator, the still and the mixing chamber, all interconnected with several heat-exchangers and shielded by several thermal screens. The ^{4}He is transferred from a large buffer dewar to the separator, where the phase separation occurs. The gas is used for pre-cooling the screens while the liquid goes mainly to the evaporator, which is pumped by combination of rotary and Roots pump to achieve temperature of about 1.5 K. The temperature of the evaporator is measured by RuO_2 thermometers on the top and the bottom and by a diode thermometer at the bottom. It is also equipped by capacitive level gauge, which

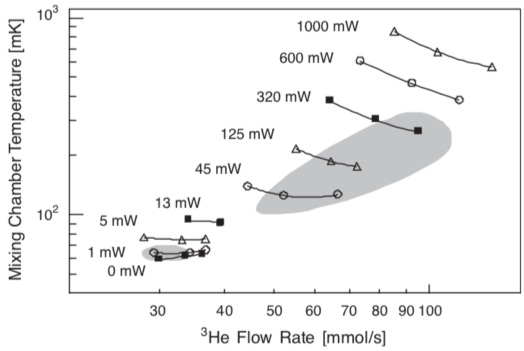

Figure 3.6: Cooling power of the COMPASS dilution refrigerator as a function of temperature.

was not used in 2015 and 2018 runs. The evaporator pre-cools the ^{3}He circuit through several heat exchangers.

The still is connected to the mixing chamber. It contains the still heater, which is used to control the circulation of the ^{3}He and consequently the cooling power. The still is pumped by 8 Roots pumps in series with total pumping speed of 13 500 m^3/s. The ^{3}He circuit is also equipped by LN_2 trap and zeolith filters for purification of the circulating gas. The mixing chamber is made of glass-fibre epoxy and has about 5 l volume. The temperature in the mixing chamber is monitored by several carbon resistor thermometers (Speer 220 Ω).

The refrigerator working mixture contains roughly 8000 l of ^{4}He and about 1200 l of ^{3}He (volume given at room temperature and pressure) according to inventory made during July 2013. The rate of ^{3}He circulation is between 25-60 mmol/s, depending on the mode, i.e. polarising or frozen spin mode. The consumption of liquid ^{4}He is about 15-40 l/h. It is worth mentioning that the price of ^{3}He is about 3 MCHF, which brings the need for extra care when operating the system. The ^{3}He is stored in several steel tanks with pressure below atmospheric. The system is thoroughly leak-checked before cool-down is started. In case of sudden overpressure in the system caused by blockage for example, several overpressure valves will allow for safe recovery of the operating mixture back to the storage tanks.

The operation is monitored by a PLC system, which collects data from all the pressure gauges, flowmeters and thermometers installed in the refrigerator system. The system is connected to the main Detector Control System (DCS) and alerts the shift crew by an audible alarm and sends a text message to an expert directly. More details can be found in Ref. [62].

3.4.1 Target holder

An important part of the refrigerator system is the target holder. After pre-cooling to 80 K it is filled with the target material and inserted into the horizontal dilution chamber of the fridge. The vacuum seal is done using indium on the target holder pressed against sharp edge in the fridge.

The target holder itself consists of several parts. First is the vacuum volume with 100 μm thin stainless steel windows in the path of the beam. Second is the aluminium support piece with kevlar tube connected to it, which contains

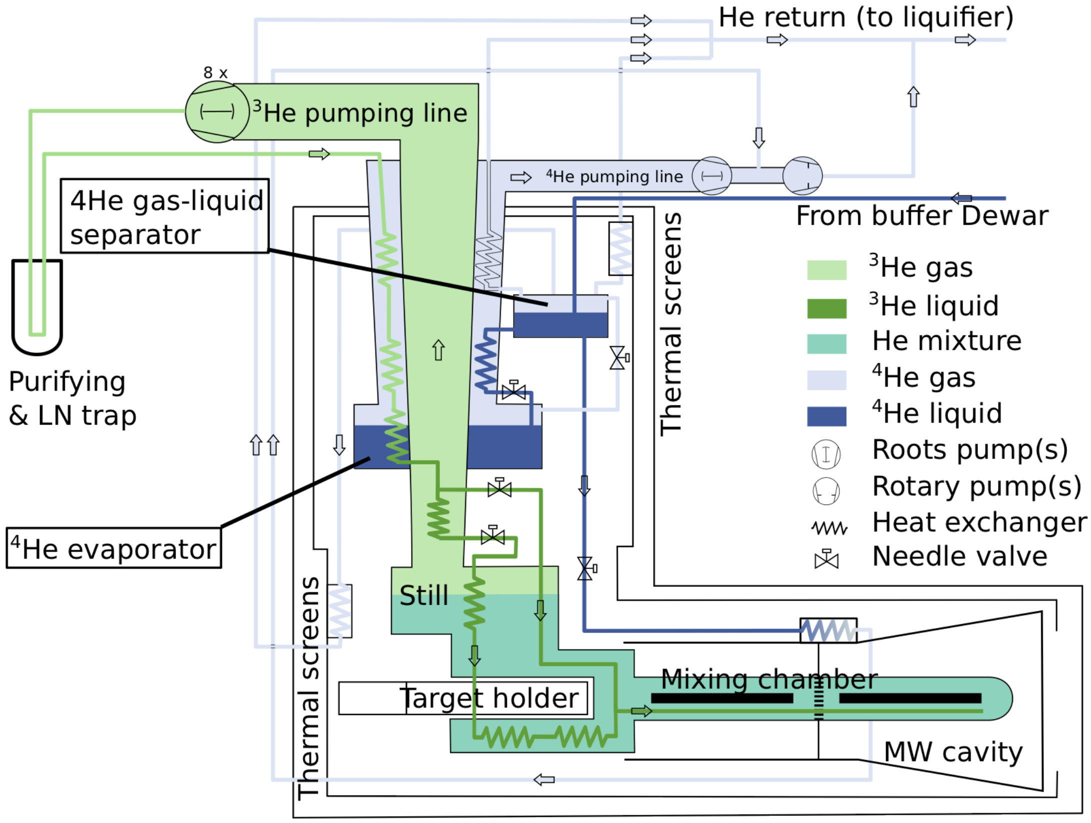

Figure 3.7: Scheme of the dilution refrigerator, the monitoring sensors are not shown for clarity.

the target cells. The target cells are equipped with lids in order to allow for the material filling. In addition, the cells are equipped with the NMR coils and temperature sensors. The upstream part of the target holder also contains small ^{3}He bulb as a part of the ^{3}He vapour pressure thermometer used during the TE calibration.

3.5 Magnet system

COMPASS superconducting polarised target magnet has been put into operation during the year 2005 and was heavily refurbished in 2012-2014, see Ref. [63]. The Fig. 3.8 illustrates the layout of the magnet.

The magnet consists of two main coils - the solenoid and the dipole. The solenoid creates longitudinal field of 2.5 T, which is homogenised by 2 compensation coils and 16 trim (or shim) coils to about 10^{-5} T. The solenoid can be used both as polarising coil and holding coil for longitudinal measurements. The dipole consists of two saddle coils which provide field of 0.63 T with homogeneity of about 10%. Since it is used only as holding coil for transverse measurements this homogeneity is sufficient.

The two coils share the same cryostat equipped with ^{4}He level gauges made of a superconducting wire. The cryostat is shielded by a thermal shield,which is kept at about 80 K by Cryomech PT-60 cryocooler [64]. Then several layers of

[2]Taken from Ref.[63].

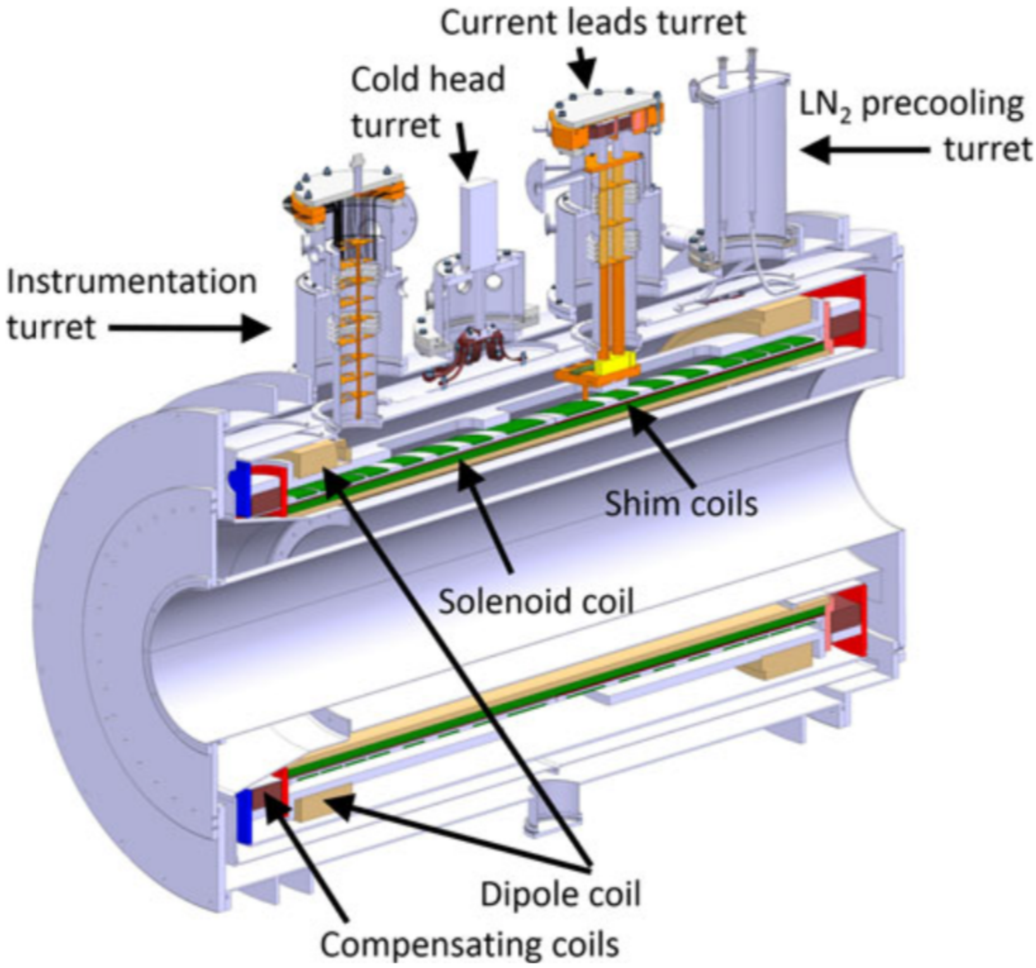

Figure 3.8: Target magnet layout[2].

super-insulation follow. The isolation vacuum is shared between the magnet and the refrigerator and is kept at pressure of roughly 10^{-6} mbar. Consumption of liquid ^{4}He is about 25 l/h.

Important part of the magnet system is the Magnet Safety System (MSS), which has to stop the magnet in a safe way in case of an accident. For less severe problems like a power cut or low liquid ^{4}He level the slow discharge is initiated. This means that the contactors are opened and the current from either the solenoid or the dipole is dissipated through 4 diodes. This takes about 10 minutes. In case of quench of the magnet the fast discharge has to be initiated. For the dipole, where the stored energy is considered low (about 0.5 MJ), this is similar to a slow discharge. For the solenoid it is much different due to the large energy stored in the coil (about 3.3 MJ). If the system detects a quench (by measuring balance of the voltages across the different parts of the coil) then the current is dissipated through a resistor and quench heaters are fired. This results in a boil-off of the ^{4}He in the cryostat, but the energy is dissipated within 20 s preventing damage of the main coil.

Second important function of the MSS is to prevent the two coils to be ramped up simultaneously to a full current, as the Lorenz force between them would tear apart the magnet. Maximum current allows simultaneously corresponds to field of 0.5 T, which is used during the so-called field rotation.

The field-rotation allows to transition from a longitudinal magnetic field to the transverse field without losing the polarisation. This is achieved by lowering the longitudinal field to 0.5 T, ramping up the transverse field to 0.5 T, ramping down the longitudinal field to zero and finally reaching the nominal transverse field of the dipole. During the rotation the trim coils are set to an opposite polarity in order to make the longitudinal field as inhomogeneous as possible. This is necessary to avoid the collective quantum effect of super-radiance which might destroy the polarisation.

3.6 Microwave system

In order to achieve opposite polarisations in the target cells two microwave power sources operating near 70 GHz are used. One operating on the upper edge (negative polarisation) of the paramagnetic spectrum, and the second one at the lower edge (positive polarisation) of the paramagnetic spectrum. The system allows for fine tuning of the power and frequency needed during the course of polarising. The system is depicted in Fig. 3.9.

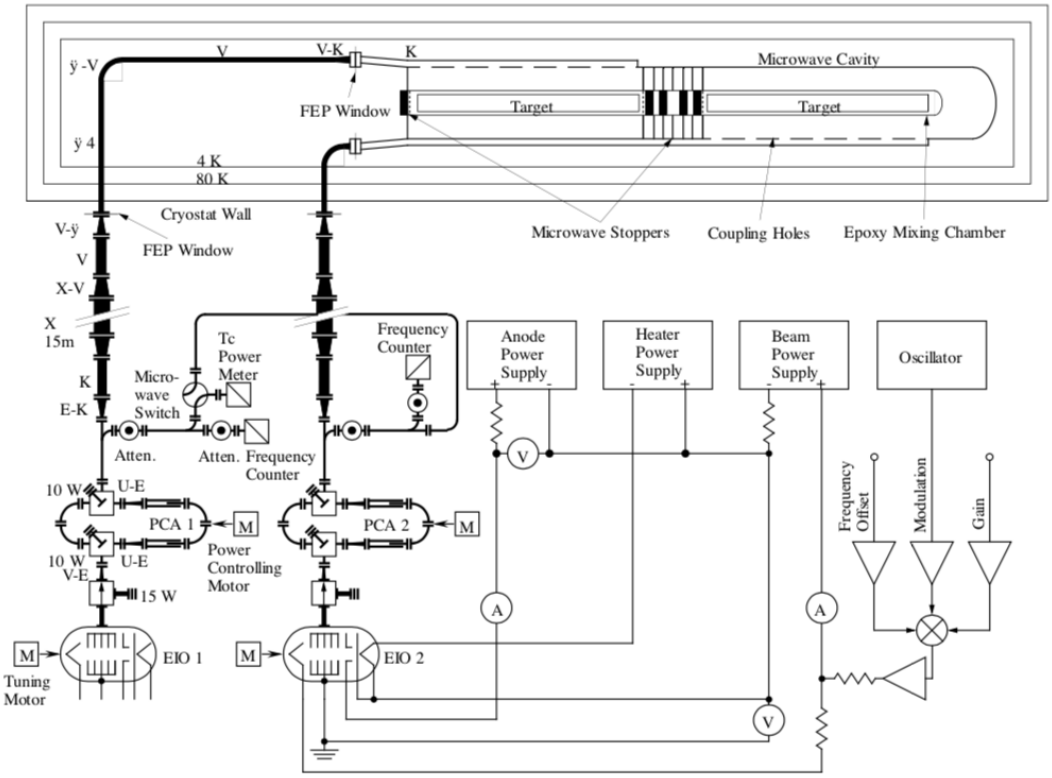

Figure 3.9: The microwave setup. The trombone attenuators are visible. The figure is actually the SMC experiment setup [65] but is still mostly valid for COMPASS.

The sources used are extended interaction oscillator (EIO) tubes with an output power of about 20 W in frequency range of about 2 GHz around the central frequency of 70 GHz. The frequency can be tuned either by changing the cathode voltage or by changing the cavity size of the EIO. The EIO tubes are protected from reflected microwaves by circulators and matching loads of 15 W.

The commercially available attenuators can withstand rather low power of several watts. It was necessary to use in-house solution for the microwave system. The power of each EIO tube is split into two branches. One is fixed with a junction to matching load and second one is a trombone-like design, which is adjustable by micro-metric screw. The two branches are then connected together. Clear illustration of the attenuator is shown in Fig. 3.9. The trombone works as phase shifter. The attenuation is then based on interference of the waves from the two branches. The frequency is measured independently for each EIO tube. The microwave power is measured by a thermocouple. All of the measurement are transmitted to the COMPASS DCS system.

The microwaves are transmitted to the microwave cavity by long wave guides. Total attenuation before the target cells was measured to be about 6 dB. The microwave cavity is a copper cylinder with 40 cm diameter and about 1.3 m length. The cavity can be internally divided either into two or three section using thin copper plates as microwave stoppers. For the three cell setup the power from one of the wave guides is first split into two. The upstream and downstream cells then share the same EIO tube are polarised in the same configuration while the central cell is polarised in the opposite configuration. For two cell setup both are independent and have opposite polarisation.

3.7 NMR system

The scheme of the NMR system is shown in Fig. 3.10. It consists of 10 NMR coils mounted on the target holder. Each coil is connected to the Liverpool Q-meter [66], which is used as phase sensitive detector for measuring the complex voltage in the resonant circuit. The output from the Q-meter is connected to the Yale card, which serve as amplifier (possible settings are either 1 or 207) and also allows for DC subtraction. Finally, the signal is digitized and stored in a PC. The control system and data acquisition is based National Instruments [67] hardware and LabView software. The configuration of the NMR coils with respect to target cells used in various years:

- 2010/2011 3 coils upstream, 4 coils middle, 3 coils downstream, all outside the cells
- 2015 5 coils both upstream and downstream, 2 coils inside and 3 outside
- 2018 the same configuration as in 2015 but 3 coils inside and 2 outside.

3.8 Target material and radiation hardness

The choice of the target material is in principle determined by the nucleus species needed for the experiment (i.e. proton or deuteron) and by the so-called figure of merit defined by the following formula:

$$FoM = f^2 P^2 F p \rho \tag{3.8}$$

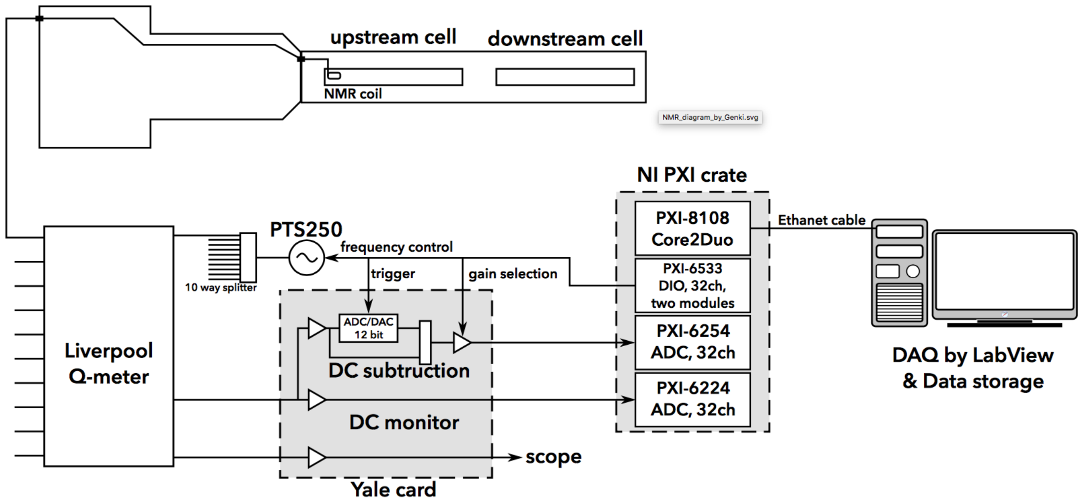

Figure 3.10: Scheme of NMR system used in 2015 and 2018.

where P is the maximum polarisation, f is the dilution factor, Fp is the packing factor, and ρ is the density of the material. The dilution factor f is defined as fraction of polarisable nuclei in the material. Naively $f = 3/17 \approx 0.176$ for ammonia. In reality the different cross-sections for the proton and other nuclei needs to be considered. The dilution factor can be then written as

$$f = \frac{n_p \sigma_p}{n_p \sigma_p + \sum n_A \sigma_A}, \tag{3.9}$$

where n_p and n_A are the amount of protons and non-polarisable nuclei respectively, and σ_p and σ_A are the corresponding cross-sections. Note that not only the target material but also the helium mixture and other material inside the mixing chamber need to be taken into account. The dilution factor than has kinematical dependence and varies between SIDIS and Drell-Yan processes.

In addition, one needs to consider also radiation hardness of the material (especially in the case of Drell-Yan experiments where the radiation dose is expected to be high) and in some cases also the feasibility of using the material at all. This is mainly given by the complexity of the preparation of the material or other properties such as the width of the EPR line. Very narrow line (such as in trytil doped D-butanol) can make it very difficult to be polarised at COMPASS [68] as very high homogeneity of the magnetic field (better than 10^{-5} T) is required in full target volume.

The ammonia used as a proton target at COMPASS has been always considered very radiation hard as described e.g. in Ref. [69]. In 2018 it was very clearly observed that even that is not enough for the Drell-Yan experiment [3] and several signs of radiation damage were observed. These include lower maximum polarisation reached and shorter relaxation time. Also they are observed to be polarisation sign dependent. Let us give an example: In the beginning of 2018 run maximum polarisation reached was about 80% positive and -85% negative, and at the end of the run they decreased to 75% positive and -68% negative. During the course of the year the average relaxation time in dipole field decreased

[3] This is also expected at the planned E1038 experiment in Fermilab, where they plan to exchange the material every couple of weeks.

from about 2500 h to about 1000 h. The above described symptoms can be explained by creation of new radicals in the material by the irradiation, which provides additional relaxation channels reducing both the maximum polarisation and relaxation time. The radiation damage can be removed by so-called annealing procedure when the material is warmed up to 80-100 K. This is rather risky procedure in the case of the COMPASS setup and was not performed during the run.

3.9 Target material weight measurement

Measurement of the weight of the solid ammonia poses quite a challenge by itself as the material temperature needs to be kept below 100 K all time. The method used at COMPASS and described in Ref. [70] is briefly summarised below.

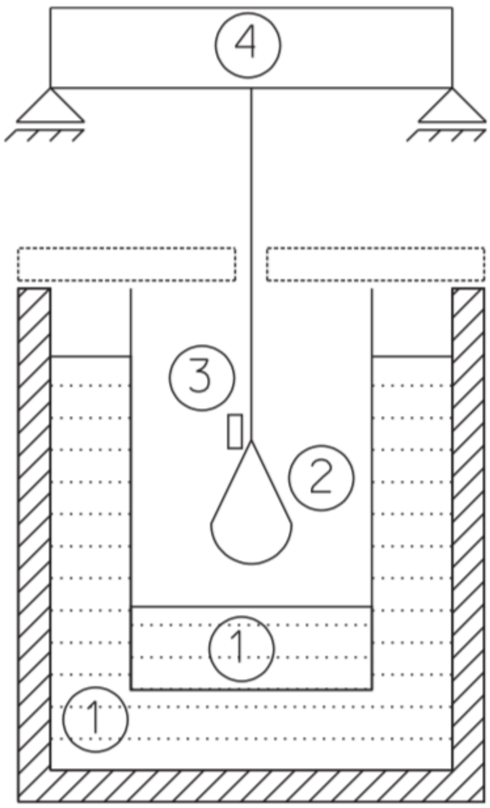

Figure 3.11: The weighting setup: 1. liquid nitrogen, 2. sock with material, 3. PT100, 4. scale.

During storage the material is kept inside nylon socks suspended on thin copper wire in standard LN_2 storage dewar. Four socks are used for the full batch of material used in 2015 and 2018. For the purpose of the weighting each sock is moved quickly into double dewar depicted in Fig. 3.11. The movement of the sock from the storage and back constitutes the most risky part of the the procedure as no temperature reading is available and has to be done very quickly in order to minimise the risk of destroying the radicals (T>120 K). The outer volume of the dewar is regularly refilled with LN_2 and the temperature of the socks is monitored by standard PT100 thermometer attached to the sock. The sock suspension wire is attached to laboratory scale. In about 8-12 h, depending on the amount of the material, the LN_2 drops out of the sock completely and the weight reading stabilises at a final value. Finally, the weight of the sock, suspension wire, sock's label, etc., is subtracted from the gross value and final weight is obtained.

	2015	2018
Up	333.5 g	329 g
Down	282.8 g	310 g

Table 3.1: Results of the weight measurements in 2015 and 2018. Estimated uncertainty for each value is about 1 g.

	2015	2018
Up	0.566	0.558
Down	0.480	0.526

Table 3.2: Packing factor results in 2015 and 2018.

The weight results from 2015 and 2018 are summarised in Tab. 3.1. Finally, from the known value of the target cell volume and density of ammonia the packing factor can be determined. The results are summarised in Tab. 3.2.

3.10 Relaxation time measurements in 2018

During the 2018 run several important and/or interesting measurements concerning the relaxation time of the polarisation were done in addition to the usual relaxation time measurement done for every physics data-taking period. We will briefly discuss two of them in the following sections - namely relaxation in zero magnetic field and relaxation during field rotation.

3.10.1 Relaxation time in zero magnetic field

There was an opportunity to perform relaxation measurement in zero magnetic field during the 2018 run. The principle was simply lowering of the solenoid field to zero, waiting several minutes, ramping up the field again, and measuring the polarisation value. This was repeated several times until the polarisation reached almost zero value. The process is illustrated in Fig. 3.12, which is taken directly from COMPASS DCS system. The measured values were then fitted by a single exponential, yielding the results of about 11 minutes for the positive polarisation and about 7.5 minutes for the negative polarisation. The fit is shown in Fig. 3.13. It is interesting to compare the values to the nominal relaxation time in the transverse configuration, which is at the order of 1000 h.

It should be noted that we are not aware of this measurement for ammonia target being ever done before.

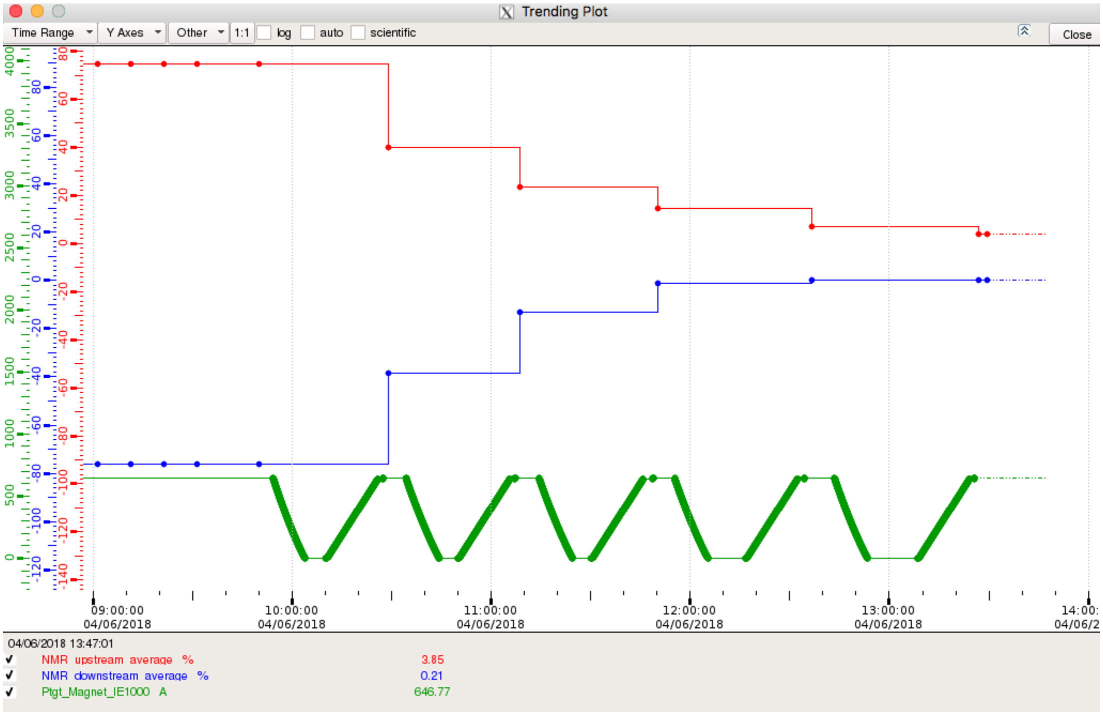

Figure 3.12: Zero field relaxation measurement, the magnetic field variation during the measurement is shown in green.

3.10.2 Polarisation loss during the magnetic field rotation

Between 2015 and 2018 the magnetic field configuration was changed for the field rotation. Originally the trim coils were set to zero current for the field rotation. In the configuration they are ramped to the same current as nominally, but with opposite sign to make the field even more inhomogeneous for the field rotation. This was done because in 2015 there was still non-negligible loss of polarisation of about 0.5% observed during the field rotation caused possibly by super-radiance.

The test was done simply by rotating the field consecutively five times and measuring the polarisation after each rotation. The observed loss was at the level of 0.1% or less. This proved that the change in configuration was indeed successful in suppressing the polarisation loss.

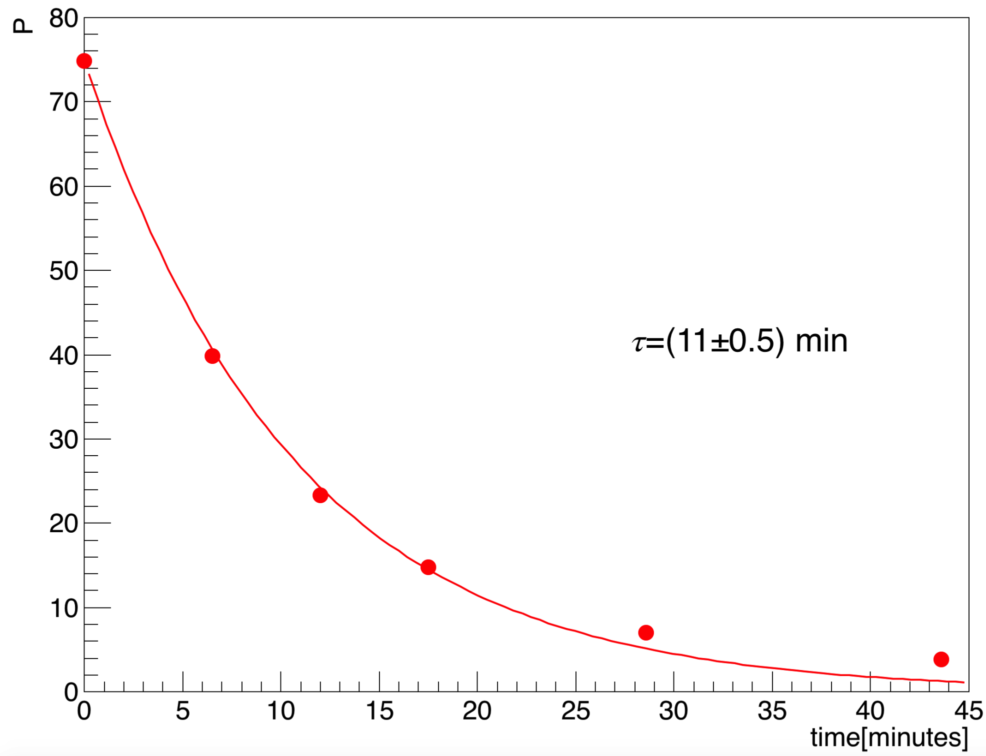

(a) Upstream cell with positive polarisation.

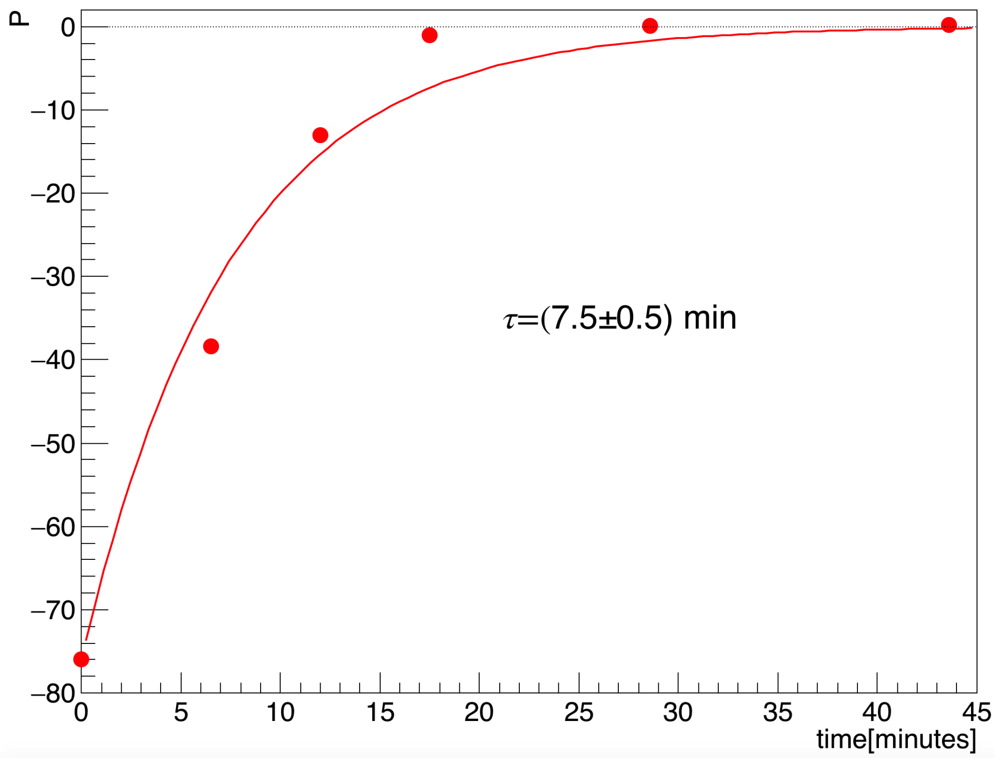

(b) Downstream cell with negative polarisation.

Figure 3.13: Zero field relaxation measurement results.

4. Express Analysis during 2015 DY run

4.1 Introduction

The express analysis is a quasi-online analysis of the physics data during the running period in order to assess the quality of the data depending on the apparatus and beam condition and to provide quick feedback to the data-taking. This is done by reconstructing selected run of data and checking various indicators with respect to expectations. The run can be either considered as a good one, and thus confirming the expectations, or a problematic one, where an impact of various hardware problems can manifest in the data. In addition, beam properties can be checked if a beam tuning was done at some point during the data-taking.

The indicators of the data quality used in 2015 data-taking were the number of reconstructed J/ψ's and high-mass Drell-Yan events per run of 200 spills, the width of J/ψ peak (provided that a reasonable alignment was available), distribution of primary vertices in the target, kinematic variables x_{proton} and x_{pion} coverage for masses above 2.5 GeV/c^2, beam properties like beam angle, or any other distributions if requested by experts.

4.1.1 Data processing

The raw data were reconstructed using the up-to-date version of CORAL software and a latest alignment file available. Following cuts were then used at the PHAST level:

- The best primary vertex exists
- Vertex in target
- At least 2 outgoing tracks with an opposite charge
- Muon identification, i.e. a track crossed more than 15 radiation lengths
- Time difference between the tracks less than 5 ns
- Di-muon trigger fired
- Momentum of negative tracks less than 100 GeV/c to eliminate muons from the beam decay

4.2 Examples

In this section we show several examples of observations made during the summer of 2015.

4.2.1 Good run

First thing to show is what is generally considered as a good run. That means the beam had a proper intensity of about 4×10^8/s during the full run, there were no major problems with detectors, and DAQ was running stably. The results concerning the reconstructed di-muon mass spectrum, and the x_{proton} and x_{pion} coverage for di-muons with mass above 2.5 GeV/c^2 for the run 260695 are shown in Fig. 4.1.

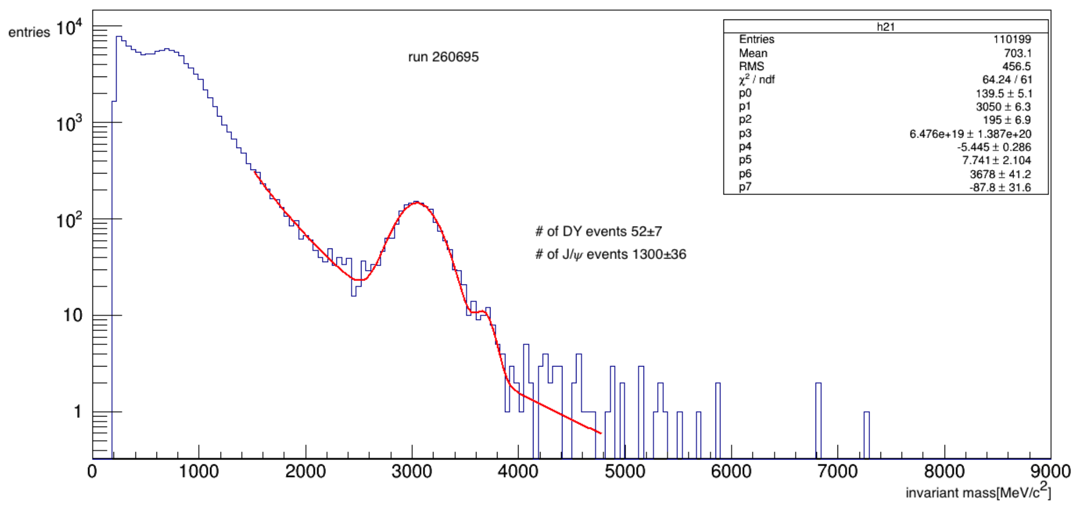

(a) Invariant mass distribution of di-muon pairs.

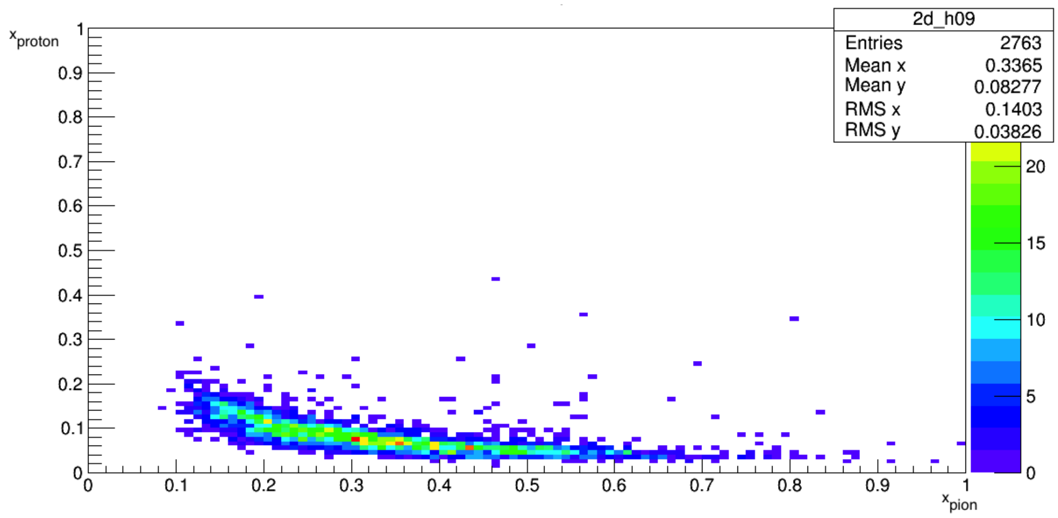

(b) x_{pion} versus x_{proton} of di-muons with mass above 2.5 GeV/c^2.

Figure 4.1: Good run.

It is worth mentioning that the fitted masses of J/ψ and ψ(2S) of around 3.05 GeV/c^2 and around 3.678 GeV/c^2, respectively, are close to the PDG [39] values already at this stage of analysis.

4.2.2 Pixel MicroMegas issue

Let us now discuss the case of the run 260964. This particular run had none of the three pixel MicroMegas stations working due to front-end problems. Having such an issue the run would never be considered for physics. Nevertheless, it was interesting to check what was the effect if this situation on the reconstruction of the data.

In Fig. 4.2 we can see the momentum distributions for a good run in comparison with the bad run. The effect is pretty obvious in high momentum of negatively charged tracks and for low momenta of both polarities. The kinematic coverage in x_{pion} versus x_{proton} is also affected compared to good run Fig. 4.1, especially in region of high x_{pion}. On an amusing note - the absence of the pixel MicroMegas lead to a significant speed up of the reconstruction by about a factor of 2 to 3.

4.2.3 Dead time setting test

One last case we will discuss is that of the run 260066. This was not a physics run. It was a run with low dead time setting, taken during tests to find the optimal settings of the dead time. It was observed that too low setting of the dead time leads to noise generated at the digital level by the front-ends, which basically renders all the MWPCs useless. This provided an opportunity to see how they contribute to the reconstruction and if it might even be beneficial to exclude them altogether for gain in the dead time.

The relevant plots are shown in Fig. 4.3. It is fairly obvious that excluding the MWPCs is not a way to proceed. The track reconstruction is affected in a similar way as in the case of absent pixel MicroMegas. In addition, the J/ψ peak is less prominent with a much worse resolution of about 350 MeV/c^2 down from optimal 200 MeV/c^2. As a bit of surprise come the fact that the number of reconstructed high-mass Drell-Yan events remains unaffected. This suggests that at least for reconstruction in the Large Angle Spectrometer the MWPCs are indeed not a major contributor.

4.3 Conclusions and lessons learned

The above mentioned issues were selected as rather striking examples of potential problems, which could be encountered also in the future data-taking. This assumption confirmed already in the second year of Drell-Yan measurements in 2018, where the experience gained in 2015 was put in use. However, it needs to be stressed that the express analysis cannot cover all possible problems. This mainly applies for true stability studies and angular distributions needed for the asymmetries measurements. We will discuss these topics in the physics analysis section.

Just for completeness we summarise below some of the conclusions based not only on the cases presented here:

- One coordinate plane of any detector not working does not present major problem

- Pixel MicroMegas are detector of vital importance for the data-taking
- Beam instabilities can cause severe problems
- Running without MWPC is not feasible, thus running with higher dead time is mandatory.
- The beam telescope has low redundancy, one tracking plane off already severally degrades the reconstruction.

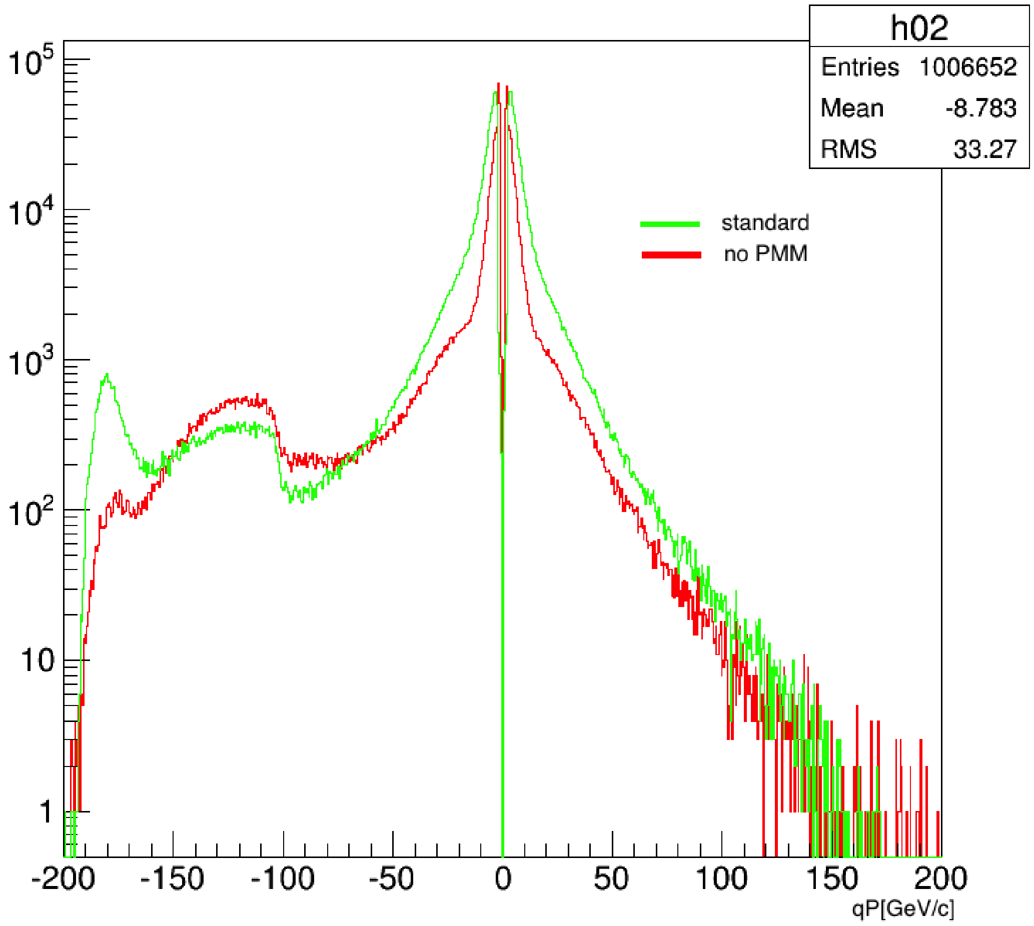

(a) Momentum distribution of tracks with and without pixel MicroMegas. The sign corresponds to the charge of the track.

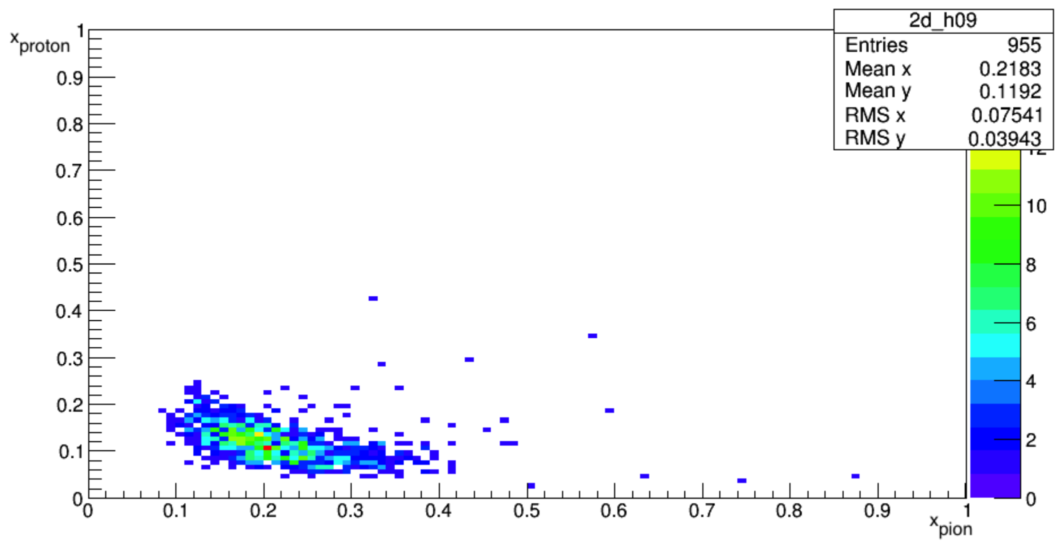

(b) x_{pion} versus x_{proton} of di-muons with mass above 2.5 GeV/c^2.

Figure 4.2: Pixel MicroMegas off.

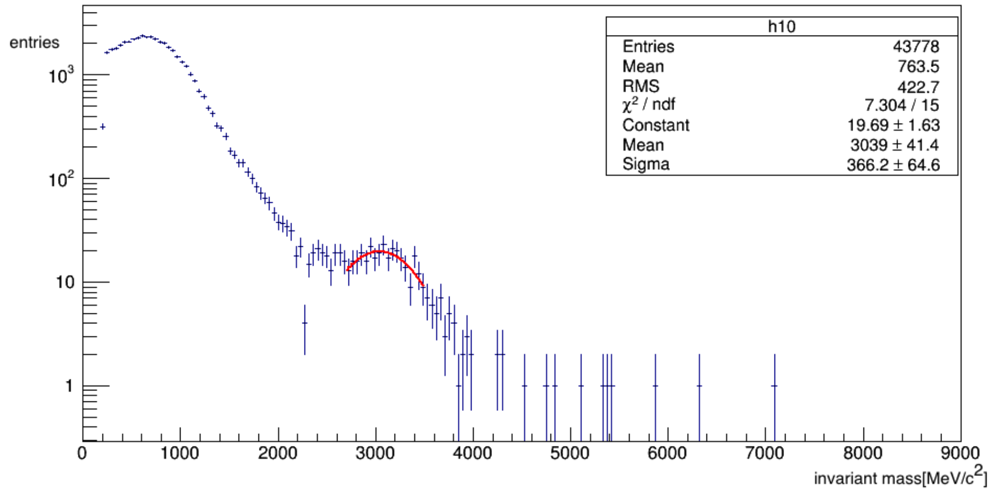

(a) Invariant mass distribution.

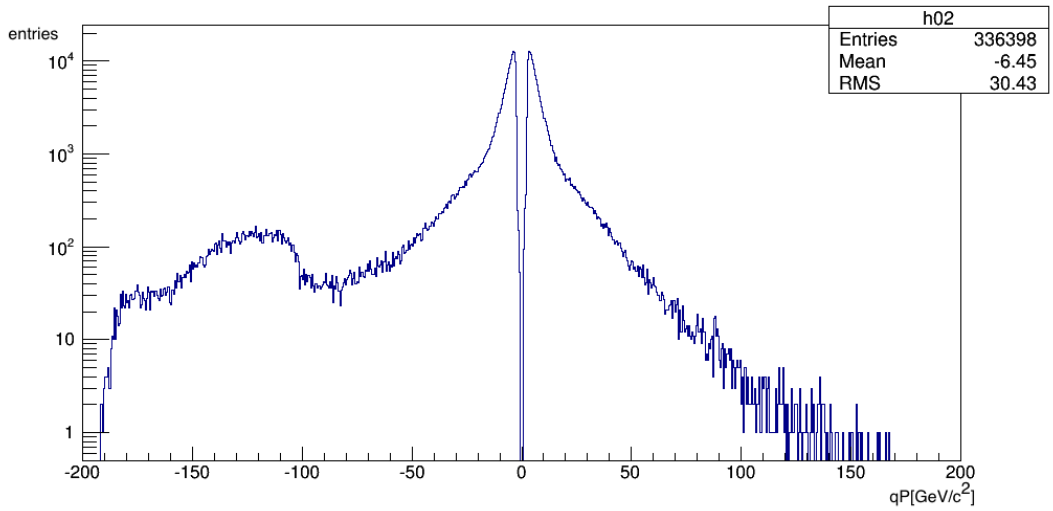

(b) Momentum distribution of tracks. The sign corresponds to the charge of the track.

Figure 4.3: MWPCs practically off due to significant noise on front-end electronics.

5. Detector efficiency studies in 2015 data

5.1 General principles

A perfect description of the experimental apparatus is necessary input into the Monte Carlo simulation. It allows to obtain precise values of the experimental acceptances. Their knowledge is then utilized for precise measurements, e.g. the Drell-Yan absolute cross-section or unpolarised asymmetries. The detector efficiency is a part of a description of every detector. It characterises how much a real detector deviates from an ideal case. The principle of the measurement of the detector efficiencies is to exclude the detector plane of interest from tracking and to look whether there is a corresponding hit in the detector in a proximity of the extrapolated reconstructed track. It can be expressed mathematically in the following way:

$$Efficiency = \frac{\#hits\ found}{\#hits\ expected}, \tag{5.1}$$

where $\#hits\ expected$ is basically a number of tracks which were extrapolated to the detector plane passing through a given spatial bin, and $\#hits\ found$ is a number of hits which are found in the vicinity of the extrapolated track in a given spatial bin. The usual choice for the vicinity is $\pm 3\sigma$, where σ is the detector resolution.

In the following we give several examples of detector efficiencies evaluated for 2015 data-taking and we show that can be also useful for revealing some hardware issues, which would be otherwise very difficult to see.

5.2 Beam telescope

It is important to have well operating beam telescope in order to have a proper beam-dimuon association in the vertex. The beam telescope configuration in 2015 had a low redundancy. It was also the first time when these detectors were used with a high intensity hadron beam. For this reason it was important to verify that the detectors are performing well and see if some improvements might be needed for 2018 run. The efficiencies were evaluated for one particular run, which was considered good. The results are shown in Fig. 5.2. One expected feature, which has been observed, were several inefficient fibres across all the SciFi stations. In addition there were significant cut-outs observed in all the planes, otherwise rather efficient. These can be split into two groups - the first is the upper left corner (when facing the setup from upstream side) and second is the strange diamond-shape of the two U-coordinate planes.

The U-plane diamond shape can be simply explained by not enough redundancy in the U coordinate, when by removing the plane in interest there is only one left for track reconstruction in the non-overlapping area. The problem of the missing part on the other planes is more complex. The almost obvious idea is that there is a physical overlap between the SciFi station and part of the Veto system,

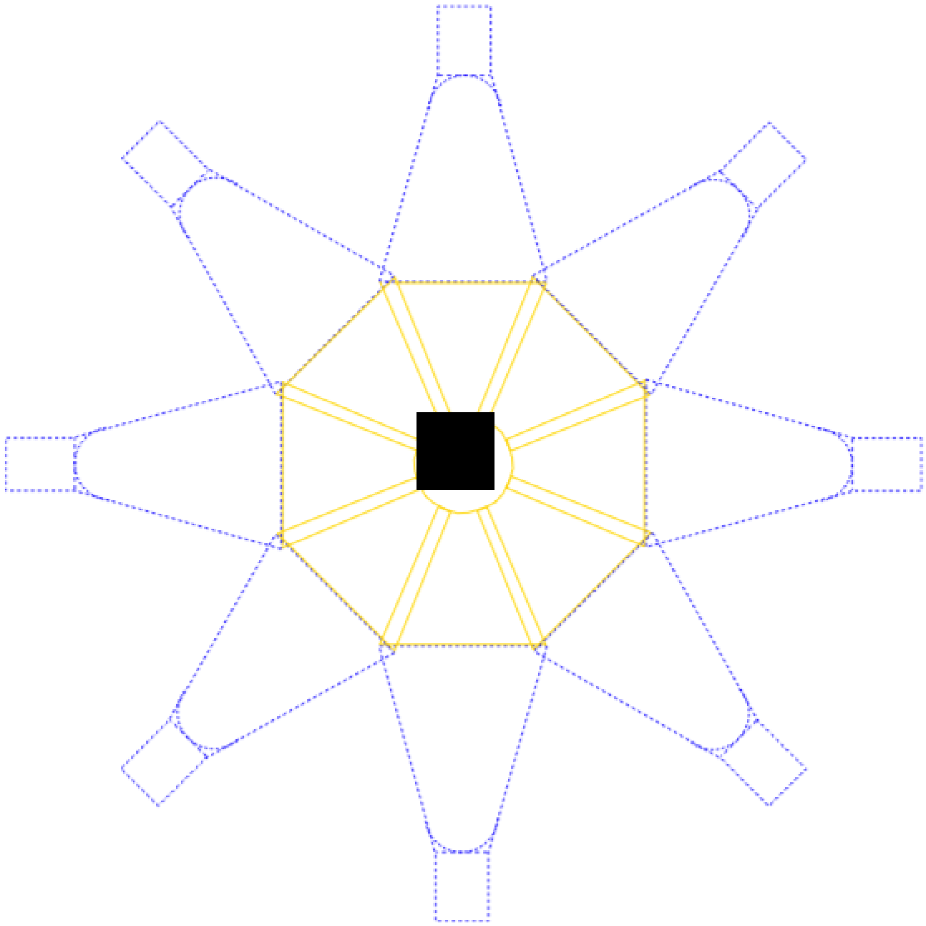

Figure 5.1: Sketch of Veto Inner 2 [71] and possible overlap with SciFi detectors.

namely Veto Inner 2. The idea for that is shown in Fig. 5.1. The final solution was discovered only much later, when the detector in question was disassembled for maintenance and it was found that two of the detector planes slipped from the originally assumed position. This illustrates the importance of staying in touch with the hardware otherwise one might be lead to false conclusions, which would have affected not only the detector description put into the MC simulations, but also at least another year of data-taking.

5.3 Vertex detector

The another detector on the list to be investigated as soon as possible was the newly employed Vertex detector, described in Chapter 2. The efficiencies were evaluated by the same method as described previously. The results are presented in Fig. 5.4. Overall efficiency is rather high, above 90%. In reality however this turned out to be meaningless information. It was found out [72] that the detector has very limited use in track reconstruction due to very high hadronic pile-up, which is impossible to distinguish from the dimuon events. It was then decided not to use the detector again in 2018 data-taking. Currently, there is an

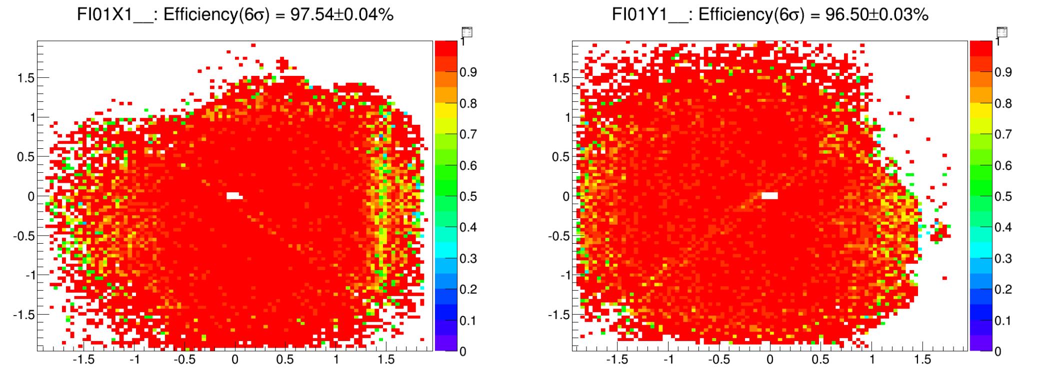

Figure 5.2: Efficiencies of SciFi01. Detector coordinate is always along the Y-axis.

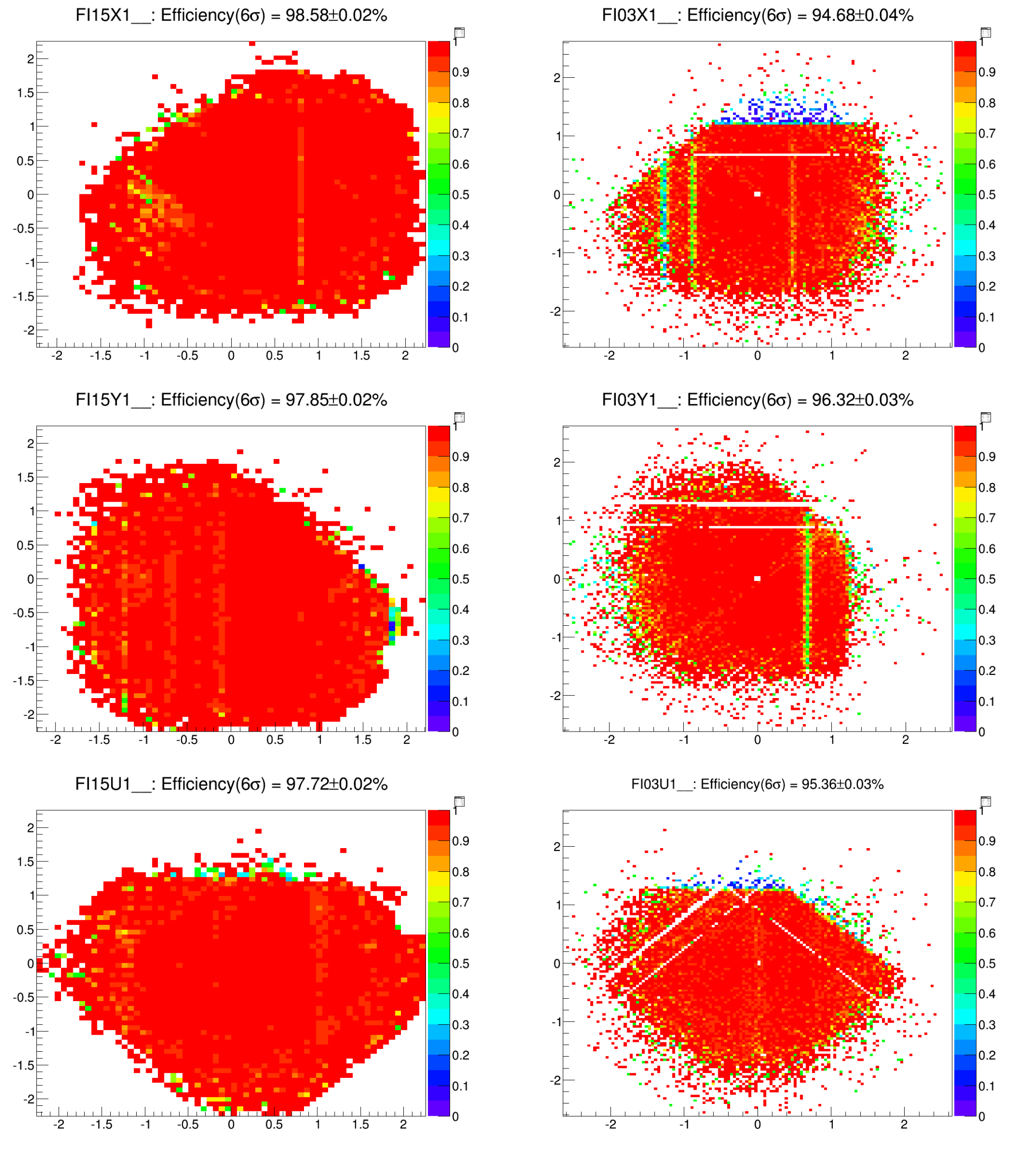

(a) SciFi15 (b) SciFi03

Figure 5.3: Efficiencies of SciFi15 and SciFi03. Detector coordinate is always along the Y-axis.

ongoing discussion on how to cope with the severe pile-up for the future Drell-Yan programme with the proposed AMBER experiment[24].

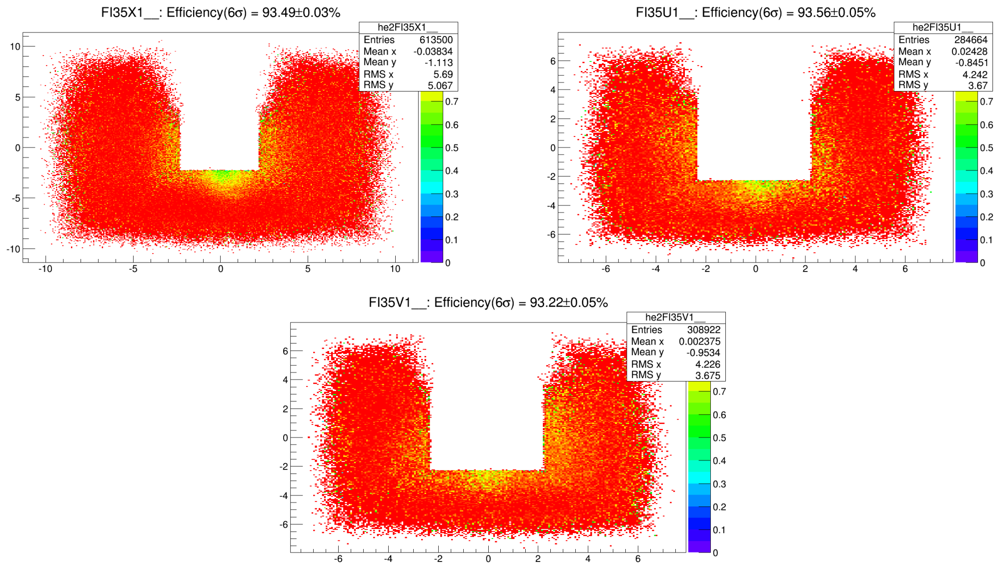

Figure 5.4: Vertex detector efficiencies. Plane coordinate is always along the Y-axis.

5.4 GEM detectors

GEM detectors are not contributing very much to the reconstruction of the dimuon events with mass above 3 GeV/c^2 due to their limited coverage. Still it is interesting to see how well they operate in Drell-Yan environment, where they cover mostly the high rate of beam decay muons[1].

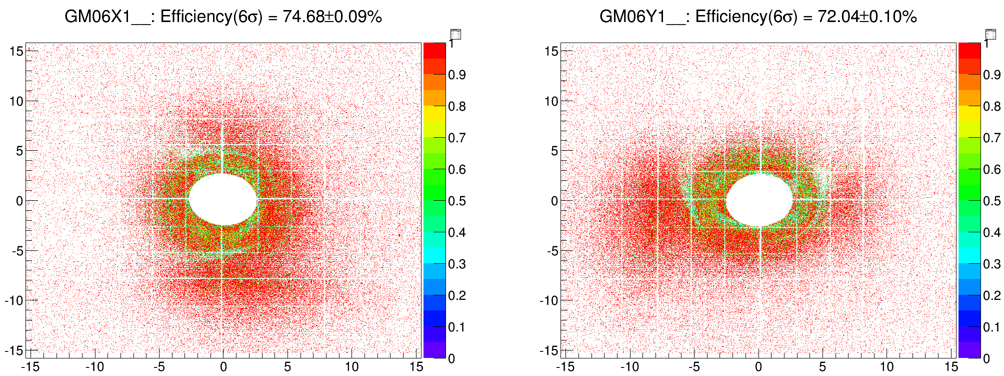

Figure 5.5: Efficiencies of GEM06. Detector coordinate is always along the Y-axis.

One particular example is shown in Fig. 5.5. It can be seen that the efficiency is somewhat lower in the central region. This could be caused by a higher flux

[1]Beam decay muons constitute about 1% of the nominal intensity, i.e. about 10^6 particles per second.

in the central part, which is generated by secondary interaction in the RICH detector beam pipe located upstream of the detector. The second possibility could be an ageing of the detector itself as this effect was less pronounced in previous years [73].

5.5 Conclusion

As could be seen from previous examples the detector efficiencies are not only important for good MC description but they also provide valuable tool to spot potential hardware issues in the apparatus which would otherwise not be observed and fixed.

6. General analysis principles

In this chapter we will discuss the common issues for the analysis being presented in Chapter 7 and 8. That is mainly the data stability checks, the asymmetry extraction method and general remarks concerning the systematic uncertainties.

6.1 Data stability

In order to allow for reliable extraction of the physics asymmetries the data are checked for a long term stability. The checks are done for each period separately as the extraction of the asymmetries is done by combining two sub-periods with the opposite polarisation.

The checks proceed in two steps. First step is the bad spills rejection and second step is the the bad runs rejection[1].

6.1.1 Bad spill analysis

At the bad spill analysis several combined measured variables are monitored. The variables used in 2015 selection are summarised in the following list:

- Number of beam particles divided by a number of events
- Number of beam particles divided by a number of primary vertices
- Number of hits of beam particles divided by a number of beam particles
- Number of primary vertices divided by a number of events
- Number of outgoing tracks divided by a number of events
- Number of outgoing particles divided by a number of events
- Number of outgoing particles from a primary vertex divided by number of primary vertices
- Number of outgoing particles from a primary vertex divided by number of events
- Number of hits of outgoing particles divided by a number of outgoing particles
- Number of μ^+ divided by a number of events
- Number of μ^+ from a primary vertex divided by number of events
- Number of μ^- divided by a number of events
- Number of μ^- from a primary vertex divided by a number of events

[1]Note that there are somewhat different variables scrutinised in 2010 and 2015 data, since the processes measured are quite different. We will comment on these in the text.

- Sum of χ^2 of outgoing particles divided by a number of outgoing particles
- Sum of χ^2 of all vertices divided by a number of all vertices.
- Trigger rates (MT-LAST, OT-LAST, LAST-LAST dimuon triggers)

To identify the bad spills, the value of every variable is compared to the values in the neighbouring spills. The spill is considered good if the value of the variable of the given spill falls in given interval for given number of neighbours. Both the interval width and the number of neighbours varies between different variables and periods. The details can be found in Ref. [74]. We show an example of three different variables for three different periods in Fig. 6.1.

The list of variables used for 2010 is different from the 2015. The monitored variables concern the scattered muon instead of the dimuon. In addition, a number of clusters in calorimeters and their energy is monitored.

The rejection rate for each period of 2015 data is shown in Tab. 6.1. In case of 2010 the rejection rate was somewhat lower at the level of 3-8% [75].

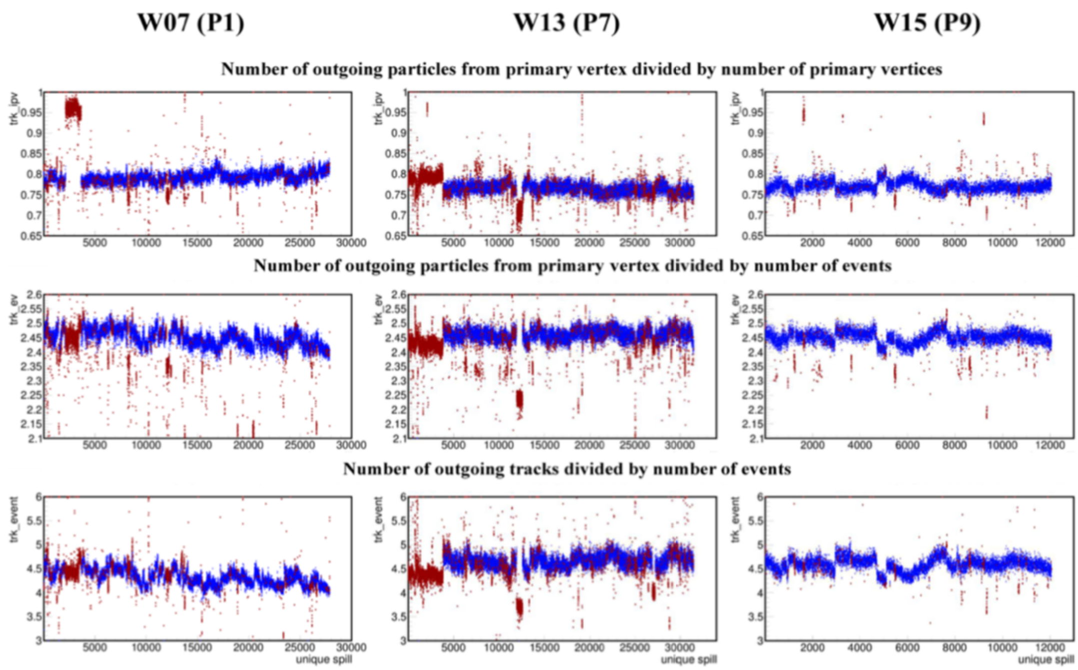

Figure 6.1: Example of the bad spill selection for three periods of 2015 data.

6.1.2 Bad run analysis

In the bad run analysis the shapes and means of distributions are monitored. The relevent distributions are the kinematic variables (x_N, x_π, q_T, $M\mu\mu$, muon and beam momenta, and positions of the interaction vertices) and angular variables (muon laboratory angles, physics angles). The shapes are compared for every pair of runs using unbinned Kolmogorov-Smirnov test [76]. The distribution means are compared with overall means of the periods. Values that are biased by more than 5 standard deviations are rejected. An example for the virtual photon momentum (the dimuon momentum) is shown in Fig. 6.2. The

Period	Bad spills	Bad spills and runs
W07(P01)	11.8%	17.9%
W08(P02)	18.0%	21.2%
W09(P03)	14.8%	17.1%
W10(P04)	15.9%	17.8%
W11(P05)	22.5%	26.1%
W12(P06)	12.7%	13.8%
W13(P07)	22.3%	22.7%
W14(P08)	8.9%	10.7%
W15(P09)	3.9%	3.9%

Table 6.1: Bad spills and run rejection for 2015 data [74].

impact of the bad run rejection is rather small compared to the bad spill one, as can be seen in the Tab. 6.1.

For the 2010 somewhat different approach was used [75]. In addition, some other variables were monitored, mainly the reconstructed K^0 mass.

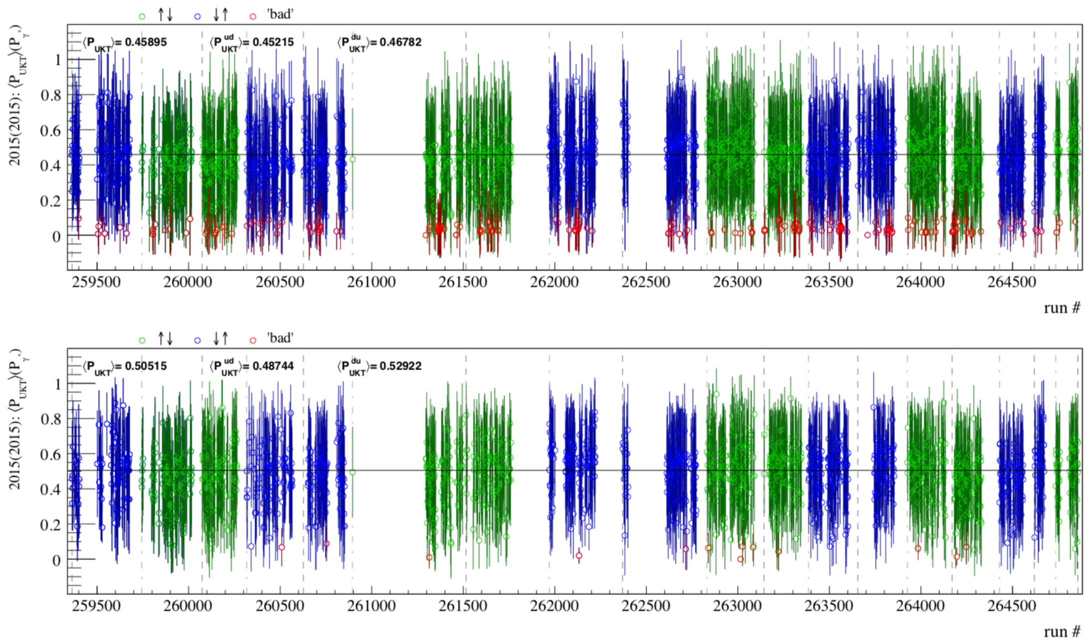

Figure 6.2: Example of bad run selection, on top - before the spill rejection, in the bottom - after the bad spills rejection.

6.2 Event selection

The event selection uses several cuts to filter out as clean signal of interest as possible. We will describe the specific criteria separately for each of the analyses. Since we are dealing with J/ψ peak the resulting dimuon invariant mass distributions are fitted with Gaussian. The peak is then cut at $\pm 2\sigma$ for the SIDIS analysis or $\pm 0.5\sigma$ for the Drell-Yan analysis. The cut for the Drell-Yan data is more strict due to the worse experimental resolutions. Note that the bad spill list and bad run lists are applied at the event selection level.

6.3 Raw asymmetry extraction

There are several possibilities to extract the spin asymmetries from the data. First option would be to correct the data for acceptance effects and simply fit the resulting angular distribution. This method is difficult to use as a perfect Monte-Carlo simulation is required.

Another option would be to use a method, which would be acceptance free. We will now describe one such method of extraction. It is the so-called 1D double-ratio method, which relies on having two target cells with opposite polarisation and frequent polarisation reversals during the data-taking, which allows for cancellation of the acceptance. We assume the cross-section in the following form:

$$\sigma(\Phi) = \sigma_0 + |S_T|\,\sigma_\Phi \sin\Phi, \tag{6.1}$$

where Φ denotes any of the possible angular dependencies. The number of events for polarisation $\uparrow$ produced in target cell C can be then written as:

$$N_C^{\uparrow}(\Phi) = F_C n_C \sigma_0 a_C^{\uparrow}(\Phi)(1 + A_{raw}\sin\Phi), \tag{6.2}$$

where F_C is the integrated beam flux, n_C is the number of target nucleons, and $a_C^{\uparrow}(\Phi)$ is the corresponding acceptance. For the polarisation $\downarrow$ the Φ is replaced by $\Phi + \pi$ and the number of events for polarisation $\downarrow$ produced in target cell C can be then written as:

$$N_C^{\downarrow}(\Phi) = F n_C \sigma_0 a_C^{\downarrow}(\Phi)(1 - A_{raw}\sin\Phi). \tag{6.3}$$

We can then define the double ratio for two target cells (U-upstream, D-downstream) with opposite polarisations[2]:

$$R(\Phi) = \frac{N_U^{\uparrow}(\Phi)N_D^{\uparrow}(\Phi)}{N_U^{\downarrow}(\Phi)N_D^{\downarrow}(\Phi)}. \tag{6.4}$$

Then assuming small asymmetry A_{raw} the ratio can be written down:

$$R(\Phi) \approx K\frac{a_U^{\uparrow}(\Phi)a_D^{\uparrow}(\Phi)}{a_U^{\downarrow}(\Phi)a_D^{\downarrow}(\Phi)}(1 + 4A_{raw}\sin\Phi). \tag{6.5}$$

We assume that the ratio of acceptances between upstream and downstream cell does not change between the two subperiods:

$$\frac{a_U^{\uparrow}(\Phi)a_D^{\uparrow}(\Phi)}{a_U^{\downarrow}(\Phi)a_D^{\downarrow}(\Phi)} = 1 \tag{6.6}$$

The uncertainty of the double ratio is expressed:

$$\sigma_R = \sqrt{\frac{1}{N_U^{\uparrow}} + \frac{1}{N_D^{\uparrow}} + \frac{1}{N_U^{\downarrow}} + \frac{1}{N_D^{\downarrow}}}, \tag{6.7}$$

where we take the expectation value of the $R = 1$ to minimise the possible bias in case of a low statistics.

The double ratio is evaluated in 8 (SIDIS) or 16 (Drell-Yan) bins and fitted by the functional dependence of $K(1 + 4A_{raw}\sin\Phi)$. The correction to the finite bin size is also applied.

[2] We remind here that each period has a polarisation reversal in the middle, between the two subperiods, hence it makes sense to construct such a ratio.

6.4 Determination of the physics asymmetries

The raw asymmetry A_{raw} is obtained for each period of data-taking and for each kinematic bin. The values are then corrected for the average polarisation P and the dilution factor f. In addition, the average value of a corresponding D-factor defined in Eq. 1.36 is taken into account if its value is different from one.

The values of the dilution factor f are provided within the COMPASS analysis software tool PHAST [55]. The dilution factor for the Drell-Yan measurement was evaluated using the parton-level Monte-Carlo program MCFM [77]. We will briefly discuss the issue of the dilution factor in corresponding analyses sections.

6.5 False asymmetries, pulls and systematics

There are systematic uncertainties related to the dilution factor f and polarisation P. The relative uncertainty of the polarisation measurement is $\pm 5\%$ and similar value corresponds to the dilution factor uncertainty.

Main systematic uncertainty stem from possible instrumental effects, which might mimic a real asymmetry. The stability of the apparatus acceptance is of particular interest since its assumption enters into the physics asymmetry evaluation.

There are several possible observables called false asymmetries, which can help to spot some potentially dangerous problems in the apparatus.

6.5.1 Pulls

First, the check of the statistical compatibility of the periods can be done by calculating the pulls:

$$P_i = \frac{A_i - \langle A \rangle}{\sqrt{\sigma_i^2 - \sigma_A^2}}, \tag{6.8}$$

where A_i is the asymmetry in every kinematic bin and for each period and $\langle A \rangle$ is the corresponding weighted mean. Assuming normally distributed data, the resulting distribution should be distributed as a Gaussian with the mean value at zero and the width equal one.

6.5.2 Time false asymmetries

The double ratio can be then evaluated using mixed data. We take every even-numbered runs and every odd-numbered runs within a given period and produce two new subperiods. In this way the polarisations average out and the resulting asymmetry should be equal to zero.

6.5.3 Target false asymmetries

Another possibility is to split the two target cells in half and combine the outer half and inner half into two new target cells. The resulting asymmetry should be again zero due to averaging out the polarisations.

7. Transverse spin asymmetries in J/ψ production in 2010 SIDIS data

7.1 Data selection

The starting point of this analysis are pre-filtered 2010 data[1] of the so-called new data production[2]. We look only at the $J/\psi \rightarrow \mu^+\mu^-$ decays. The number of possible J/ψ candidates should be larger than that used to be in the previous analyses [15].

The following selection criteria were applied on the pre-filtered data:

1. Best primary vertex[3] with 3 outgoing muon[4] tracks, i.e. 2 μ^+ and 1 μ^-[5]
2. Cut on the reduced χ^2 of the tracks, $\chi^2 < 10$
3. Bad spills and runs excluded
4. Cut on events triggered by the inclusive Middle Trigger, due to its unstable behaviour (only in the Period 5)
5. Cut on the vertex position, Z_{vertex}, $r_{vertex} < 2$ cm
6. Cut on the reconstructed beam track momentum (160 ± 10) GeV/c
7. Beam track extrapolation crosses the target cells to equilibrate the flux
8. Cut on the dimuon invariant mass; the invariant mass spectrum is fitted by the following function:

$$f(M_{\mu\mu}) = p0 \times \text{Gaus}(p1, p2) + p3 \times M_{\mu\mu}^{p4}, \tag{7.1}$$

   yielding the width of about 50 MeV/c^2 and the peak position of 3.11 GeV/c^2

9. Cut on the missing energy $|E_{miss}| < 3$ GeV/c^2 for the selection of exclusively produced J/ψ

We evaluate the final asymmetries for three different samples. The full sample, where no cut on E_{miss} is applied, an exclusive sample, where the cut of ± 3 GeV/c^2 on E_{miss} is applied, and a final "inclusive" sample, which is the complement to the exclusive one.

---

[1]Courtesy of Bakur Parsamyan.

[2]The muon reconstruction has been improved compared to the first production.

[3]As tagged by CORAL software, among several reconstructed vertices the one with most outgoing tracks is considered best.

[4]Track is considered as a muon track if it crossed more than 30 radiation lengths.

[5]Note that μ^+ beam is used for the DIS measurements.

The final statistics contains 17437 ± 132 events in the J/ψ peak, the exclusive sample contains 7031 ± 84 events, and the complementary "inclusive" sample contains 10406 ± 102 events. We show the corresponding invariant mass distribution in the Fig. 7.1 for the exclusive sample, and in Fig. 7.2 for the full and inclusive samples.

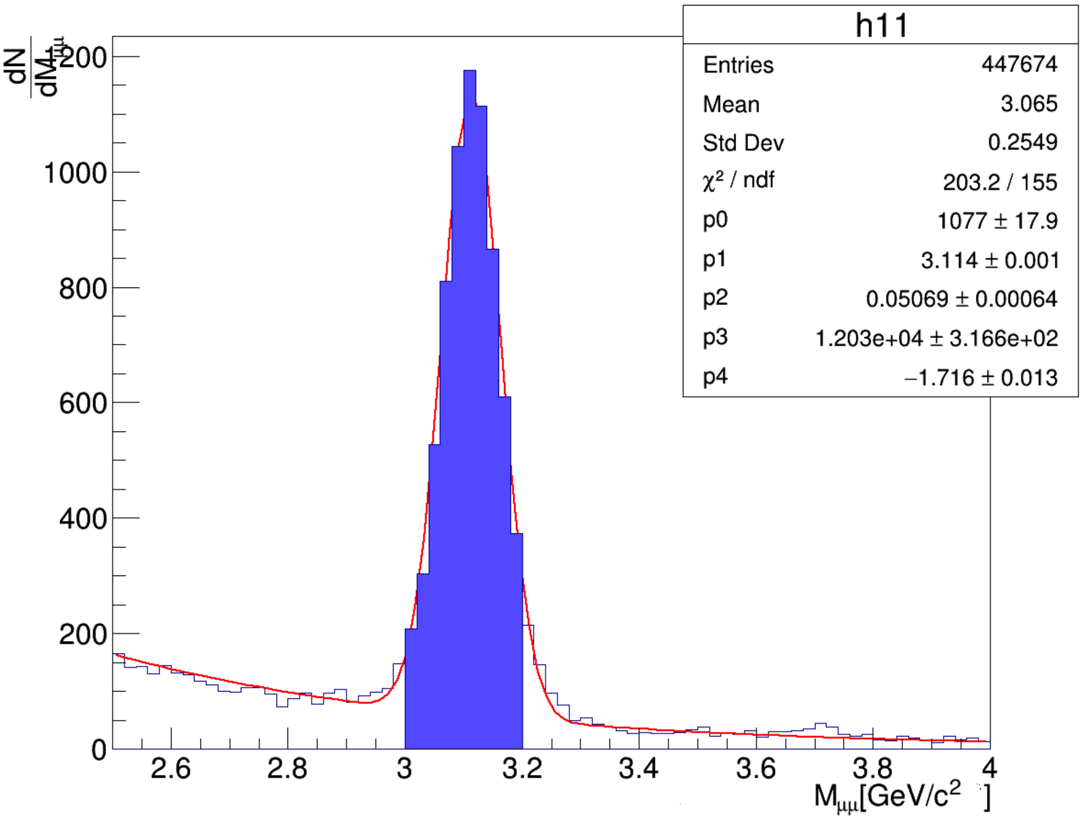

Figure 7.1: Invariant mass distribution of the exclusive sample. The shaded area highlights the mass cut.

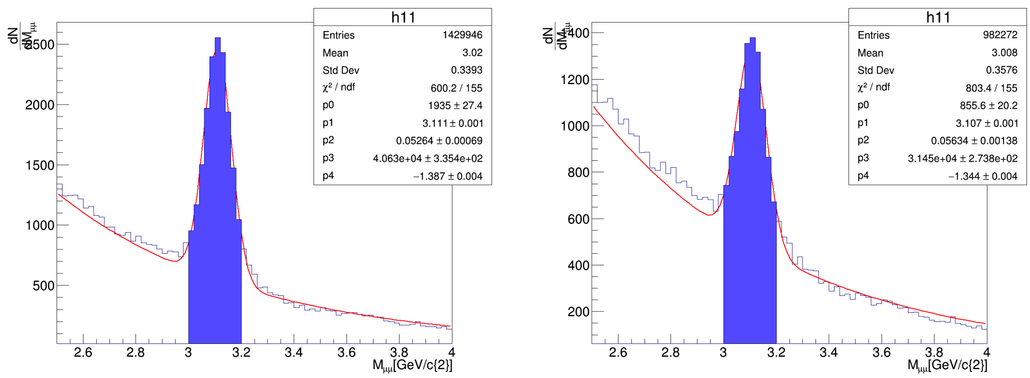

(a) full sample

(b) inclusive sample

Figure 7.2: Invariant mass distribution for the full and inclusive sample. Note that the fit function does not describe well the background.

The combinatorial background contribution differs significantly among the samples. The exclusive sample is the cleanest with S/B ratio $\sim$ 10, then it decreases to $\sim$ 2 for the full sample. Finally the "inclusive" has S/B $\sim$ 1. Note that the fit function does not describe well the inclusive sample background. This will lead to an underestimation of the background contribution, so the real S/B might be even worse for the inclusive sample.

7.2 Kinematic distribution

The Fig. 7.3 shows the Z-vertex distribution for all three data samples. We see no clear difference between the exclusive sample and the full or inclusive samples.

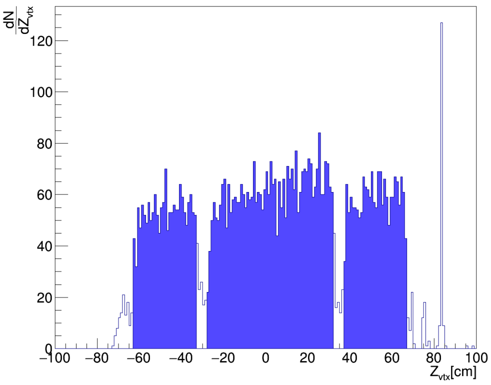

(a) exclusive sample

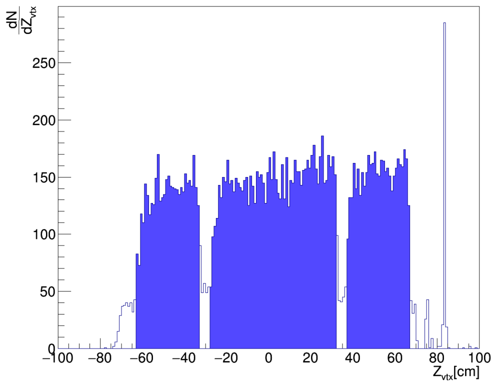

(b) full sample

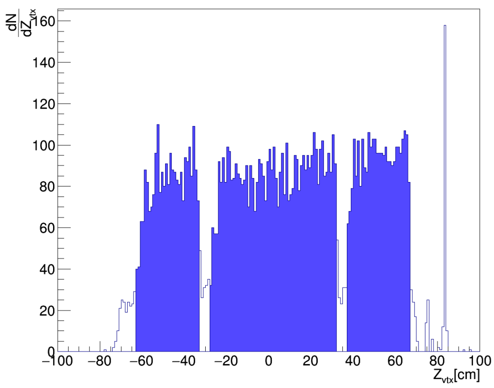

(c) inclusive sample

Figure 7.3: Z-vertex distributions for all three data samples. Clear target cells separation is visible. Shaded are shown the target cells cuts.

Fig. 7.4 shows the missing energy distribution for the full sample. Clear peak around zero is visible indicating the exclusive events.

The Fig. 7.5 and Fig. 7.6 show the $x_{bjorken}$ distributions, the J/ψ P_T distributions, J/ψs total momentum distributions and the y distributions. There is a clear difference between the exclusive sample and the full/inclusive ones. In order to verify the hypothesis that the peak in the $x_{bjorken}$ and y distributions stems from the background, we plot in Fig. 7.7 the corresponding distributions for

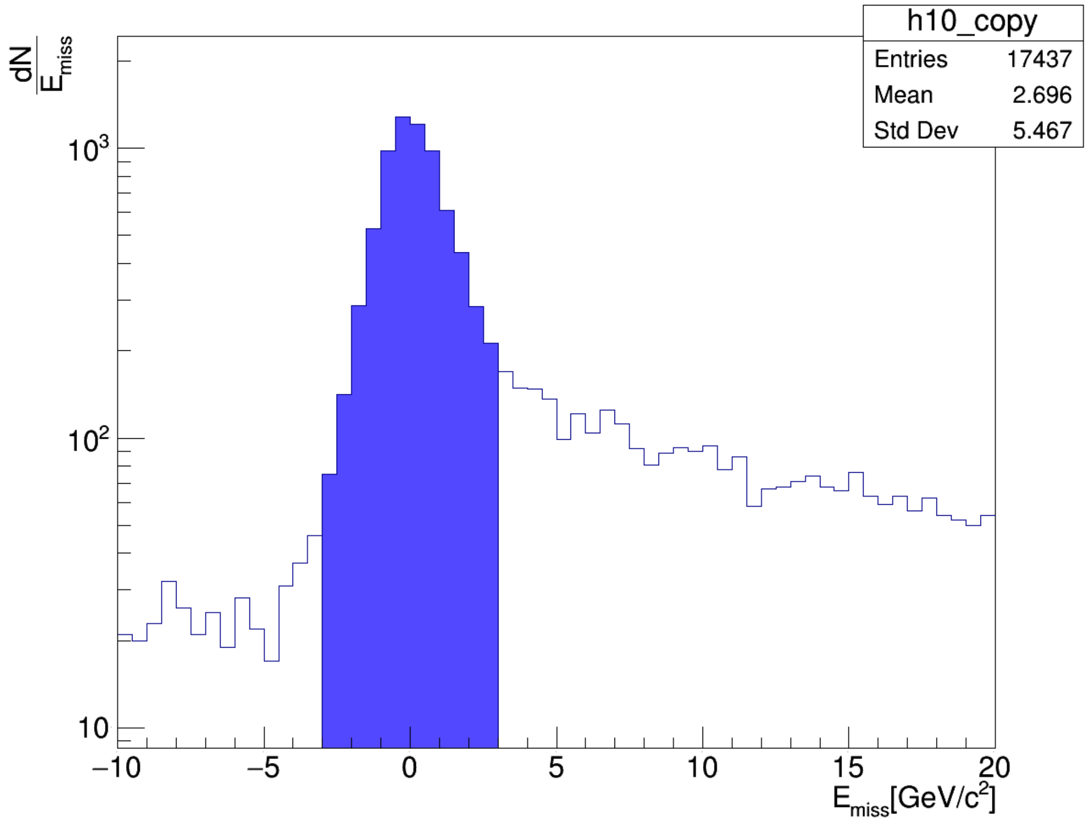

Figure 7.4: Missing energy distribution. The shaded are corresponds to the ± 3 GeV/c^2 cut.

300 MeV/c^2 wide side-bands around the J/ψ peak. They show the same peaking structures.

7.3 Results

All the 8 transverse spin asymmetries were evaluated for each of the three samples. The asymmetries were determined in a single kinematic bin due to the limited statistics. The raw asymmetries obtained by the double ratio method were corrected by the average polarisation for each period, the dilution factor, the corresponding D-factors (if any) and scaled by the S/B ratio.

The average polarisation varied between 0.77-0.83. The dilution factor was taken as an average of the available semi-inclusive values leading to value of 0.15. The scaling by the S/B ratio was done to compensate for the background contamination. The background is considered as having no spin effects. Alternatively the asymmetry in the neighbourhood of the J/ψ peak might be evaluated. However, this is less important in the exclusive case, where the background is low.

The Fig. 7.8 shows the results on all the 8 TSAs measured for each of the samples. We include the exclusive measurement results also separately in Fig. 7.9 for better visibility.

The Sivers asymmetry in exclusively produced J/ψ is measured to be

$-0.13 \pm 0.19_{stat}$, which is well compatible with the theoretical predictions in Ref. [28]. Unfortunately the prediction for our kinematics vary between -0.01 and -0.17 depending on the evolution scheme chosen. The measured value falls into this interval leaving any possible discrimination between various evolution schemes inconclusive.

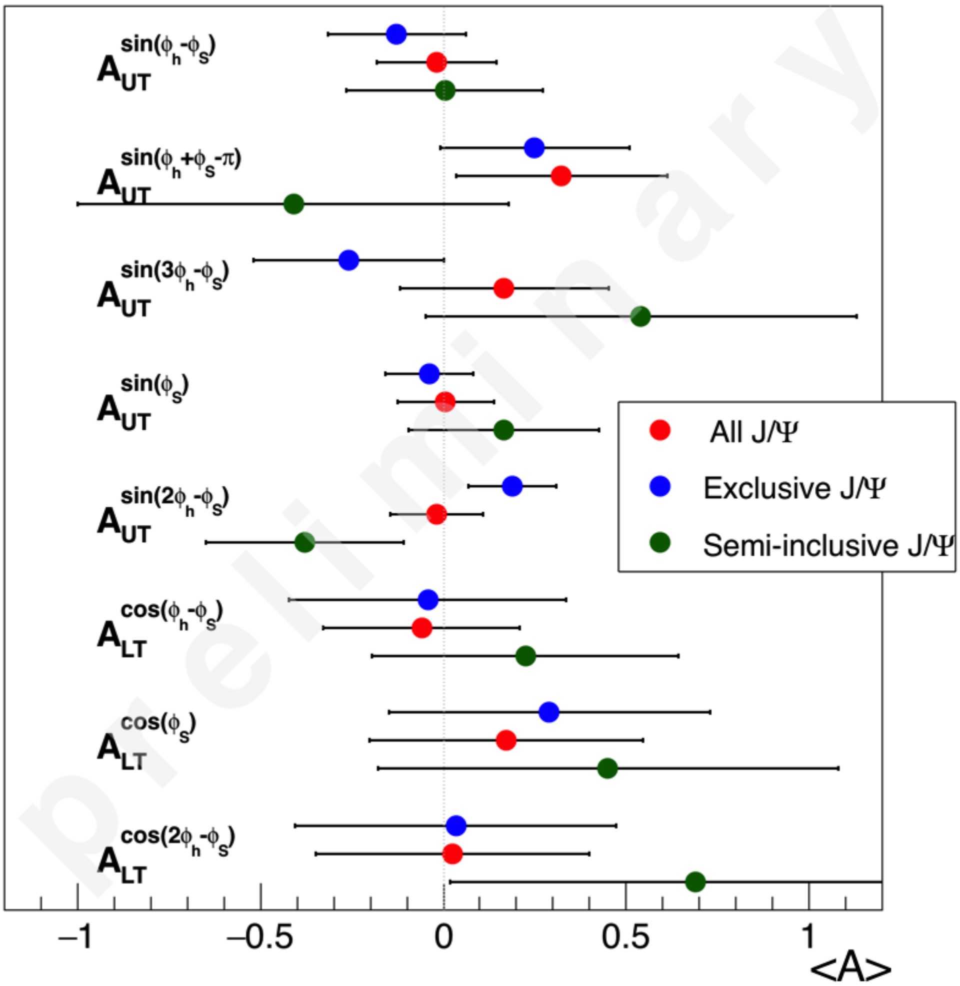

Figure 7.8: All the 8 TSAs extracted for all the three samples. Uncertainties are statistical only.

7.4 Systematics and Conclusion

The systematic error is given by the polarisation and dilution factor uncertainties. These are 5% scaling error for both the polarisation and dilution factor.

The false asymmetries might play role as well, but since we are dealing with very limited statistics, they could not be reliably extracted as they would suffer from the same problem as the physics asymmetries.

The J/ψ production and particularly the exclusive one, where the background is low, seems to be another possible channel to study the transverse spin asymmetries. However the present data sample does not allow for any particular conclusion. All the asymmetries are well compatible with zero within their large statistical uncertainties. In particular the Sivers asymmetry is:

$$A_{UT}^{\sin(\phi_h-\phi_S)} = -0.13 \pm 0.19_{stat}. \tag{7.2}$$

There are more COMPASS data coming in 2021 and also there are smaller samples collected prior to 2010. The estimated gain in statistics is a factor of about three. It seems that at least for COMPASS data this analysis poses rather an interesting exercise than a relevant physics result.

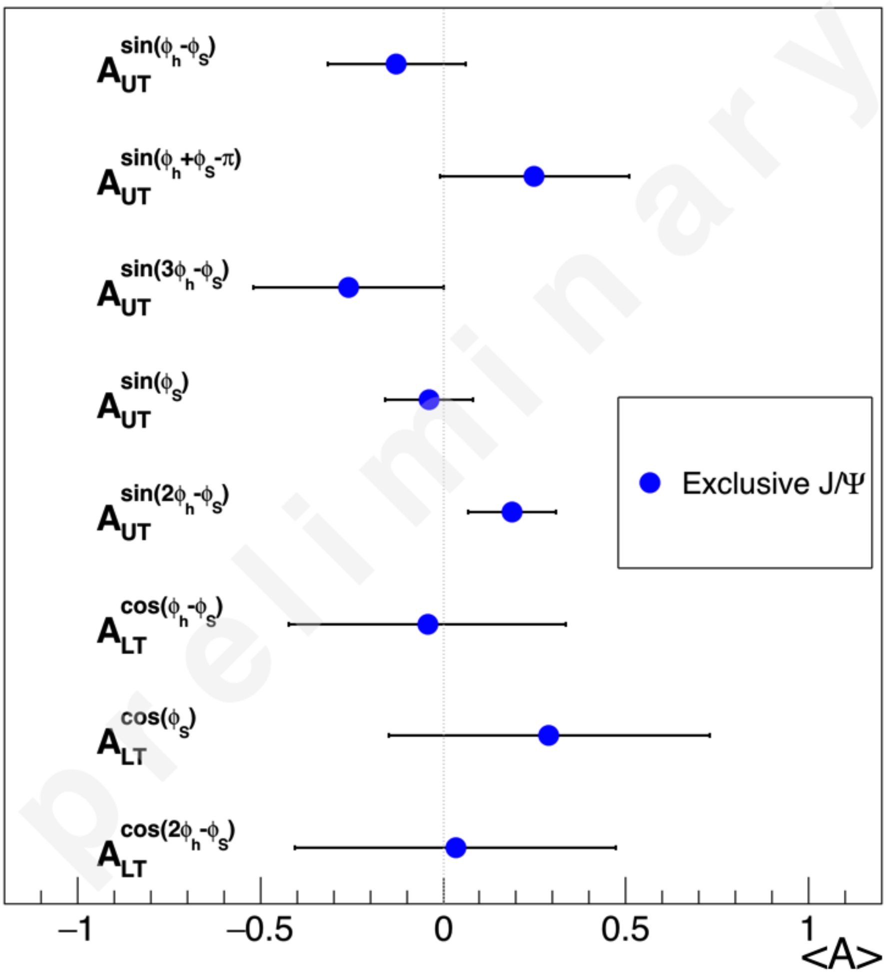

Figure 7.9: All the 8 TSAs extracted for the exclusive sample only. Uncertainties are statistical only.

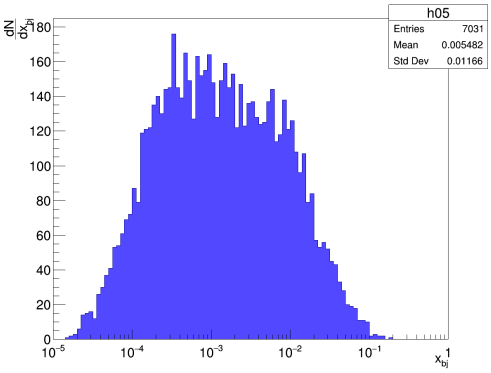

(a) exclusive $x_{bjorken}$

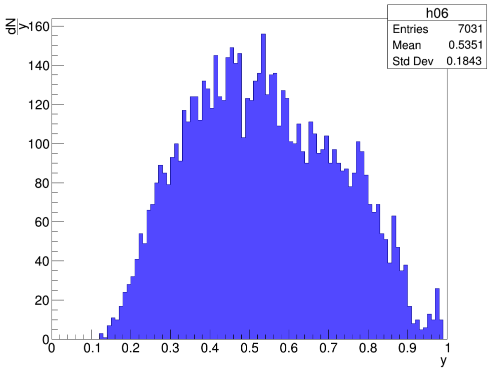

(b) exclusive y

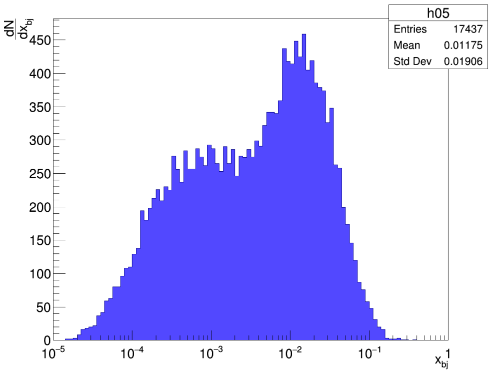

(c) full $x_{bjorken}$

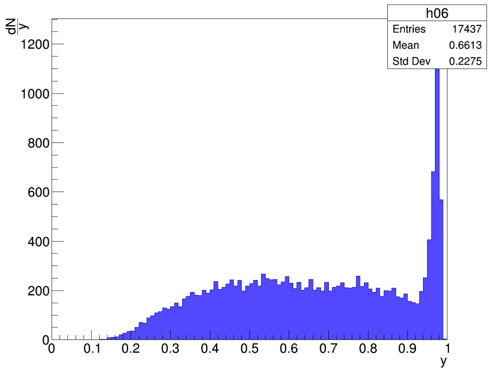

(d) full y

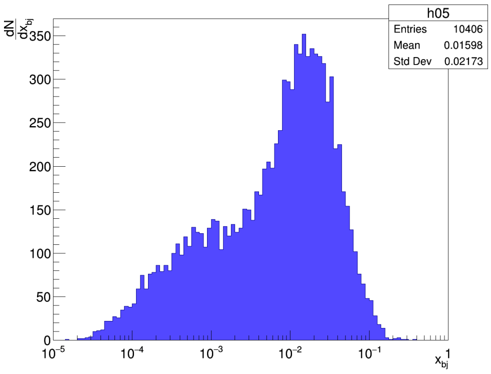

(e) inclusive $x_{bjorken}$

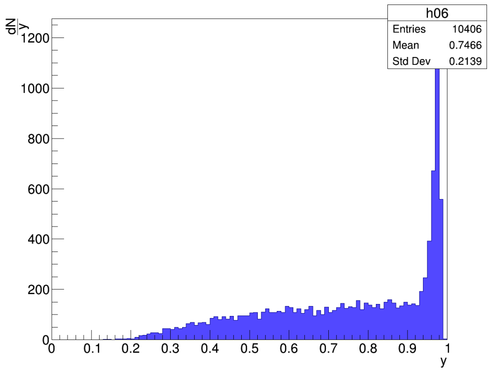

(f) inclusive y

Figure 7.5: $x_{bjorken}$ and y distributions for all three data samples.

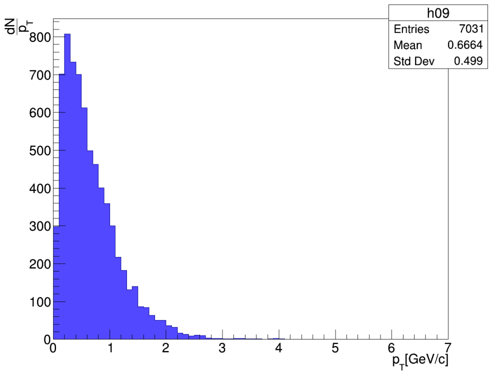

(a) exclusive P_T

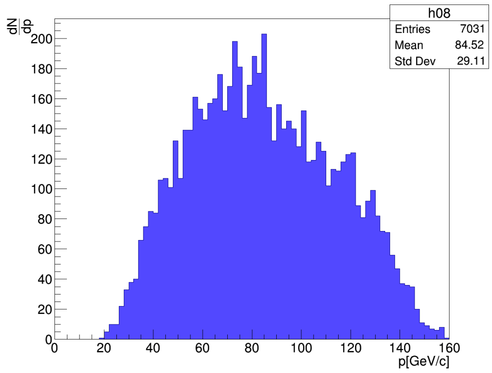

(b) exclusive P

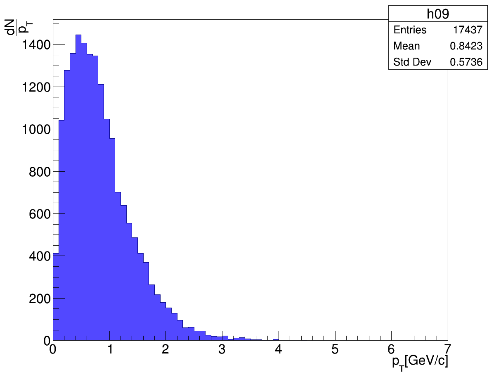

(c) full P_T

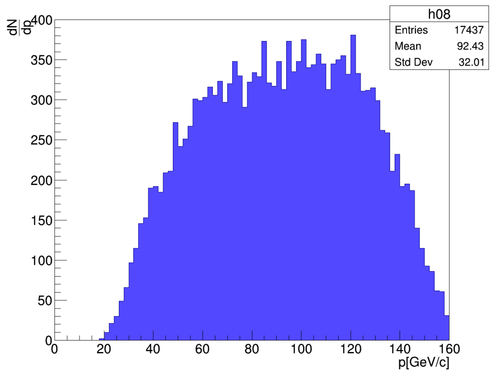

(d) full P

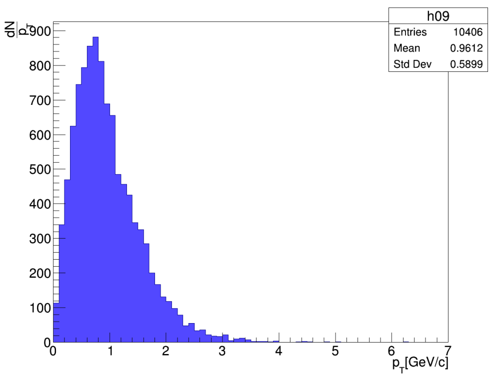

(e) inclusive P_T

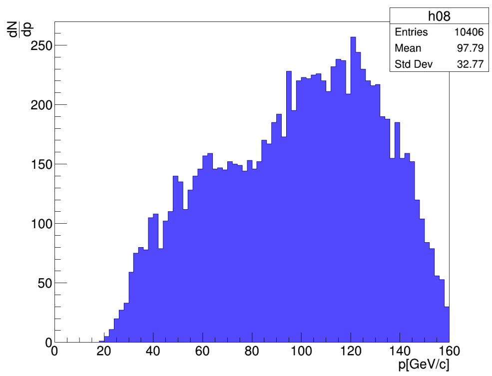

(f) inclusive P

Figure 7.6: P_T and P distributions for all three data samples.

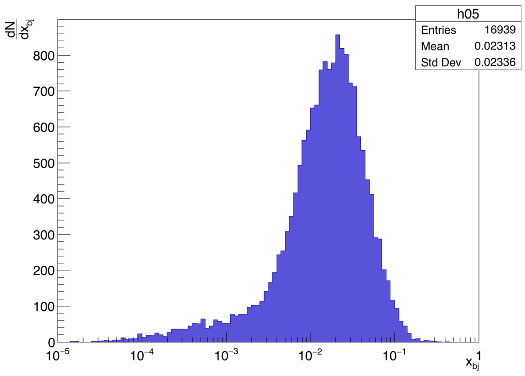

(a) $x_{bjorken}$

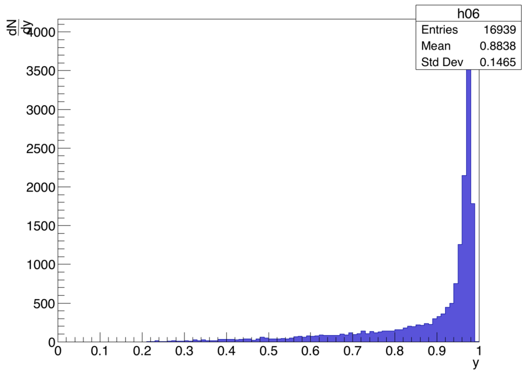

(b) y

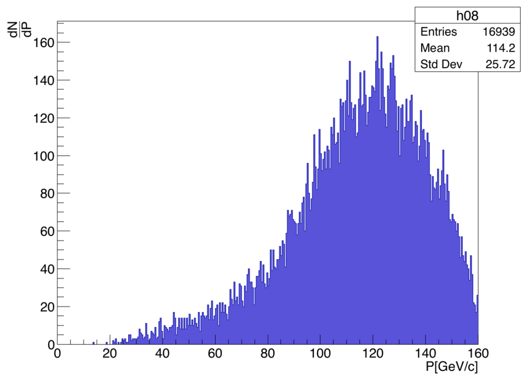

(c) J/ψ momentum

Figure 7.7: $x_{bjorken}$, y and the momentum distributions for the background sample. The same peaking structure is visible as in the distributions containing the J/ψ peak.

8. Transverse spin asymmetries in J/ψ production in 2015 Drell-Yan data

8.1 Data selection

The following cuts are used for the event selection:

1. Primary vertices with dimuon candidate - two tracks with opposite charge that have passed more than 30 radiation lengths (muon ID), either CORAL tagged best primary vertex is used, or in case of more common vertices the one with smallest χ^2 is used.
2. Dimuon trigger fired - only events that were triggered by either the Outer-Last dimuon trigger or Last-Last dimuon trigger, events with Middle-Last are vetoed to remove the events containing the beam decay muons (BDM).

   The BDM are predominantly produced at small angles $\theta_{lab} < 0.012$ and high momenta $p > 106$ GeV/c as follows from 2 body decay of 190 GeV/c pions. They can be removed by a simple momentum-angle cut, but also by removing the events with Middle-Last trigger fired, as they fall into its acceptance. The BDMs rejection is illustrated in Fig. 8.1.
3. Only tracks $Z_{first} < 300$ cm and $Z_{last} > 1500$ cm - selecting only tracks that have first point measured in front of SM1 magnet and last measured point behind MuonWall 1.
4. Time of μ^+ and μ^- tracks defined (defined with respect to the trigger time).
5. Time difference of the dimuon tracks $\Delta t < 5$ ns.
6. $\chi^2_{tracks} < 10$ - cut on quality of the reconstructed tracks.
7. Trigger validation - verifying that the muon tracks are in the geometrical acceptance of the trigger hodoscopes that triggered on them.
8. Bad spills and bad runs rejection.
9. Cuts on x_π, x_{N} and x_F - very few events are rejected (about 1 per 100 000).
10. Cut on $q_T > 0.4$ GeV/c - to ensure proper resolution of the azimuthal angles, see Fig. 8.2, and $q_T < 0.5$ GeV/c to remove the high q_T tail.
11. Cut on the Z-position of the vertex - require the vertices to be in the target cells, $Z_{vertex} \in [-294.5, -239.3] \,||\, [-219.5, -164.3]$ cm.
12. Radial cut on the vertex position $r < 1.9\ cm$ - require the vertices to be in the target cells.
13. Cut on the dimuon invariant mass $M_{\mu\mu} \in [3.0, 3.25]$ GeV/c^2.

In total there are 964869 ± 980 events left after all the selection criteria.

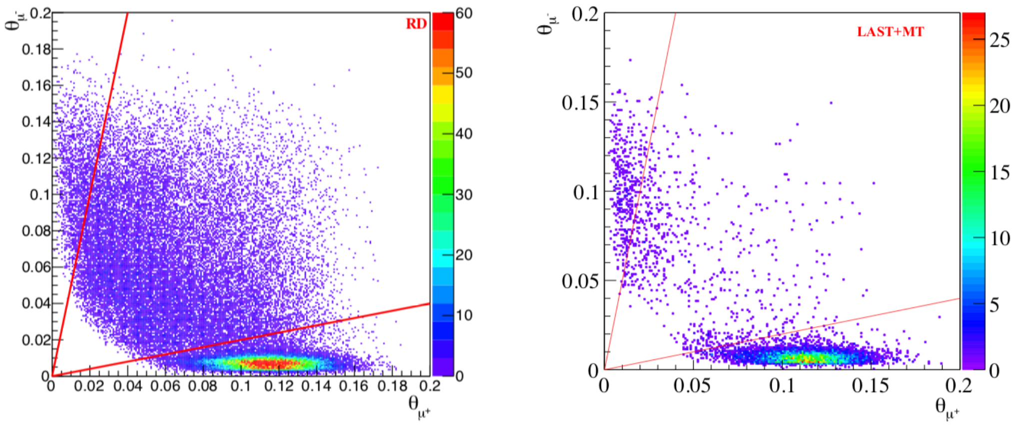

(a) Angular cut

(b) Middle-Last trigger events

Figure 8.1: Rejection of the BDM. (a) shows the alternative cut on the muon angle, while (b) shows the events in acceptance of the Middle-Last dimuon trigger, the BDM island is clearly visible, plots from Ref. [74; 78].

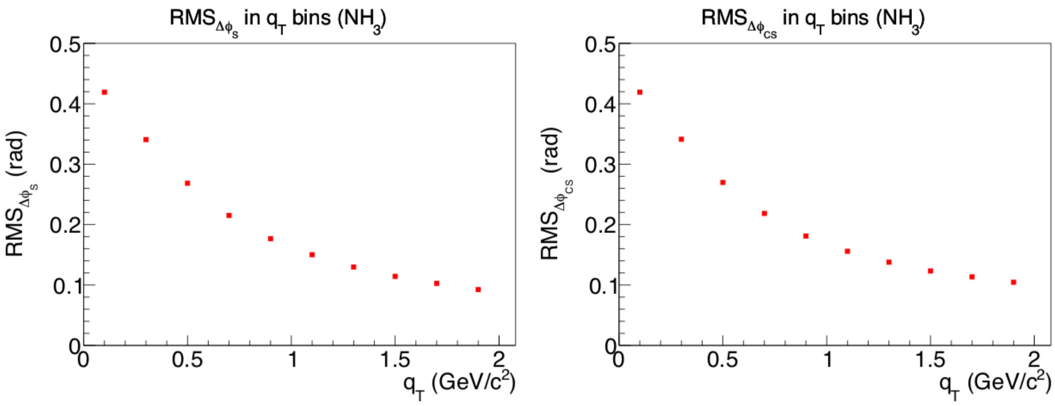

Figure 8.2: q_T dependence of the azimuthal angles resolutions, from Ref. [74].

8.2 Kinematic distribution

We shown in Fig. 8.3 the distribution of reconstructed vertices along the target region. The two cells of polarised target, the vertex detector, the aluminium target and the tungsten beam plug are clearly visible.

The Fig. 8.4 illustrates the full invariant mass distribution from 2.0 to 9 GeV/c^2. The Fig. 8.5 then shows the J/ψ peak. The conservative mass cut leads to very low level of background of about 4% [74]. The Fig. 8.6 shows the corresponding x_{N} vs x_π coverage and Fig. 8.7 shows the corresponding x_F distribution.

8.3 Results

The asymmetries are evaluated in 6 equally populated bins for each of the kinematic variables - x_F, x_π,x_{N} and q_T. The binning is summarised in the Tab. 8.1. The asymmetries are extracted using the double ratio method described in the Chapter 6. The raw asymmetries are corrected for the polarisation, the dilution

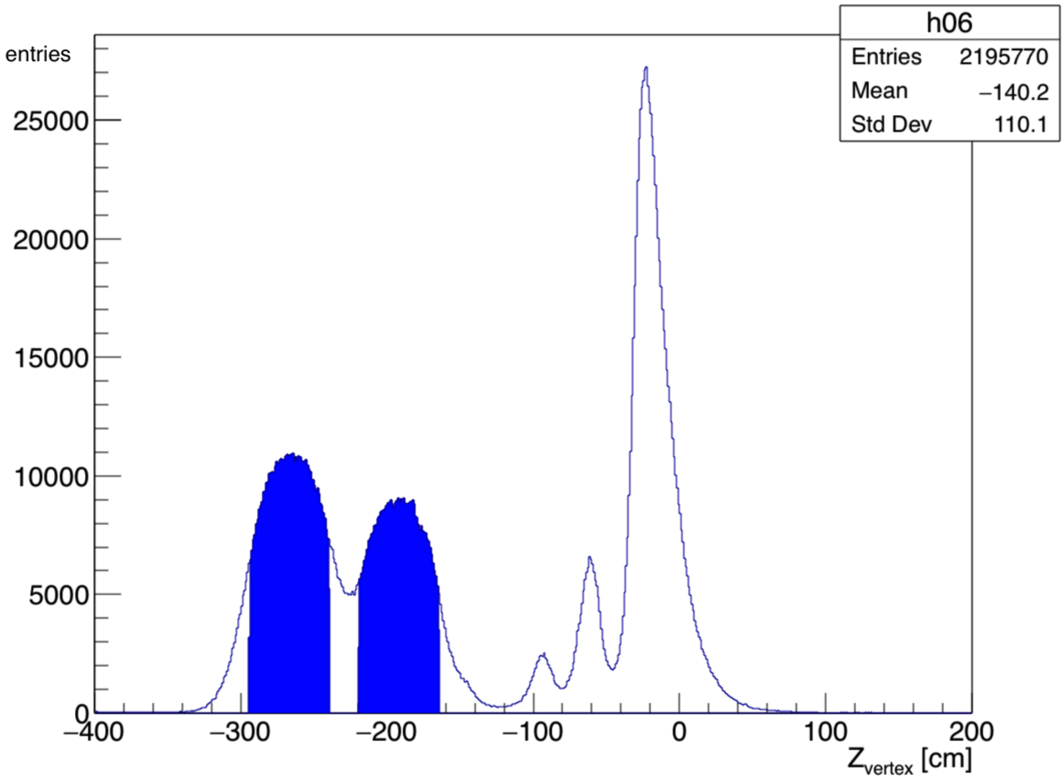

Figure 8.3: Z-vertex distribution with all the target components visible. The shaded area corresponds to the cut used in the physics analysis.

factor and the depolarisation factor. The kinematic dependencies of depolarisation factors are plotted in Fig. 8.9. Final values are then obtained as weighted average over the periods in each bin. The results together with the systematic uncertainties are summarised in Fig. 8.10, Fig. 8.11 and Fig. 8.12. The integrated asymmetries are plotted in the Fig. 8.13.

8.4 Systematics

The Fig. 8.14 shows the pull distributions for each of the measured asymmetries. We see that the data show good statistical compatibility.

Variable / Bin number	q_T [GeV/c]	x_F	x_{N}	x_π
1	0.4-0.62	-1.0-0.06	0.0-0.055	0-0.18
2	0.62-0.82	0.06-0.13	0.055-0.070	0.18-0.23
3	0.82-1.04	0.13-0.20	0.070-0.083	0.23-0.28
4	1.04-1.30	0.20-0.27	0.083-0.100	0.28-0.34
5	1.30-1.70	0.27-0.37	0.100-0.125	0.34-0.42
6	1.70-5.0	0.37-1.0	0.125-1.00	0.42-1.0

Table 8.1: Binning used in the analysis.

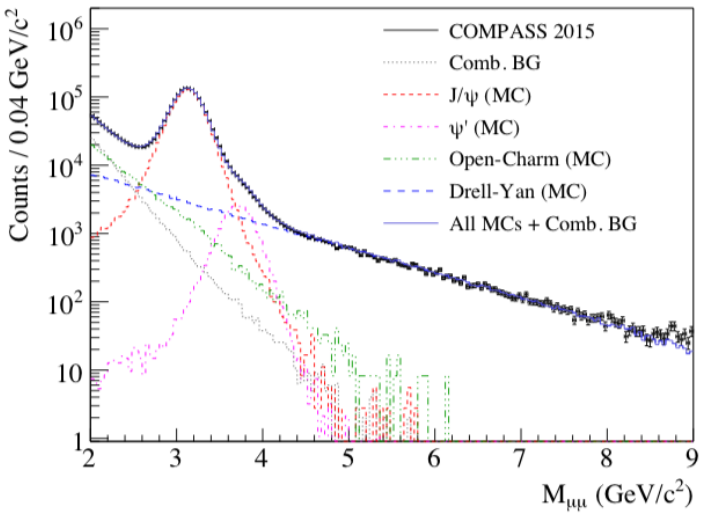

Figure 8.4: Invariant mass distribution of the dimuons in the mass range used at COMPASS. The various background contribution obtained from MC simulation are also shown. figure is taken from Ref. [74].

8.4.1 False asymmetries

We use the standard COMPASS recipe to determine the systematic uncertainties from the two types false asymmetries described in Chapter 6.

The basic idea is to check the compatibility of the measured false asymmetries FA with zero. We take conservative approach and if the probability of being compatible decreases below 50% we consider that as a systematic effect. For every bin in each period we can then express the σ_{syst} in terms of σ_{stat}:

- if $|FA_i| < 0.68\sigma_{stat,i}$ then $\frac{\sigma_{syst,i}}{sigma_{stat,i}} = 0$
- if $|FA_i| > 0.68\sigma_{stat,i}$ then $\frac{\sigma_{syst,i}}{\sigma_{stat,i}} = \sqrt{\frac{FA_i^2}{\sigma_{stat,i}^2} - 0.68^2}$.

The weighted average is then taken over the periods. Since the two types of false asymmetries are not completely uncorrelated we take the larger one of the two.

The σ_{syst} stemming from the false asymmetries is between $0.4\sigma_{stat}$ and $1.2\sigma_{stat}$ in each bin.

8.4.2 Polarisation and dilution factor

There is additional 5% scaling uncertainty stemming from the polarisation measurement.

The dilution factor is more complicated as there are no values available for the J/ψ mass range. We can extrapolate the available values for the high mass Drell-Yan [74] to the J/ψ mass range. This brings a value of about 0.16. We assign a rather conservative value of 10% scaling uncertainty to this value. It should be noted that since the dilution factor is a multiplicative factor it will not change the statistical significance of the measured asymmetries. This is also the reason why the effect on the total uncertainty is rather small since the measured asymmetries are also small.

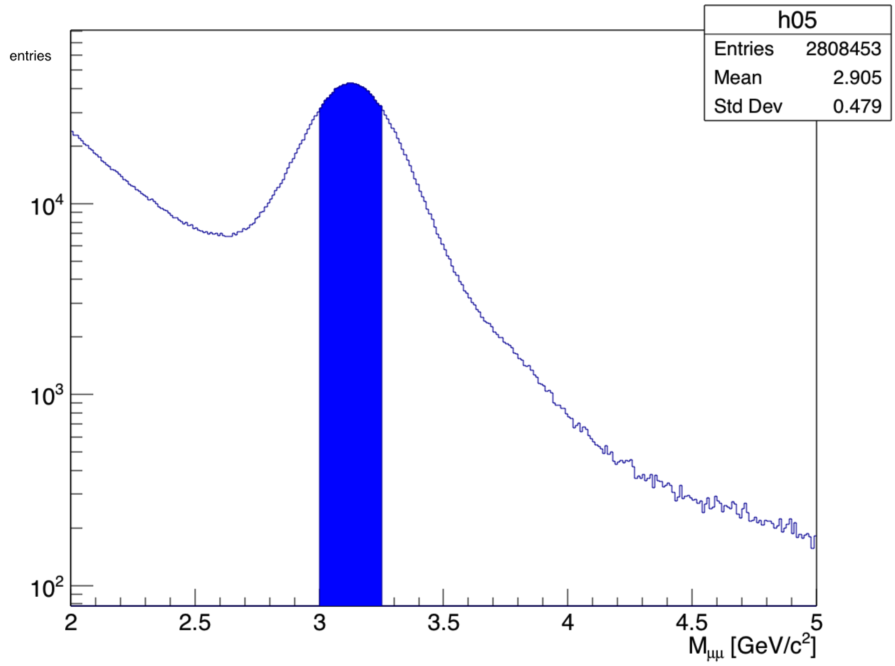

Figure 8.5: The J/ψ range of the invariant mass distribution, the shaded area corresponds to the mass cut used in the analysis.

8.4.3 Feed-down contribution and unpolarised asymmetry

Additional uncertainty might come from the, in principle unknown, values of the unpolarised asymmetry λ. It is expected to be close to one. However the only existing measurement [79] prefers rather small value albeit with large uncertainties. For evaluating the possible effect the value of λ was varied between zero and one. This brings at maximum additional 15% scaling uncertainty.

Final uncertainty might come from possible higher charmonia states which are decaying into J/ψ and thus polluting our sample. We expect this to be rather small effect. However it is not straightforward to estimate this without proper cross-section measurement available for the J/ψ production in J/ψ collisions. We will thus refer to the results as being asymmetries measured in the invariant mass range of the J/ψ rather than the asymmetries of prompt J/ψ.

8.5 Conclusion

We measured the leading twist transverse spin asymmetries in COMPASS 2015 polarised J/ψ data in the J/ψ mass range. At mean values of the kinematic variables $< q_T >= 1.16$ GeV/c, $< Q^2 >= 9.2$ (GeV/)c^2, $< x_{\mathrm{N}} >= 0.09$, $x_\pi = 0.3$, $< x_F >= 0.2$ the asymmetries are

- $A^{\sin\Phi_S} = 0.017 \pm 0.013_{stat} \pm 0.0074_{syst}$
- $A^{\sin(2\Phi-\Phi_S)} = 0.023 \pm 0.017_{stat} \pm 0.009_{syst}$
- $A^{\sin(2\Phi+\Phi_S)} = -0.007 \pm 0.017_{stat} \pm 0.012_{syst}$.

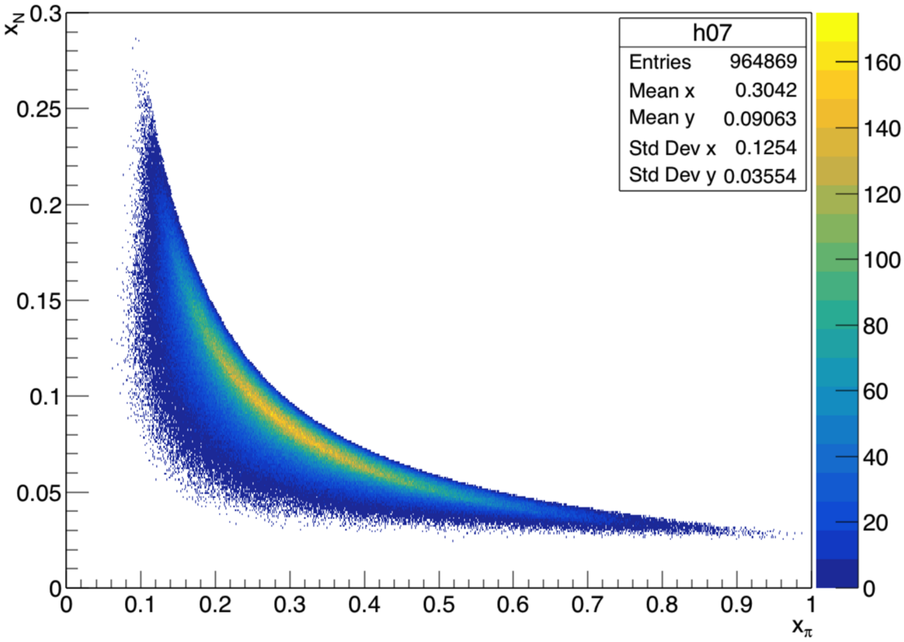

Figure 8.6: x_π vs x_N coverage of the J/ψ events.

All the asymmetries are found to be compatible with zero within the uncertainties. In particular the Sivers asymmetry $A^{\sin\Phi_S}$ is found to be very different with respect to the theoretical prediction in Ref.[37]. This might be possible due to different production mechanism than $q\bar{q}$ annihilation (like gluon-gluon fusion) or some unaccounted TMD evolution effects. This measurement will provide an important input to the TMD analysis.

In 2018 COMPASS collected almost twice the statistics available in 2015. This might, together with somewhat relaxed mass cut, provide enough statistics to perform a 2D measurement of the asymmetries.

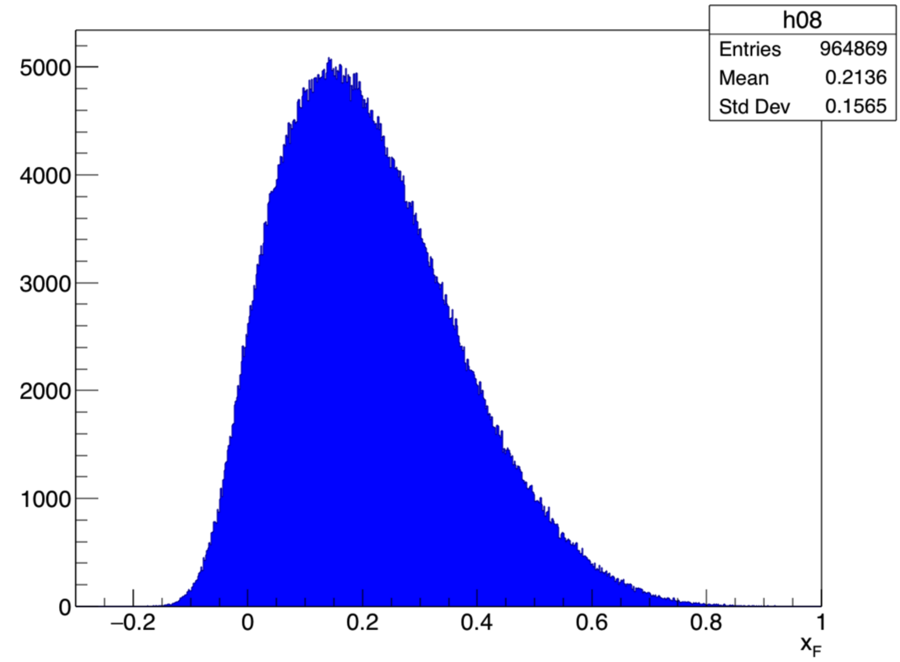

Figure 8.7: The x_F coverage of the J/ψ events.

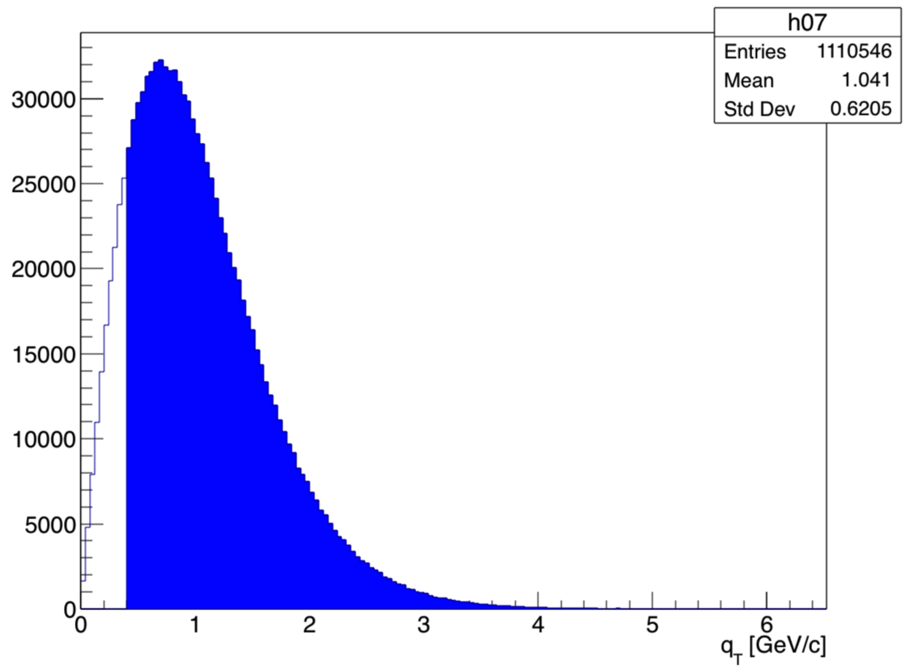

Figure 8.8: The q_T coverage of the J/ψ events, the shaded area corresponds to the mass cut used in the analysis.

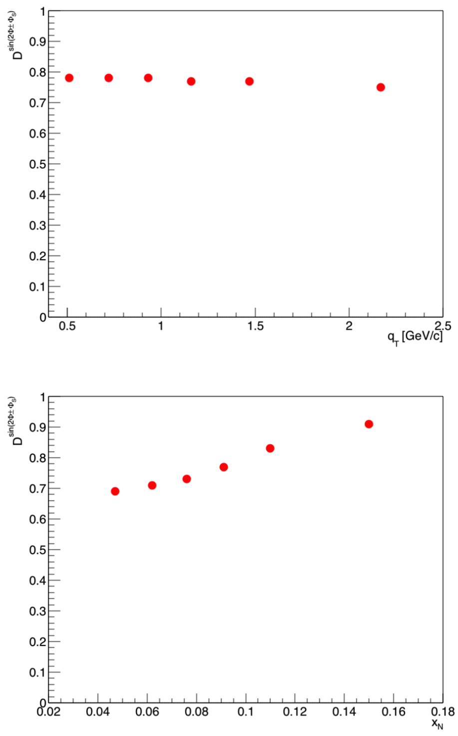

Figure 8.9: The kinematic dependencies of the depolarisation factor D for the transversity and pretzelosity related asymmetries. Note that D=1 for Sivers asymmetry by definition.

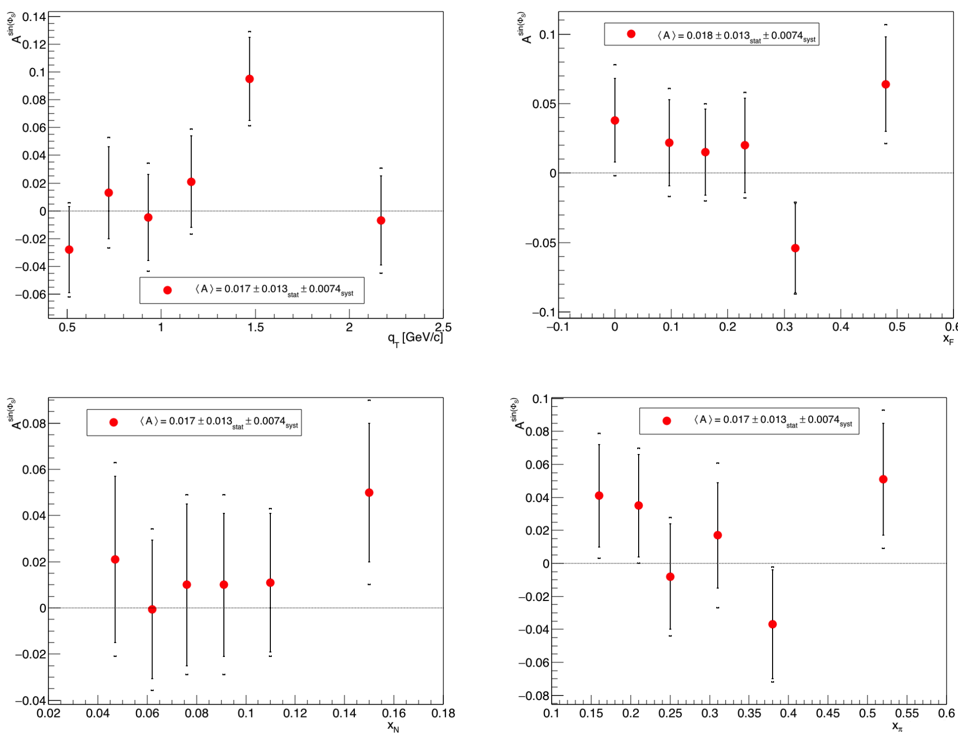

Figure 8.10: The Sivers asymmetry extracted in the four kinematic variables. The inner errors bars show the statistical uncertainty and the outer error bars show the total uncertainty.

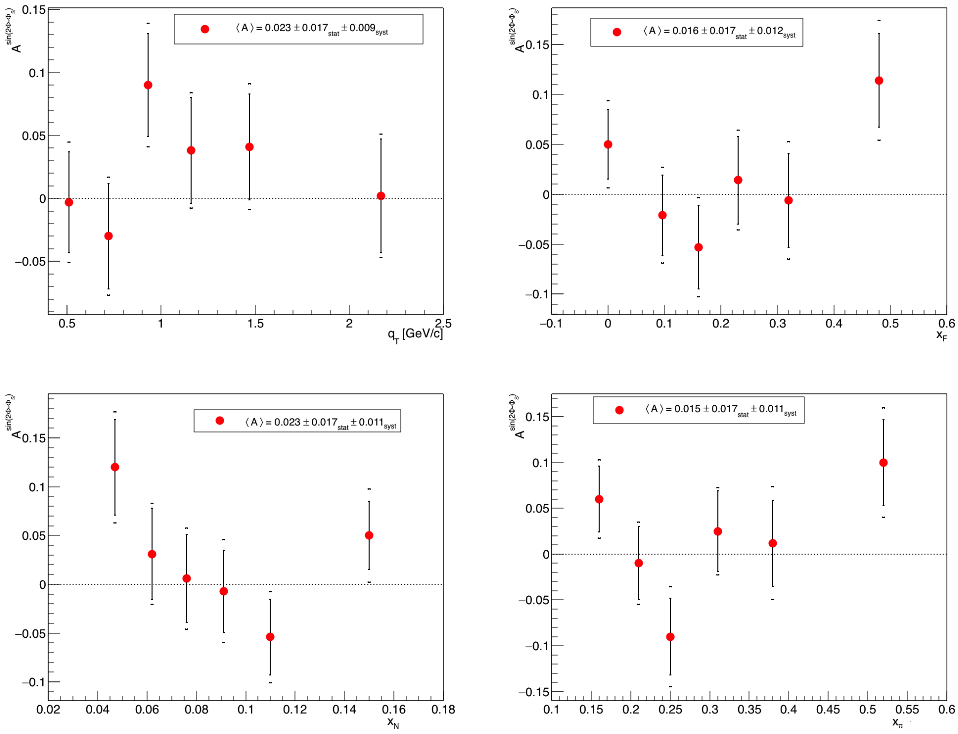

Figure 8.11: The transversity related asymmetry extracted in the four kinematic variables. The inner errors bars show the statistical uncertainty and the outer error bars show the total uncertainty.

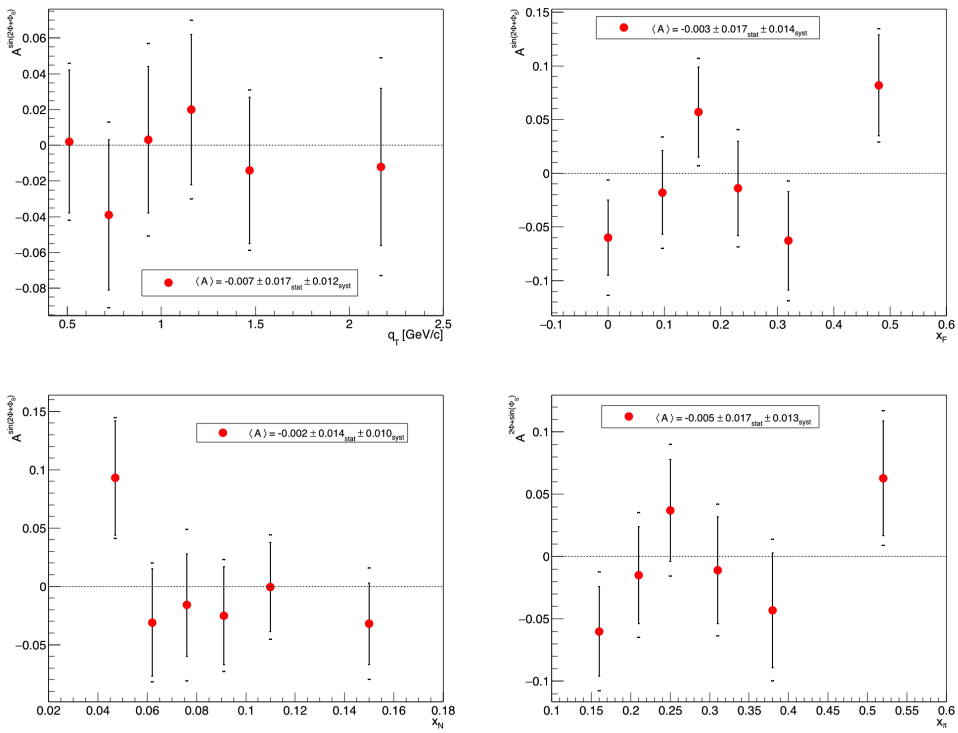

Figure 8.12: The pretzelosity related asymmetry extracted in the four kinematic variables. The inner errors bars show the statistical uncertainty and the outer error bars show the total uncertainty.

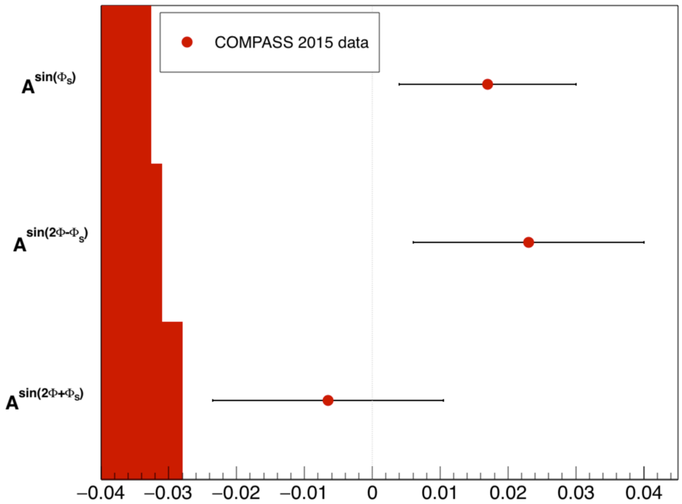

Figure 8.13: The integrated transverse spin asymmetries measured in the J/ψ mass range.

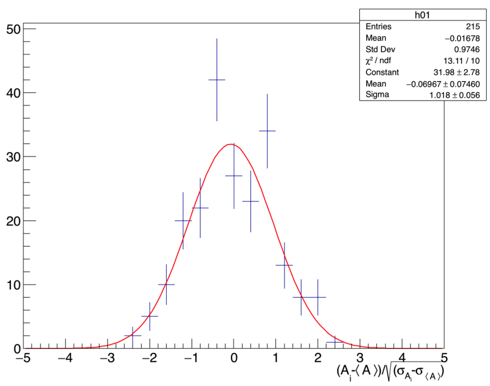

(a) Sivers

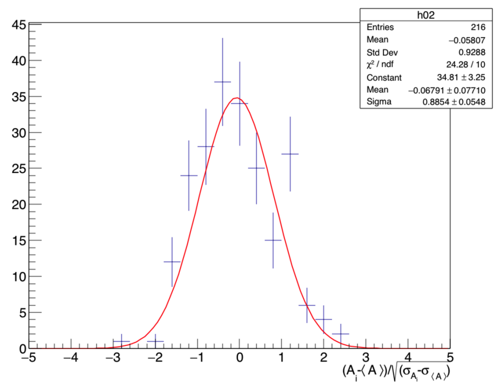

(b) Transversity

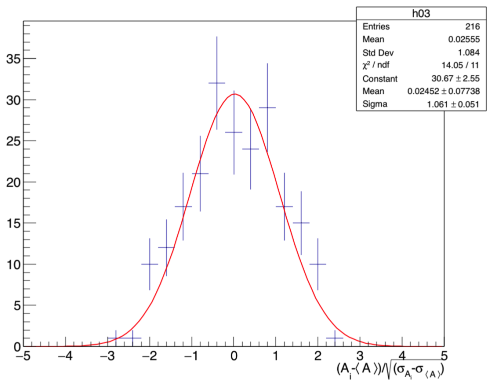

(c) Pretzelosity

Figure 8.14: The pull distribution for all the measured asymmetries. They show a good statistical compatibility.

Conclusion

In the present work we introduced the basic theoretical description of the nucleon spin structure. The concept of the TMDs was introduced and the related experimentally available processes were described.

The COMPASS experiment was presented with its two configurations as used in 2010 SIDIS data-taking, and 2015 and 2018 Drell-Yan data-taking. The polarised target was described in detail. In particular, some experimental results of its own were presented. We presented the measurement of the polarised ammonia behaviour in zero field yielding the relaxation times of (11 ± 0.5) minutes and (7.5 ± 0.5) minutes for positive and negative polarisations, respectively. The target material weight measurement for 2015 and 2018 was also presented along the packing factor determination. The packing factor was found to be improved for the downstream in 2018 as compared to 2015.

We presented two types of hardware related analyses - the express analysis and the detector efficiencies analysis. We presented the their importance and showed some relevant examples of potential hardware problems found during the course of the analyses.

We presented the analysis of 2010 SIDIS data. Specifically the transverse spin asymmetries were measured in J/ψ production. The exclusively produced J/ψ showed a rather clean signal. However, the measurement is statistically limited. In particular, the Sivers asymmetry, which is suggested to be used to determine the gluon Sivers distribution in the nucleon, is found to be $A^{\sin(\phi_h - \phi_S)} = -0.13 \pm 0.19_{stat}$.

Finally the measurement of the transverse spin asymmetries was performed using the 2015 COMPASS Drell-Yan data. All the leading twist asymmetries are found to be compatible with zero. Especially the Sivers asymmetry is found to be $A^{\sin(\phi_S)} = 0.017 \pm 0.013_{stat} \pm 0.0074_{syst}$. This results does not confirm the prediction by Anselmino et al. and does not allow for the test of the predicted sign-change of the Sivers function in SIDIS and Drell-Yan processes.

Bibliography

[1] Antille J. et al. , Spin dependence of the inclusive reaction p+p (polarized) $\rightarrow \pi^0$ + X at 24 GeV/c for high p_T π^0 produced in the central region, Phys. Lett. 94B, 523 (1980).

[2] Bunce G. et al., Λ^0 Hyperon Polarization in Inclusive Production by 300-GeV Protons on Beryllium, Phys. Rev. Lett. 36, 1113, 1976.

[3] Ashman J. et al., A measurement of the spin asymmetry and determination of the structure function g1 in deep inelastic muon-proton scattering, Physics Letters B, 206 (2): 364, 1988.

[4] Falciano S. et al., Angular Distributions of Muon Pairs Produced by 194-GeV/c Negative Pions, Z. Phys., C31, 513, 1986.

[5] Guanziroli M. et al., Angular Distributions of Muon Pairs Produced by Negative Pions on Deuterium and Tungsten, Z. Phys., C37, 545, 1988.

[6] Conway J.S. et al., Experimental Study of Muon Pairs Produced by 252 GeV Pions on Tungsten, Phys. Rev., D39, 92–122, 1989.

[7] Efremov A.V. et al., Spin structure of the nucleon and axial anomaly, Nuclear Physics B Vol. 346, Issue 1,97-114, 1990.

[8] D. Muller et al., Wave functions, evolution equations and evolution kernels from light ray operators of QCD, Fortsch. Phys. 42 (1994) 101.

[9] Ji X., Gauge-Invariant Decomposition of Nucleon Spin, Phys. Rev. Lett. 78, 610, 1997.

[10] Sivers D.W., Single Spin Production Asymmetries from the Hard Scattering of Point-Like Constituents. Phys. Rev., D41, 83, 1990.

[11] Boer D., Investigating the origins of transverse spin asymmetries at RHIC, Phys. Rev., D60, 014012, 1999.

[12] Baum G. et al., COMPASS proposal, CERN/SPSLC 96-14, 1996.

[13] Collins J.C., Foundations of perturbative QCD, Cambridge University Press, 2011.

[14] Cooper-Sarkar A., Devenish R., Deep Inelastic Scattering, Oxford University Press, 2004.

[15] Matoušek J., Nucleon spin structure studies in Drell–Yan process at COMPASS, PhD thesis, 2018.

[16] V. Barone, A. Drago, and P. G. Ratcliffe. Transverse polarisation of quarks in hadrons. Phys. Rept., 359, 1–168, 2002.

[17] E. D. Bloom et al. High-Energy Inelastic e p Scattering at 6-Degrees and 10-Degrees. Phys. Rev. Lett., 23, 930–934, 1969.

[18] Feynman R.P., The behavior of hadron collisions at extreme energies, Conf.Proc. C690905 (1969) 237-258.

[19] Cejnar P., A Condensed Course of Quantum Mechanics, Karolinum, 2015.

[20] Chyla J., Quark, Partons and Quantum Chromodynamics, published online,https://www.fzu.cz/˜chyla/lectures/text.pdf, 2004.

[21] Wilson, K., Confinement of quarks, Physical Review D. 10, 1974.

[22] Aybat S.M. and Rogers T.C., TMD Parton Distribution and Fragmentation Functions with QCD Evolution, Phys. Rev., D83, 114042, 2011.

[23] Bacchetta A. et al., Semi-inclusive deep inelastic scattering at small transverse momentum, J. High Energy Phys., 02, 093, 2007.

[24] Adams B. et al. COMPASS++/AMBER: Proposal for Measurements at the M2 beam line of the CERN SPS Phase-1: 2022-2024, SPSC-P-CERN, 2019.

[25] Adolph C. et al., 05.01.2017 First measurement of the Sivers asymmetry for gluons from SIDIS data, PLB 772 (2017) 854.

[26] Alekseev M. et al, Direct Measurement of the Gluon Polarisation in the Nucleon via Charm Meson Production, hep-ex/0802.3023. 2008.

[27] Godbole R.M. et al., Transverse Single Spin Asymmetry in $e+p^{\uparrow} \to e+J/\psi+X$ and Transverse Momentum Dependent Evolution of the Sivers Function. Phys. Rev., D88(1), 014029, 2013.

[28] Mukherjee A. et al.,J/ψ Production in Polarized and Unpolarized ep Collision and Sivers and $\cos 2\Phi$ Asymmetries , Eur.Phys.J. C77 (2017) no.12, 854.

[29] Drell S.D. and Yan T.M., Massive Lepton Pair Production in Hadron-Hadron Collisions at High-Energies, Phys. Rev. Lett., 25, 316– 320, 1970.

[30] Arnold S, Metz A., and Schlegel M., Dilepton production from polarized hadron hadron collisions, Phys. Rev., D79, 034005, 2009.

[31] Lam C.S. and Tung W.K., A Systematic Approach to Inclusive Lepton Pair Production in Hadronic Collisions, Phys. Rev., D18, 2447, 1978.

[32] Lam C.S. and Tung W.K., A Parton Model Relation Sans QCD Modifications in Lepton Pair Productions, Phys. Rev., D21, 2712, 1980.

[33] Zhu L. Y. et al., Measurement of Angular Distribu- tions of Drell-Yan Dimuons in p+p Interactions at 800 GeV/c, Phys. Rev. Lett., 102, 182001, 2009.

[34] Zhu L. Y. et al., Measurement of Angular Distributions of Drell-Yan Dimuons in p+d Interaction at 800 GeV/c, Phys. Rev. Lett., 99, 082301, 2007.

[35] Lambertsen M. and Vogelsang W., Drell-Yan lepton angular distributions in perturbative QCD, Phys. Rev., D93(11), 114013, 2016.

[36] Nakano K. (E906/SeaQuest Coll.), Measurement of Boer-Mulders Function via Drell-Yan Process by SeaQuest Experiment at Fermilab. Int. J. Mod. Phys. Conf. Ser., 40, 1660041, 2016.

[37] Anselmino M. et al., The Sivers asymmetry in Drell–Yan production at the J/ψ peak at COMPASS, Phys.Lett. B770 (2017) 302-306.

[38] Guzey V., A U.S.-based Electron-Ion Collider, J.Phys.Conf.Ser. 1390 (2019) no.1, 012123.

[39] Tanabashi M. et al. (Particle Data Group), Phys. Rev. D 98, 030001 (2018).

[40] Adolph C. et al., Experimental investigation of transverse spin asymmetries in $\mu^{-}p$ SIDIS processes: Collins asymmetries, Phys. Lett., B717, 376–382, 2012.

[41] Adolph C. et al., A high-statistics measurement of transverse spin effects in dihadron production from muon–proton semi-inclusive deep-inelastic scattering, Phys. Lett., B736, 124–131, 2014.

[42] Abe K. et al., Measurement of azimuthal asymmetries in inclusive production of hadron pairs in $e^{+}e^{-}$ annihilation at Belle, Phys. Rev. Lett., 96, 232002, 2006.

[43] M. Radici, A. Courtoy, A. Bacchetta, and M. Guagnelli. Improved extraction of valence transversity distributions from inclusive dihadron production. JHEP, 05, 123, 2015.

[44] Augsten K. et al., Addendum to the COMPASS-II Proposal for 2021/22: d-quark Transversity and Proton Radius, CERN-SPSC-2017-034, CERN, 2017.

[45] Anselmino et al., Study of the sign change of the Sivers function from STAR Collaboration W/Z production data, JHEP, 04, 046, 2017.

[46] Aghasyan M. et al, First measurement of transverse-spin-dependent azimuthal asymmetries in the Drell-Yan process, PRL 119 (2017) 112002.

[47] Adamczyk L. et al., Measurement of the transverse single- spin asymmetry in p+p to W/Z at RHIC, PRL 116(13), 132301, 2016.

[48] Bernhard J. et al., Studies for New Experiments at the CERN M2 Beamline within "Physics Beyond Colliders", arXiv:1911.01498v1 [hep-ex], 2019.

[49] Jasinski P., Analysis of diffractive dissociation of K^{-} into $K^{-}\pi^{+}\pi^{-}$ on a liquid hydrogen target at the COMPASS spectrometer, University of Mainz, 2012.

[50] Bovet C. et al., The Cedar Project. Cherenkov Differential Counters with Achromatic Ring Focus, IEEE Trans.Nucl.Sci. 25 (1978) 572-576.

[51] Abbon P. et al., The COMPASS experiment at CERN, NIMA 577 (2007) 455–518.

[52] Agarwala J. et al., Novel MPGD based detectors of single photons in COMPASS RICH-1, NIMA 912 (2018) 158-162.

[53] Barth J. et al., Trigger configuration summary 2002-2012, COMPASS note 2016-4, 2016.

[54] Huber S. et al., Intelligence Elements and Performance of the FPGA-based DAQ of the COMPASS Experiment, PoS TWEPP-17 (2018) 127.

[55] PHAST webpage, http://ges.home.cern.ch/ges/phast/index.html, accessed in January 2020.

[56] Andrieux V. et al., Transverse-spin-dependent azimuthal Drell-Yan asymmetries from COMPASS 2015 data, COMPASS release note, March 2017.

[57] Abragam A., Goldman M., Principles of dynamic nuclear polarisation, Rep. Prog. Phys. 41 (1978), 395.

[58] Kondo K., The polarization measurement and the feature investigation of the COMPASS 6LiD target, Nagooya University, 2004.

[59] Pešek M. , Low temperature polarized target for spin structure studies of nucleons at COMPASS, Charles University, 2014.

[60] Nukazuka G., various presentation during target meetings, CERN, 2019.

[61] Ventura G., Risegari L., The Art of cryogenics, Elsevier, 2008.

[62] Doshita N. et al., Performance of the COMPASS polarized target dilution refrigerator, NIMA 526 (2004), 138-143.

[63] Bielert E.R. et al. Operational Experience With the Combined Solenoid/Dipole Magnet System of the COMPASS Experiment at CERN, IEEE TRANSACTIONS ON APPLIED SUPERCONDUCTIVITY, VOL. 28, NO. 3, APRIL 2018.

[64] website of Cryomech Inc., http://www.cryomech.com, accessed in December 2019.

[65] Adams D. et al. The polarized double cell target of the SMC, Nucl.Instrum.Meth. A437 (1999) 23-67.

[66] Court G.R. et al., A high precision Q-meter for the measurement of proton polarization in polarised targets, NIMA 324 issue 3 (1993) 433-440.

[67] web page of National Instruments, http://www.ni.com.

[68] Mayer W., private communication, 2018.

[69] Mayer W. et al. Proceedings of 4^{th} international workshop on polarised target materials and techniques, pp. 23–32 (1984).

[70] Neliba S. et al., Weight and volume measurement of the large COMPASS target NIMA 526 (2004) 144-146.

[71] Panknin R., Bau und Installation eines neuen Veto-Detektors am COMPASS-Experiment am CERN, Diploma thesis, University of Bonn, 2006.

[72] Franco C. Vertex detector in 2015, Presentation at Drell-Yan meeting, 20.3.2017.

[73] Bernhard Ketzer, private communication, 2017.

[74] Andrieux V. et al., Transverse-spin-dependent azimuthal Drell-Yan asymmetries from COMPASS 2015 data, COMPASS release note, 2017, available at http://wwwcompass.cern.ch/compass/results/2017/march_polarised_DY/.

[75] Adolph C. et al., Collins, Sivers and two hadron asymmetries from the 2010 transversely polarized proton data, COMPASS release note, 2011, accessible at http://wwwcompass.cern.ch/compass/results/.html/2011/august_transv_1h/index.html.

[76] Eadie W.T et al., Statistical Methods in Experimental Physics, North-Holland Amsterdam, 1971, pp. 269–271.

[77] Boughezal R., et al., ”Color-singlet production at NNLO in MCFM”, The European Physical Journal C 77 (2016) 1.

[78] Parsamyan B. et al., COMPASS Drell-Yan 2015 data with NH3 and W targets: ongoing analysis Kinematic distributions and projected uncertainties for the asymmetries, COMPASS release note, 2016, available at http://wwwcompass.cern.ch/compass/results/2016/june_DY/.

[79] Badier J. et al., Experimental J/ψ hadronic production from 150 to 280 GeV/c, Zeitschrift fur Physik C Particles and Fields 20,1983, 101–116.

List of Figures

1.1 DIS diagrams . . . 6
1.2 Helicity amplitudes . . . 9
1.3 SIDIS Feynman diagram . . . 11
1.4 SIDIS reference frame . . . 12
1.5 DY Feynman diagram . . . 15
1.6 DY reference frames . . . 15
1.7 Predicted Sivers asymmetry . . . 17
1.8 Number and helicity measurements . . . 18
1.9 Transversity extraction . . . 19
1.10 Sivers extraction . . . 19
1.11 Sivers sign change 1 . . . 20
1.12 Sivers sign change 2 . . . 20

2.1 M2 beamline . . . 21
2.2 Beam composition . . . 22
2.3 CEDAR principle . . . 23
2.4 Target region DY . . . 24
2.5 2010 setup . . . 25
2.6 Micromegas and GEM principles . . . 26
2.7 RICH detector . . . 27
2.8 Trigger matrix . . . 30
2.9 Trigger elements . . . 31

3.1 DNP levels . . . 35
3.2 Spin temperature . . . 35
3.3 NMR signals . . . 37
3.4 Curie fit . . . 37
3.5 Phase diagram of ^{3}He/^{4}He. . . . 38
3.6 Cooling power . . . 39
3.7 Dilution fridge scheme . . . 40
3.8 Target magnet layout[1]. . . . 41
3.9 The microwave setup . . . 42
3.10 NMR system . . . 44
3.11 The weighting setup . . . 45
3.12 Zero field measurement explained . . . 47
3.13 Zero field measurement results . . . 48

4.1 Good run . . . 50
4.2 No PMM . . . 53
4.3 No MWPCs . . . 54

5.1 Sketch of Veto Inner 2 and SciFi03 . . . 56
5.2 Scifi01 efficiencies . . . 57
5.3 SciFi15 and SciFi03 efficiencies . . . 57
5.4 Vertex detector efficiencies . . . 58
5.5 GEM06 efficiencies . . . 58

6.1 Bad spill analysis 61
6.2 Bad runs analysis 62

7.1 Exclusive J/ψ 66
7.2 Full and inclusive sample 66
7.3 Z-vertex distributions 67
7.4 E_{miss} distribution 68
7.8 8 TSAs 69
7.9 8 TSAs Exclusive 70
7.5 $x_{bjorken}$ and y distributions 71
7.6 J/ψs P_T and P 72
7.7 Background distributions 73

8.1 BDM rejection 75
8.2 Azimuthal angles resolutions 75
8.3 Z vertex 76
8.4 Mass distribution 77
8.5 Mass J/ψ 78
8.6 x_π vs x_N 79
8.7 x_F distribution 80
8.8 q_T distribution 80
8.9 Depolarisation factors 81
8.10 Sivers asymmetry 81
8.11 Transversity related asymmetry 82
8.12 Pretzelosity related asymmetry 82
8.13 Integrated asymmetries 83
8.14 Pull distributions 83

List of Tables

1.1 Leading twist TMDs 9

3.1 Weight of the material 46
3.2 Packing factor 46

6.1 DY rejection rates 62

8.1 Binning 76

List of Abbreviations

AMBER - Apparatus for Meson and Baryon Experimental research
CEDAR - CErenkov Detector with AchRromatic focus
CERN - Conseil Europeane pour la Recherche Nucleaire
COMPASS - COmmon Muon and Proton Apparatus for Structure and Spectroscopy
CORAL - COmpass Reconstruction Algorithm Library
DAQ - Data AcQuisition
DC - Drift Chamber
DIS - Deep Inelastic Scattering
DR - Dilution Refrigerator
DCS - Detector Control System
FF - Fragmentation Function
GEM - Gas Electron Multiplier
NMR - Nuclear Magnetic Resonance
PDF - Parton Distribution Function
PMT - Photomultiplier
QCD - Quantum Chromo-Dynamics
QED - Quantum Electro-Dynamics
RICH - Ring Imaging Cherenkov detector
SciFi - Scintillating Fibres
SIDIS - Semi Inclusive DIS
SPS - Super Proton Synchrotron
TMD - Transverse Momentum Dependent PDF

List of publications

1. Gerhard Reicherz (Ruhr U., Bochum) et al., COMPASS polarized target in 2018 and 2021, PoS SPIN2018 (2019) 097

2. COMPASS Collaboration (M.G. Alexeev (Turin U.) et al.), Measurement of PT-weighted Sivers asymmetries in leptoproduction of hadrons,Nucl.Phys. B940 (2019) 34-53

3. B. Adams (Chicago U., EFI and Xonics Inc.) et al., Letter of Intent: A New QCD facility at the M2 beam line of the CERN SPS (COMPASS++/AMBER), CERN-SPSC-2019-003 (SPSC-I-250),e-Print: arXiv:1808.00848 [hep-ex] — PDF

4. Gerhard Reicherz (Ruhr U., Bochum) et al., Future plannings for the COMPASS polarized target, PoS PSTP2017 (2018) 004

5. COMPASS Collaboration (M. Aghasyan (INFN, Trieste) et al.), Light isovector resonances in $\pi^- p \to \pi^- \pi^- \pi^+ p$ at 190 GeV/c, Phys.Rev. D98 (2018) no.9, 092003

6. COMPASS Collaboration (R. Akhunzyanov (Dubna, JINR) et al.), Transverse extension of partons in the proton probed in the sea-quark range by measuring the DVCS cross section, Phys.Lett. B793 (2019) 188-194

7. COMPASS Collaboration (R. Akhunzyanov (Dubna, JINR) et al.), K- over K+multiplicity ratio for kaons produced in DIS with a large fraction of the virtual-photon energy , Phys.Lett. B786 (2018) 390-398

8. COMPASS Collaboration (M. Aghasyan (INFN, Trieste) et al.), Longitudinal double-spin asymmetry A1p and spin-dependent structure function g1p of the proton at small values of x and Q2, Phys.Lett. B781 (2018) 464-472

9. COMPASS Collaboration (M. Aghasyan (INFN, Trieste) et al.), Transverse-momentum-dependent Multiplicities of Charged Hadrons in Muon-Deuteron Deep Inelastic Scattering, Phys.Rev. D97 (2018) no.3, 032006

10. J. Matousek (Charles U.) et al., Polarised target for Drell-Yan experiment in COMPASS at CERN, part I, e-Print: arXiv:1709.06833 [physics.ins-det]

11. JPAC and COMPASS Collaborations (A. Jackura (Indiana U.) et al.). ,New analysis of $\eta\pi$ tensor resonances measured at the COMPASS experiment, Phys.Lett. B779 (2018) 464-472

12. COMPASS Collaboration (M. Aghasyan (INFN, Trieste) et al.), Search for muoproduction of X(3872) at COMPASS and indication of a new state X-tilde(3872), Phys.Lett. B783 (2018) 334-340

13. COMPASS Collaboration (M. Aghasyan (INFN, Trieste) et al.), First measurement of transverse-spin-dependent azimuthal asymmetries in the Drell-Yan process, Phys.Rev.Lett. 119 (2017) no.11, 112002

14. COMPASS Collaboration (C. Adolph (Erlangen - Nuremberg U.) et al.), First measurement of the Sivers asymmetry for gluons using SIDIS data, Phys.Lett. B772 (2017) 854-864

15. COMPASS Collaboration (C. Adolph (U. Erlangen-Nuremberg (main)) et al.), Final COMPASS results on the deuteron spin-dependent structure function g1d and the Bjorken sum rule, Phys.Lett. B769 (2017) 34-41

16. COMPASS Collaboration (C Adolph (U. Erlangen-Nuremberg (main)) et al.), Sivers asymmetry extracted in SIDIS at the hard scales of the Drell–Yan process at COMPASS, Phys.Lett. B770 (2017) 138-145

17. COMPASS Collaboration (C. Adolph (U. Erlangen-Nuremberg (main)) et al.), Azimuthal asymmetries of charged hadrons produced in high-energy muon scattering off longitudinally polarised deuterons, Eur.Phys.J. C78 (2018) no.11, 952

18. COMPASS Collaboration (C. Adolph (Erlangen - Nuremberg U.) et al.), Multiplicities of charged kaons from deep-inelastic muon scattering off an isoscalar target, Phys.Lett. B767 (2017) 133-141

19. COMPASS Collaboration (C. Adolph (Erlangen - Nuremberg U.) et al.), Exclusive ω meson muoproduction on transversely polarised protons, Nucl.Phys. B915 (2017) 454-475

20. COMPASS Collaboration and COMPASS Polarized Target Group (M. Finger et al.), COMPASS Polarized Target for Pion-induced Drell–Yan Experiment, Nucl.Part.Phys.Proc. 273-275 (2016) 2557-2559

21. COMPASS Collaboration (C. Adolph (Erlangen - Nuremberg U.) et al.), Multiplicities of charged pions and charged hadrons from deep-inelastic scattering of muons off an isoscalar target, Phys.Lett. B764 (2017) 1-10

22. COMPASS Collaboration (Michael Pešek (Charles U./Turin U.) for the collaboration), Upgraded polarized target for polarized Drell-Yan measurement at COMPASS, J.Phys.Conf.Ser. 678 (2016) no.1, 012005

23. Jaakko Henrik Koivuniemi (Ruhr U., Bochum (main)) et al., Large COMPASS polarized solid state target for Drell-Yan physics, PoS PSTP2015 (2015) 015

24. COMPASS Collaboration (C Adolph (Erlangen - Nuremberg U.) et al., Longitudinal double spin asymmetries in single hadron quasi-real photoproduction at high pT, Phys.Lett. B753 (2016) 573-579

25. COMPASS Collaboration (C Adolph (Erlangen - Nuremberg U.) et al.), Resonance Production and $\pi\pi$ S-wave in $\pi^- p \to \pi^-\pi^-\pi^+ p$ at 190 GeVc, Phys.Rev. D95 (2017) no.3, 032004

26. COMPASS Collaboration (C. Adolph (Erlangen - Nuremberg U.) et al.), Interplay among transversity induced asymmetries in hadron leptoproduction, Phys.Lett. B753 (2016) 406-411

27. COMPASS Collaboration (C. Adolph (Erlangen - Nuremberg U.) et al.), The spin structure function g1p of the proton and a test of the Bjorken sum rule, Phys.Lett. B753 (2016) 18-28

28. COMPASS Collaboration (C. Adolph (Erlangen - Nuremberg U.) et al.), Observation of a New Narrow Axial-Vector Meson a1(1420), Phys.Rev.Lett. 115 (2015) no.8, 082001

29. COMPASS Collaboration (C. Adolph (Erlangen - Nuremberg U.) et al.), Measurement of radiative widths of a2(1320) and $\pi_2(1670)$, Eur.Phys.J. A50 (2014) 79

30. COMPASS Collaboration (C. Adolph (Erlangen - Nuremberg U.) et al.), A high-statistics measurement of transverse spin effects in dihadron production from muon–proton semi-inclusive deep-inelastic scattering, Phys.Lett. B736 (2014) 124-131

31. COMPASS Collaboration (C. Adolph (Erlangen - Nuremberg U.) et al.), Measurement of azimuthal hadron asymmetries in semi-inclusive deep inelastic scattering off unpolarised nucleons, Nucl.Phys. B886 (2014) 1046-1077

32. COMPASS Collaboration (C Adolph (Erlangen - Nuremberg U.) et al.), Transverse target spin asymmetries in exclusive ρ^0 muoproduction, Phys.Lett. B731 (2014) 19-26

33. COMPASS Collaboration (M. Pešek et al.), COMPASS polarized target for Drell-Yan, PoS PSTP2013 (2013) 009